UNIVERSITY OF CAPE TOWN

MASTER'S DISSERTATION

In-Silico Design and Verification of an Extracorporeal Normothermic Cardiac Perfusion System for use during Heart Transplantation Procedures

Author:
Ronald VAN DEN BERG
(VBRRON002)

Supervisor:
Prof. Sudesh SIVARASU *Co-Supervisor:*
Dr. Jithan Jacob KOSHY

A dissertation submitted in fulfilment of the requirements for the degree of Master of Biomedical Engineering

in the

DIVISION OF BIOMEDICAL ENGINEERING

DEPARTMENT OF HUMAN ANATOMY

January 31, 2025

Declaration of Authorship

I, Ronald VAN DEN BERG (VBRRON002), declare that this thesis titled, "*In-Silico* Design and Verification of an Extracorporeal Normothermic Cardiac Perfusion System for use during Heart Transplantation Procedures" and the work presented in it are my own. I confirm that:

- By submitting this project electronically, I declare that the entirety of the work contained therein is my own, original work, that I am the sole author thereof (save to the extent explicitly otherwise stated)
- Where I have consulted the published work of others, this is always clearly attributed.
- Where I have quoted from the work of others, the source is always given. With the exception of such quotations, this thesis is entirely my own work.
- I have acknowledged all main sources of help.
- Where the thesis is based on work done by myself jointly with others, I have made clear exactly what was done by others and what I have contributed myself.
- The reproduction and publication thereof by The University of Cape Town will not infringe any third party rights and that I have not previously in its entirety or in part submitted it for obtaining any qualification.

Signed: Signed by candidate

Date: **28/05/25**

UNIVERSITY OF CAPE TOWN

Abstract

Faculty of Health Sciences
Department of Human Anatomy

MSc. Biomedical Engineering

In-Silico Design and Verification of an Extracorporeal Normothermic Cardiac Perfusion System for use during Heart Transplantation Procedures

by Ronald VAN DEN BERG (VBRRON002)

Heart transplantation relies on effective donor organ preservation to ensure successful graft viability. Since the first human heart transplant in 1967 by Christiaan Barnard, organ preservation techniques have evolved from static cold storage with cardioplegic arrest to continuous blood perfusion, which enhances metabolic support and extends viable ischemic time. This study explores the development of a system for continuous myocardial perfusion to improve donor heart preservation during transplantation.

Using *in-silico* modelling and simulation, the study defines functional requirements for a proof-of-concept system capable of achieving physiologically relevant pressure and flow waveforms necessary for sustained coronary perfusion. A cardiovascular hemodynamic simulation environment was established by adapting lumped parameter models and integrating computed tomography angiograms, facilitating both *in-silico* and coupled *in-vitro* validation analyses. This enabled the development of a bench testing model that replicated physiologically relevant coronary perfusion dynamics. The bench testing model provided critical insights for refining *in-silico* simulations and optimising design parameters for improved myocardial perfusion.

Validation was performed through vessel-specific flow rate comparisons with computational fluid dynamics simulations. Experimental results identified a time delay in relation to the identified set of functional and control parameters when achieving target physiological pressures, informing future system optimisation. Further findings allowed for the identification of relative flow proportion exiting through the *Left Circumflex* and *Right Major Coronary* arteries and was shown to behave as a second order time derivative with respect to the inflow waveform applied to a fabricated flow phantom during testing. Similarly, the proportion of flow exiting through the *Left Anterior Descending* and *Ramus Intermedius* arteries exhibited first order time derivative behaviour in relation to the inflow signal.

The resultant outcomes of testing and analysis allowed for the tuning of an embedded pump control system yielding the optimised parameter control values for proportional, integral and derivative gain of 147.74, 2.57 and -4974.96 respectively.

The findings of this study establish a framework for the development of an automated continuous myocardial perfusion system, contributing to enhanced donor heart preservation strategies for clinical transplantation. ...

Acknowledgements

The following are acknowledged for their valuable contributions in the form of consultation and guidance within aspects of work covered within this study:

Associate Professor Malebogo Ngoepe - Application and use of Computational Fluid Dynamics.

Associate Professor Wei Hua Ho - Fabrication and validation methods of rigid body flow phantoms.

Michael Brown - Control system theory and electronic integration.

Dr. Struan Hume - Computational Fluid Dynamic Mesh and Model setup.

Beaurich Groenewald - Perfusion specific clinical guidance and loaning of materials.

Table of Abbreviations

ACS - Acute Coronary Syndrome
ADP - Aortic Diastolic Pressure
AF - Atrial Fibrillation
ASD - Atrial Septal Defect
AV - Atrioventricular
AVR - Aortic Valve Replacement
BP - Blood Pressure
CABG - Coronary Artery Bypass Grafting
CAD - Coronary Artery Disease
Cath - Catheterization
CFD - Computational Fluid Dynamics
CHD - Computational Haemodynamic
CHF - Congestive Heart Failure
CI - Cardiac Index
CO - Cardiac Output
CPB - Cardiopulmonary Bypass
CTA - Computed Tomography Angiography
DBD - Donation after Brain Death
DCD - Donation after Circulatory Death
DVT - Deep Vein Thrombosis
ECG/EKG - Electrocardiogram
ECMO - Extracorporeal Membrane Oxygenation
EF - Ejection Fraction
FAS - Fractional Area Shortening
HOCM - Hypertrophic Obstructive Cardiomyopathy
HR - Heart Rate **HTN** - Hypertension
IABP - Intra-Aortic Balloon Pump
IVC - Inferior Vena Cava
IVS - Interventricular Septum
LA - Left Atrium
LAD - Left Anterior Descending
LCX - Left Circumflex
LPM - Lumped Parameter Model
LVSW - Left Ventricular Stroke Work
LVAD - Left Ventricular Assist Device
LVEDP - Left Ventricular End-Diastolic Pressure
MAP - Mean Arterial Pressure
MI - Myocardial Infarction
MRI - Magnetic Resonance Imaging
MVO2 - Myocardial Oxygen Consumption
MVR - Mitral Valve Replacement
PDA - Posterior Descending Artery
PCI - Percutaneous Coronary Intervention
PE - Pulmonary Embolism
PID - Proportional Integral Derivative
PPM - Predictive Pump Model
PVR - Pulmonary Vascular Resistance
RA - Right Atrium
RCA - Right Coronary Artery
RMS - Root Mean Squarex
RSVP - Right Systolic Ventricular Pressure
RV - Right Ventricle
SCD - Sudden Cardiac Death
SV - Stroke Volume
SVR - Systemic Vascular Resistance
SVC - Superior Vena Cava
TAVR - Transcatheter Aortic Valve Replacement
TEE - Transesophageal Echocardiogram
TTE - Transthoracic Echocardiogram
TVR - Tricuspid Valve Replacement
VAD - Ventricular Assist Device
VF - Ventricular Fibrillation
VSD - Ventricular Septal Defect
VT - Ventricular Tachycardia

List of Figures

List of Tables

Contents

Chapter 1

Introduction

1.1 History

The first human heart transplant was performed by Christiaan Barnard and his team in 1967 (Barnard, 1969). The procedure utilized a cardioplegic solution to induce donor heart arrest, allowing for organ explantation and subsequent transfer in a hypothermic state to reduce metabolic demand. While operative techniques have remained fundamentally similar since then, most recent advancements have focused on organ preservation and transfer, primarily involving donors who have succumbed to brain death (Firestone, 1991).

Current developments in cardiac transplantation have explored donor heart transfer while maintaining continuous blood perfusion to the major coronary arteries. However, the organ still requires cardioplegic arrest to facilitate explantation (Rega et al., 2024). Advances in myocardial protection techniques have demonstrated the benefits of blood cardioplegia as a method for oxygen and metabolite delivery, helping to reduce metabolic demand (White et al., 2015). Nevertheless, this approach has not been universally accepted as a definitive solution for myocardial protection during organ transfer due to total ischemic time constraints and the resulting accumulation of lymphatic fluid, which increases the risk of myocardial oedema (Cobert, West, and Jessen, 2008).

1.2 Prevalence

More than **5000** cardiac transplants occur each year around the world, although it is estimated that up to **50,000** people are candidates for transplantation (Strüber et al., 2009). The population of people who died from CVD's in **2019** was estimated to be approximately **USD 17.9 Million** according to a *WHO* published report in **June 2021**. The market for transplant specific treatment has been benchmarked at approximately **USD 11.62 Billion** in **2023** and is estimated to grow from **USD 12.84 Billion** in **2024** to **USD 27.22 Billion** by **2032** (SkyQuest, 2024).

1.3 Transplantation Protocol

Chronic VAD therapy has become the clinical standard and serves to prolong a patients life during the time in which they await transplantation. Early decision to use VAD treatment has been shown to result in **> 75%** one year survival rate (Strüber et al., 2009). This is however by no means a long-term solution. The reality for many patients diagnosed with end-stage cardiovascular diseases or complications is the requirement for transplant.

1.3.1 Cardiectomy

Once a donor heart has been inspected and approved for transplantation, the cardiectomy procedure may commence following the standard protocol for heart transplantation (Firestone, 1991). The process begins with the ligation of the superior vena cava (SVC), followed by an incision in the inferior vena cava (IVC) to exsanguinate the patient. The left heart is then vented through an incision in either the left atrial appendage or a pulmonary vein. Next, the aorta is cross-clamped, and the heart is flushed with a cold preservation solution to maintain its viability. Once adequately prepared, the heart is explanted and placed in a sterile bag filled with a preservation solution. To ensure optimal preservation during transport, two additional sterile bags are applied, and the heart is then placed in an ice-filled cooler for delivery to the transplant recipient.

1.3.2 Cardiopulmonary Bypass

The human heart among other roles, functions as the centrepiece to the human cardio-circulatory system in two main ways. The first is to receive deoxygenated blood from the peripheral venous circulatory system and circulate it to the pulmonary system through proper ventricular contraction and ejection. The second is to receive returning

oxygenated blood from the pulmonary system and re-circulate this blood via peripheral arterial networks to the remainder of the body (Ramanathan and Skinner, 2005).

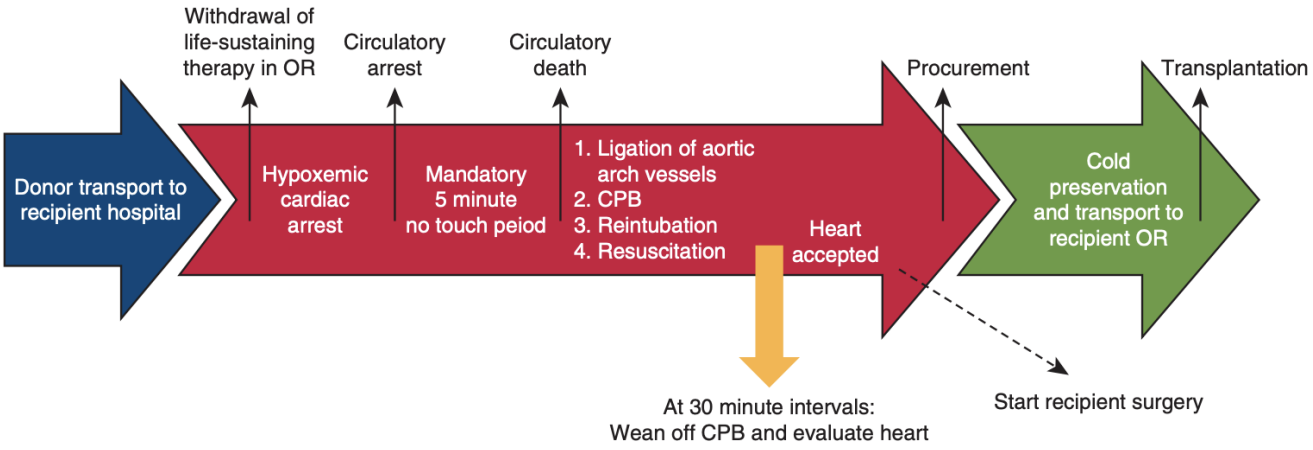

FIGURE 1.1: Utility of CPB in Cardiac Allograft Transplantation (Smith et al., 2022)

A surgical cardiopulmonary bypass (CPB) procedure, also known as Heart-Lung machine support, is a technique used during specific surgeries to temporarily take over the functions of the heart and lungs. Patients receiving a donor heart during transplant undergo bypass from the time the native heart is explanted until the new donor heart is implanted, reactivated and native cardiocirculatory function has resumed (Firestone, 1991).

The procedure involves several key steps to ensure a controlled and stable surgical environment. First, the patient is administered general anesthesia to induce unconsciousness and ensure a pain-free operation. Once anesthetized, cannulation is performed by inserting small tubes called cannulas into the blood vessels to redirect blood flow. Two main types of cannulas are used: arterial cannulas, which divert blood away from the heart, and venous cannulas, which return oxygenated blood to the body. These cannulas are then connected to the heart-lung machine, a device consisting of a pump and an oxygenator. The pump assumes the function of the heart by circulating blood throughout the body, while the oxygenator removes carbon dioxide and adds oxygen, effectively replacing the function of the lungs.

With the heart-lung machine in place, bypass is initiated by gradually diverting blood flow away from the heart and lungs. To protect the heart during the procedure, the surgeon may administer a cardioplegic solution to temporarily halt its activity. Once the heart is stopped and blood circulation is maintained by the machine, the surgeon proceeds with the necessary cardiac intervention, such as coronary artery bypass grafting, valve repair or replacement, or other corrective procedures. Throughout the operation, the patient's vital signs—including blood pressure, oxygen levels, and temperature—are continuously monitored to ensure stability.

After the surgical intervention is complete, the process of weaning off bypass begins. The surgeon gradually restores blood flow to the heart and lungs, allowing the heart to resume its normal function. As the heart regains activity, the heart-lung machine is progressively disconnected. Finally, the cannulas are removed, and the blood vessels are sutured. The surgical incisions are then closed, and the patient is transferred to the intensive care unit (ICU) or a post-operative recovery area for further monitoring and stabilization. The current standard of care for allograft management from the time of donor explantation to recipient implantation remains to be the method of **static-cold storage**. Measures are taken in order to achieve diastolic arrest creating a reduction of metabolic demand and minimising the impact of ischemic damage during relocation (Hess, Ziegler, and Kaczorowski, 2022). The heart is typically arrested *in-situ* through the use of a cardioplegic solution and then placed within an ice bath at a storage temperature of approximately 4°C. This procedure results in the organ becoming susceptible to damage on a cellular level especially during prolonged cold ischemic periods of greater than approximately five hours. Prolonged ischemic arrest has been shown to be positively correlated with an increase in the probability of primary graft failure (White et al., 2015).

1.3.3 Implantation Procedure

Transplantation as a surgical procedure consists of two distinctive methodologies (Wicomb, 1983):

1. **Orthotopic:** This procedure consists of excision of the recipient's heart and implantation of a donor heart in the same position with functional anastomosis of all major connecting vessels.

2. **Heterotopic:** This denotes the surgical procedure of implanting the donor heart without excision of the recipient heart. The donor heart thus functions to supplement ventricular stroke work of the recipient heart.

1.4 Shortcomings of Conventional Transplant Protocol

Upon the resumption of ATP synthesis, observations of sarcoplasmic reticulum Ca^{2+} cycling leading to cytosolic oscillations of Ca^{2+} have been made (Ruiz-Meana et al., 2009). Overloading of Ca^{2+} due to these oscillations, has been associated with the activation of degradative enzymes thought to potentially cause irreversible tissue injury (Suleiman, Halestrap, and Griffiths, 2001). When the myocardium is cooled without the administration of a cardioplegic arrest, a phenomenon known as rapid cooling contracture occurs, leading to myocardial damage in response to the loading of calcium that would otherwise be mitigated by the onset of a cardioplegic arrest (Rebeyka et al., 1990). The disadvantages of a cardioplegic heart include decreased cellular activity in relation to the shutting down of enzymatic pathways at lower temperatures, cellular swelling as well as decreased activity of the ATP-dependent cell membrane channels.

In addition, damage associated with hypothermia has shown deleterious effects on myocardial preservation such as the dysregulation of cell membrane function and transmembrane channels, mitochondrial damage and reperfusion injury incurred during reactivation.

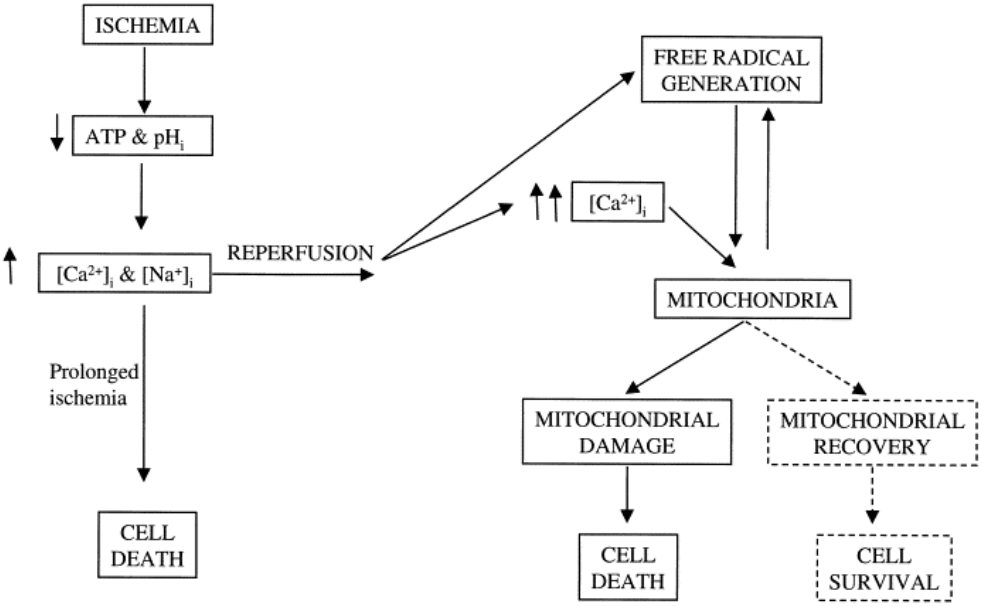

FIGURE 1.2: Mechanisms of Reperfusion Injury and Ischemia (Suleiman, Halestrap, and Griffiths, 2001)

1.5 Innovation and Advancement of Myocardial Preservation

The maintenance of *in-vivo* physiological function of the donor organ throughout explantation, transportation and implantation could be considered the gold standard for preservation. The utilisation of mechanical cardiocirculatory support devices have allowed for continuous left ventricular support and the maintenance of controlled flow and pressure of thermally regulated blood while sustaining pharmacologically induced bradycardia. Left ventricle support has however not been documented to address the problem of vertical heart displacement required for multivessel off-pump coronary artery bypass grafting (Porat et al., 2000).

1.5.1 Extracorporeal Normothermic Perfusion

Extracorporeal perfusion refers to the circulation of blood outside the body. Innovations in hypothermic perfusion systems for donor heart preservation have increased the maximum allowable transfer time, making geographically distant procurement a viable strategy for expanding the donor pool (Brink and Cooper, 2005).

Organ preservation using normothermic *(warm)* maintenance, achieved through the control of physiological flow and pressure parameters, has enabled prolonged preservation and successful transplantation of both healthy hearts and those that have sustained significant ischemic damage (Brink and Cooper, 2005). This technique presents a potential solution to the shortage of available donor organs for transplantation.

Normothermic perfusion has also allowed hearts that have undergone circulatory death to remain viable for transplantation. These hearts are classified as *Donation after Circulatory Death* **(DCD)** hearts. In contrast, hearts from patients who have suffered a fatal brain injury are referred to as *Donation after Brain Death* **(DBD)** hearts.

Langendorff Model for Coronary Perfusion

The use of the Langendorff model for perfusion of the *ex-vivo* heart and the study of its physiology have been the corner-stone for most experimental work in this field (White et al., 2013).

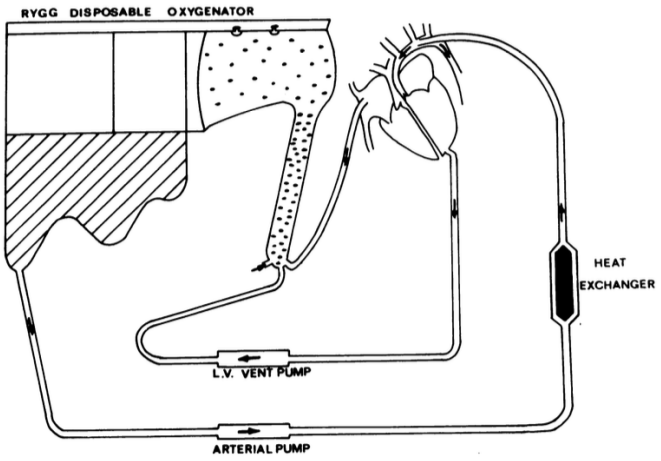

FIGURE 1.3: Langendorff model for Coronary Perfusion

The original description of the *Langendorff Perfusion Model*, as shown in *Figure 1.3*, has remained largely unchanged to this day. In this model, the aorta is cannulated, and the heart is perfused with a buffer solution via the retrograde flow of blood (Bell, Mocanu, and Yellon, 2011). The accumulation of pressure in the aortic root forces the aortic valve to close, directing the buffer through the coronary vasculature. After traversing the vascular bed, the buffer drains into the coronary veins, then into the coronary sinus, and finally fills the right atrium. During perfusion, the left ventricle remains empty. An ideal form of myocardial protection could be achieved through the maintenance of continuous coronary blood flow to the myocardium thus maintaining the constant oxygen supply required for ongoing cellular respiration in addition to preserving mechanisms for excretion and most importantly the limitation of myocardial stresses. In the past decade, machine perfusion has presented itself as a viable alternative to the use of static cold-storage affecting of donor hearts thus improving the short term results of cardiac transplantations (Cobert, West, and Jessen, 2008).

Vertical displacement has also been seen shown to cause haemodynamic instability predominantly as a result of right heart dysfunction (Porat et al., 2000). In a study conducted by (Cobert et al., 2010), the role of machine perfusion in the prolonging of donor heart preservation was evaluated. Additionally, the importance of oncotically active agents in the prevention of myocardial cell swelling was also explicated. The *UWMP* solution resulted in reduce oedema formation during storage within an *ex-vivo* environment.

A donor brain death causes the release and activation of products that pose deleterious effects on myocardial function. In a study conducted by (White et al., 2015), the use of whole blood perfusate was suggested due to an observed antioxidant capacity that may be protective to the *ex-vivo* heart. A further conclusion recommended the use of banked plasma combined with washed red blood cells as a clinical perfusate option.

The functional alterations occurring in whole blood when kept in the extracorporeal system threaten the efficacy of continual perfusion. Additionally, the use of donor blood thus poses a number of additional challenges, including the logistics of salvaging the required volume of donor blood to prime the extracorporeal circuit, the accumulation of toxins within the donor blood prior to harvesting due to the donor's status, the activation of the coagulation cascade, leucocyte activation, the accumulation of potassium due to red cell lysis, and the buildup of cellular debris from cell lysis. Ending lactate has thus been determined to be the best predictor of post-transplant graft failure (Alomari et al., 2022).

Advantages of prolonged preservation periods allow for distant organ procurement, improved organ allocation and the subsequent increase in accuracy and efficiency of donor-recipient matching (Ardehali et al., 2015).

1.6 Existing/Emerging Solutions

The existing solutions for donor heart preservation play a crucial role in improving organ preservation, transplant outcomes, and overall success rates in cardiac transplantation. In 2014, an evaluation of the use of the *Transmedic Organ Care System* by (Sáez et al., 2014) using an adverse donor profile concluded that the system has become the standard of practice within their institution due it's utility of increasing the eligible donor pool and reducing the probability and risk of primary graft failure.

TABLE 1.1: Comparison of Cardiovascular Perfusion Solutions

Solution	Mean Sum of Costs per Procedure	Advantages	Disadvantages
Static Cold Storage with Cardioplegic Arrest **(Best Practice)**	In 2011 Approx. $782,400 (Evans, 2013)	• Widely available globally. • Relatively simple execution. • Requires limited pre-planning.	• Limited to 5-hour cross-clamp time. • Reperfusion injury likely.
Hypothermic Perfusion with Cardioplegic Arrest **(XVIVO - HOPE)**	Not yet commercially available	• Lower cost than OCS. • Dependent on correct application and concentrations.	• Does not negate cardioplegic arrest. • May cause cytosolic calcium loading, myocardial edema, and acidosis.
Controlled Warm Perfusion in absence of Arrest **(Transmedic Inc.)**	In 2021 Approx. $1,032,212 (Urban et al., 2024) per case	• High fidelity, effective in DCD allografts. • Functional advantages of using donor blood.	• Requires manual control. • Requires specialized training. • Not globally available.

A further experiment conducted by (Sáez et al., 2015) using the *Organ Care System* aimed at studying the effect of extracorporeal coronary perfusion in the resuscitation of porcine hearts. Graft salvage remained possible with arrest times as long as twenty minutes.

Studies recruiting the extracorporeal *Organ Care System* have shown prolonged preservation times in comparison with cold storage before implantation (Kothari, 2023). Cold-ischemic time is reduced using this system because it is restricted to the process of allograft retrieval to initiation of perfusion and the final period of implantation into the recipient (Ardehali et al., 2015).

Cold ischemic time can thus be considered the most important factor that is diminished by the *Organ Care System* due to it's profound impact subsequent myocardial function. Logistics concerned with the preparation and transportation of donor hearts are also simplified by a reduction of factors otherwise involved when exclusively using the method of static cold storage (Sáez et al., 2014). Studies conducted on rat models have shown that cardioplegic arrest at normothermia may provide better protection than at hypothermia (Ji and Ündar, 2006).

Implementation of the *Organ Care System* for the purpose of donor heart procurement and transportation in a single-institutional setting was however, not associated with significant differences in the intermediate outcomes of cardiac transplantation recipients two years post-op. Reviews of the *Organ Care System* thus propose it as a valid adjunct in the preservation of an allograft in the context of transplantation (Ardehali et al., 2015). This encourages a need for further research and innovation of this technology as a potential vehicle for the advancement of future transplantation protocols.

1.7 Identified Limitations

In addition to the fact that the current protocol for transplant limits the distance with which a donor heart can be transported due to the maximal allowable aortic cross clamp time - the gold standard for continuous perfusion in South Africa does not leverage any existing potential solution concepts for improved graft success i.e continuous normothermic perfusion *in-transit*.

The method in which continuous warm perfusion is applied hinges on the maintenance of adequate pressure and flow delivery to respective vessels during the logistical period of the procedure. Attention and maintenance of

transplant teams to the organ's instantaneous state of preservation would be constantly required. Failure of these teams to respond to changes in the organ's stability via manual intervention introduces the propensity for risk of human error.

1.8 Research Gap

The development of a normothermic perfusion system for preservation of donor hearts would result in an increase in the total allowable organ transfer time, while minimising subsequent myocardial damage associated with extended periods of hypothermic ischemia. This allows for donor organ procurement to become viable over greater proximities in relation to the site of implantation. Considering the greater potential geographic distances South African transplant teams may then become able to reach and traverse, there exists a great advantage in the use of a continuous myocardial perfusion system.

The development of a technique for continuous myocardial perfusion enables the ischemic time factor between explantation and implantation to be negated. By effectively maintaining a closed loop extracorporeal circuit throughout a transplantation procedure supplemented by dynamic feedback control over parameters governing efficient perfusion, the allograft can hypothetically remain in an *in-situ* state thus achieving the gold standard of myocardial preservation.

A potential solution system approach would ideally aim to provide continuous coronary perfusion using oxygenated blood during the explantation, transfer, and implantation of the donor heart. This approach ensures the maintenance of several key factors including a constant supply of oxygen, a steady provision of essential metabolites, normothermia, lymphatic drainage, conventional physiological haemodynamics and a reduction in required left ventricular stroke work (Brink and Cooper, 2005).

At present in the South African Healthcare Industry, there is no such system or device present in use having achieved FDA approval, and able to achieve the aforementioned characteristics. In conjunction with the need for allograft procurement and efficient donor matching, there exists a pertinent field for research, design and subsequent development of a device able to provide extracorporeal normothermic perfusion using locally attainable and sourceable machine components.

To date there exists an absence of computational tools developed that allow for the simulation and analysis of coronary perfusion with respect to the cross-clamped cannulated aortic root, such as the case during the perfusion of the transplanted heart. This gap in model development extends across both an *in-silico* and *in-vitro* simulation landscape. A novel precedent would be set through the combined *in-silico* and *in-vitro* approach to transplant specific perfusion simulation conducted in parallel with a developed perfusion bench testing apparatus that is designed specifically to target cannulated cross-clamped aortic root geometries. Using this foundation for transplant specific perfusion modelling and analysis, the necessary functional design considerations for the development of an extracorporeal perfusion system can be investigated.

The incorporation of automated flow control within a machine model functionality reduces the requirement for manual intervention of transplant teams toward the maintenance of *in-transit* organ stability. The self-stabilising utility of automated flow control lends a potential advantage by simplifying the organ transport process in the face of already present logistical obstacles. This reduces the degree to which the impact of human error during the logistical period may compromise organ preservation and primary graft outcomes.

1.9 Study Objective Feasibility Analysis

Code	Possible Objective	Verification	Validation	Feasibility
1	Fully Functional Perfusion Solution System	Full circuit assembly and *In-Vitro* functional testing	Efficiency of Myocardial Preservation	Concept is already valid and would require large animal testing and subsequent ethics approval to validate a protype's operational efficacy.

Code	Possible Objective	Verification	Validation	Feasibility
2	System Circuit Design including Feedback	*In-Silico* Multi-parameter Coupled Model Simulation	Fully assembled and tested feedback system	Monetary and time limitations associated with the implementation of system feedback and accurate testing in both a physical and *In-Silico* landscape.
3	Simulated Perfusion Control System Model + Non-Coupled CFD Mesh Model	Validation of Individual Model Aspects	Scenario Specific Simulation Testing	Feasible
3A	Perfusion Model	Variation of systemic parameters *(Initial Pressure Drop, Coronary Impedance, HR Phase Offsetting)* and comparison against clinically expected values	Bench test flow trial for measurement comparison and resultant model correction.	Feasible
3B	CHD Model	Verification of setup and configuration using mesh independence study	Simulation data compared with physical flow data measured through resin printed phantom	Feasible

TABLE 1.2: Study Objective Feasibility Logic

1.10 Aim

The aim of the study is to model the design and operation of an extracorporeal perfusion device intended to eliminate cold ischemic time during cardiac transplantation.

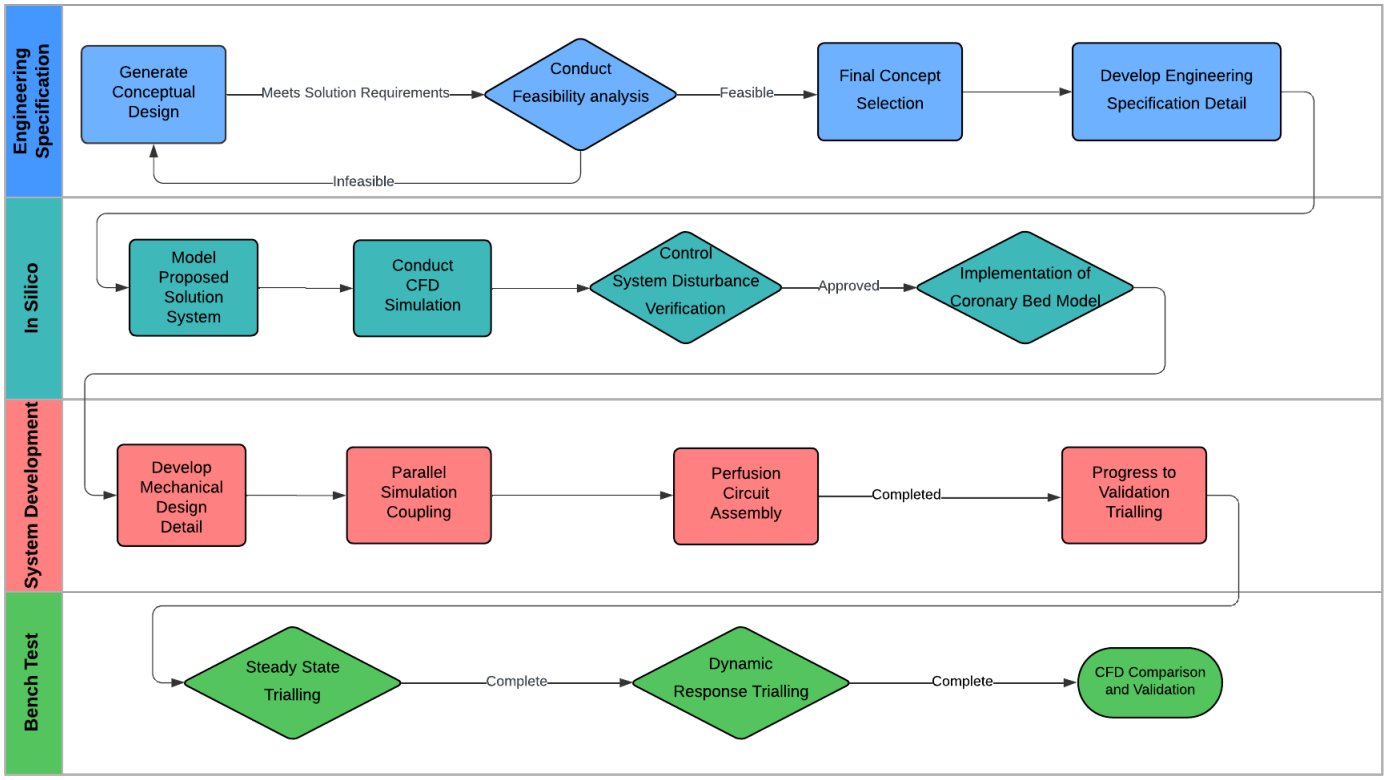

FIGURE 1.4: Project Flow Methodology

1.11 Objectives

1. Development of an *In-Silico* perfusion simulation landscape, by achieving the following.
    - Creation of an antegrafe perfusion heart model by adapting existing modelling principles and techniques present in literature.
    - Incorporation of a pump system exhibiting dynamic feedback control through the implementation of a PID control loop capable of exhibiting both continuous and pulsatile flow modalities.
    - Verification of control implementation through analysis of control response to applied variable disturbances.
    - Adaptation to a transplant specific perfusion model based on the antegrade perfusion model with the addition of a coronary vascular bed system element.
2. Development of an anatomically accurate mesh model for the application of Computational Fluid Dynamic calculations from the perspective of perfusion through aortic root cannulation, by achieving the following:
    - Segmentation of an Aortic Root using anonymous patient CT-imaging data.
    - Creation of a finite element perfusion model through the meshing of aortic root geometry augmented with cannula geometry.
    - Confirmation of mesh independence through verification of a mesh independence study.
    - Perfusion specific flow calculation and analysis using polyhedric adaptation of verified model mesh.
    - Adaptation of root model into a mechanical part file for use in physical flow testing and mesh flow data verification.
    - Creation of physical root model that can be used for flow testing.
3. Physical flow circuit bench test design, assembly and testing.
    - Incorporation of a parallel hydraulic system aspect to *In-Silico* model to account for blood specific fluid behaviour and physical circuit components within simulation.
    - Physical test rig design and perfusion circuit assembly based on hydraulic model configuration.
    - Bench testing using physical Aortic Root model for the purpose of flow data collection.
    - Hydraulic model correction using comparison of simulated and actual flow measurement data.
    - Validation of corrected model simulation using captured physical flow data.
    - PID control system tuning based on validated model and observations from bench testing.

1.12 Expected Outcomes

The following research outcomes are expected from this study:

1. A *Simscape* simulation model that can be used to analyse the pressure control responses of a dynamic feedback control pump system used to perfuse a heart theoretically being transplanted. The model accounts for physical losses present within an extracorporeal perfusion circuit of know specifications. System state parameters can be varied to analyse the system perfusion operation with respect to different hypothetical scenarios e.x Differing Heart Rate, Fluid Properties etc.
2. An Aortic Root mesh model representative of aortic root cannulation and perfusion that can be used to calculate accurate Flow and Velocity measurements that have been verified at chosen boundary conditions of the Right Major, Left Major, Left Anterior Descending and Left Anterior Circumflex Coronary Arteries.
3. A test rig allowing for the physical data analysis of differing perfusion use-cases and the framework with which to begin to consider necessary design aspects for the fabrication of a fully functional prototype.

1.13 Chapter Overview

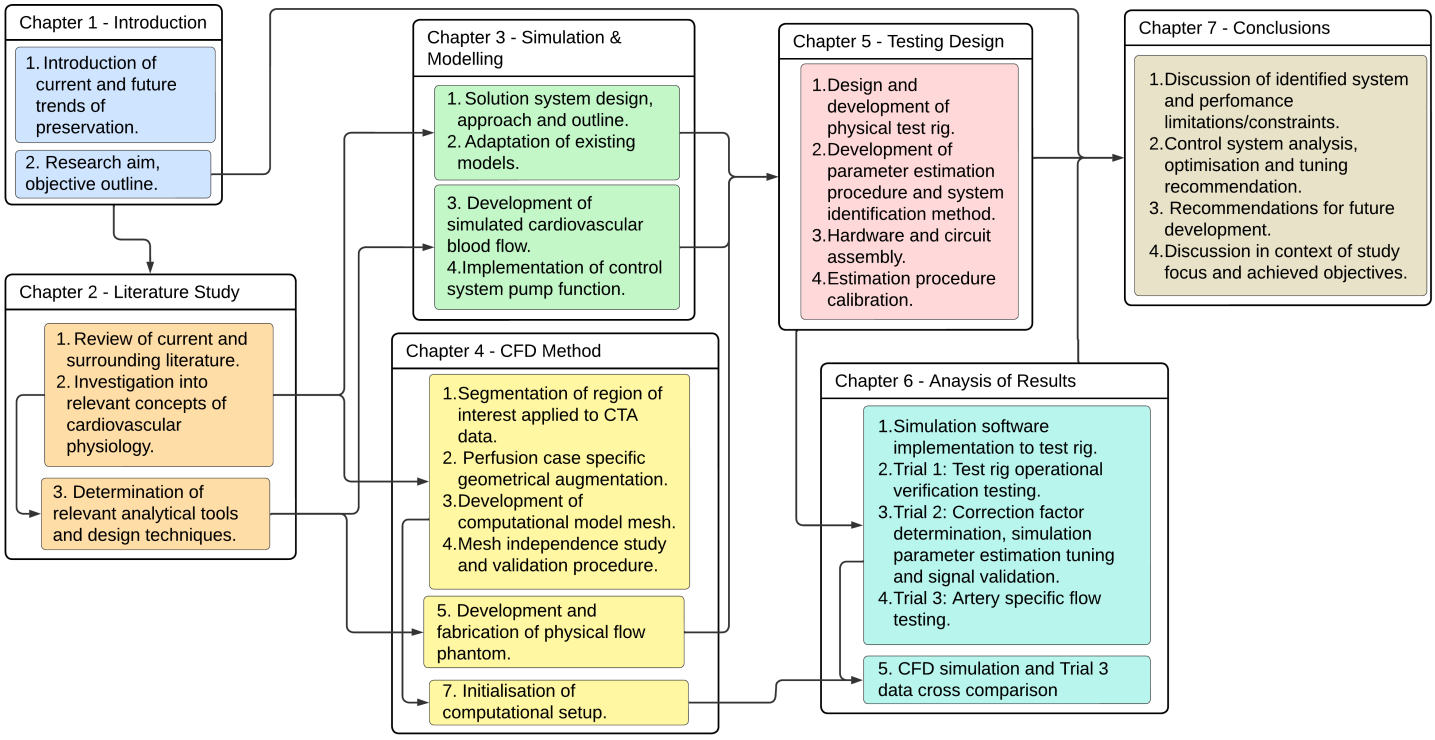

FIGURE 1.5: Chapter Breakdown and Information Process Flow

Chapter 2

Review of Literature

2.1 Cardiovascular Anatomy and Function

The major vessel connecting the left ventricle to the systemic circulation is called the Aorta and branching off of it are two arteries that function to deliver oxygenated blood to the cardiac muscle tissue known as the myocardium. The myocardium allows for ejection of blood from each chamber through muscular contraction and thus relies on oxygen supply through the blood for cellular metabolism. These branches are the left and right coronary arteries. The two coronary ostia arise from the sinuses of Valsalva proximal to the base of the Aortic Root.

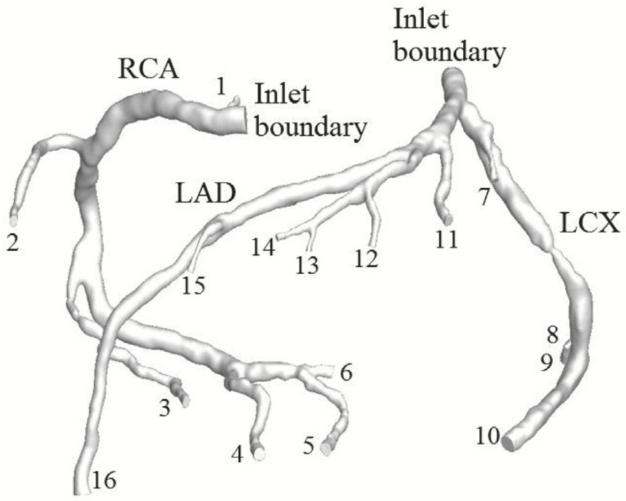

FIGURE 2.1: Patient Specific Coronary Artery Geometry

The Left Coronary Artery **(LCA)**, divides into the left and anterior descending artery and circumflex artery. The LCA serves to supply the lateral and anterior walls of the left ventricle as well as the anterior two thirds of the interventricular septum. The Right Coronary Artery **(RCA)**, supplies the walls of the right ventricle as well as the posterior wall of the left ventricle and posterior third of the septum.

The major coronary arteries divide into epicardial arteries and intramuscular arteries that penetrate the myocardium perpendicularly. The majority of blood from the myocardium of the left ventricle drains into the coronary sinus, while blood from the right ventricle drains into the anterior cardiac vein (Ramanathan and Skinner, 2005).

2.1.1 Cardiocirculatory Physiology

The heart functions tow circulate blood throughout the body by means of two muscular contractile chambers known as the left and right ventricles. The left and right ventricles function to circulate oxygenated and de-oxygenated blood to the systemic and pulmonary circuits respectively. Blood is then either oxygenated in the case of the pulmonary circuit and de-oxygenated in the case of the systemic circuit and returned back to the heart. Returning blood collects in the left and right atrial chambers from which it is then pumped into the ventricles.

2.1.2 Cardiac Pressure Changes and Signalling

Ventricular filling and contraction can be better understood through the visualisation of the resulting pressure-volume curve measured during cardiac function. Ventricular function can be divided into four distinct phases as follows: **Isovolumic Relaxation, Ventricular Filling, Isovolumic Contraction and Ventricular Ejection**.

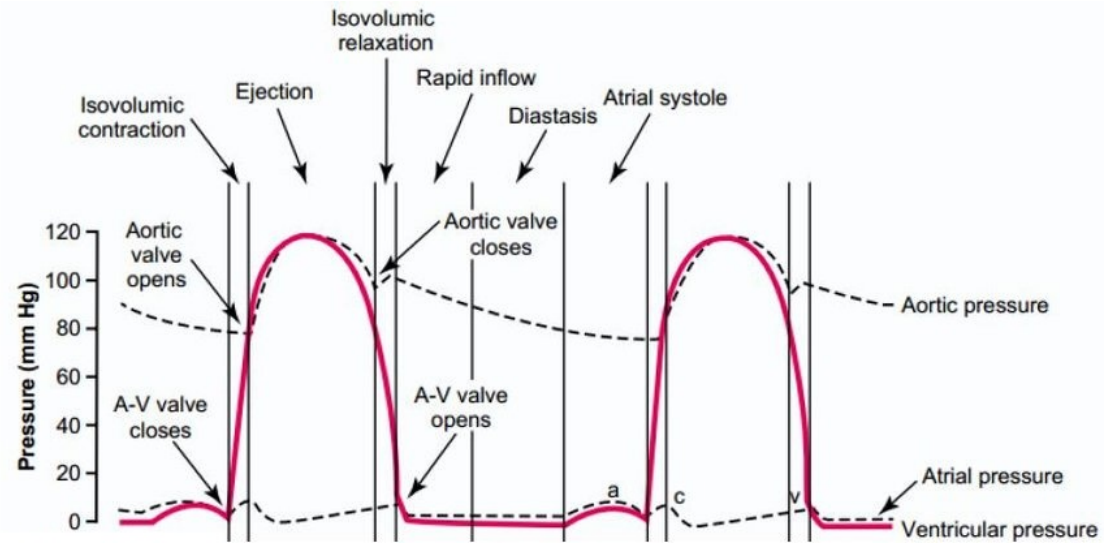

FIGURE 2.2: Pressure Changes during the Cardiac Cycle (Mansouri, 2016)

Isovolumic relaxation occurs immediately after ventricular contraction where in the aortic valve closes while the mitral valve remains shut, resulting in a reduced ventricular pressure. This low pressure creates a gradient that forcing the opening of the mitral valve. Ventricular filling begins when the mitral valve opens allowing blood to flow from vessels into the expanding ventricle. This ventricular filling phase continues until ventricular pressure exceeds atrial pressure causing the mitral valve to shut. Isovolumic Contraction denotes the period between the closure of the mitral valve and the opening of the aortic valve. During this phase pressure builds within the ventricle without blood ejection, leading to the first heart sound **(S1)**. Ventricular ejection begins when the aortic valve opens, allowing blood to be ejected from the ventricle. A healthy ventricle typically ejects approximately $\geq$ **60%** of its volume. The aortic valve closure marks the end of this phase, resulting in the second heart sound **(S2)** (Pollock and Makaryus, 2017).

From the time that the atrioventricular valve between the ventricles and connecting major vessel is open, to the time that the valve shuts is known as the Diastolic Phase of the cardiac cycle. During this time, the atria are concurrently increasing in volume from returning blood. Similarly, during the time from when the atrioventricular valve shuts and is once again opened, there is blood filling each of the respective ventricles. This portion of the cardiac cycle is known as the Systolic Phase (Sevre, 2006).

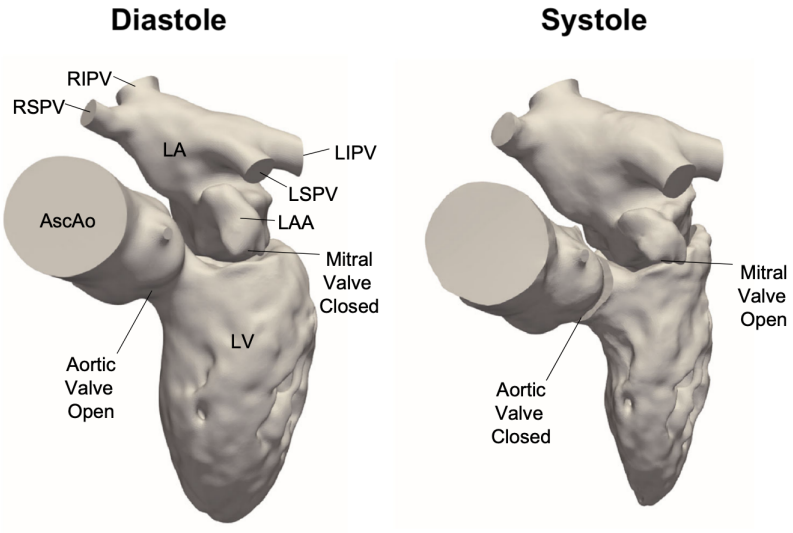

FIGURE 2.3: Anatomical Rendering of Volume Variations during Cardiac Cycle

Diastole : Blood is propelled into the ventricle due to potential energy stored in the elastic walls of neighbouring blood vessels.

Systole : Ventricles force blood into the systemic/pulmonary circulation causing distension of connecting blood vessels.

2.2 Methods and Procedures for Cardiocirculatory Support

2.2.1 Left Ventricular Unloading

In a study by (Kapur et al., 2015) the use of two different methods of pump circulation modalities have been used as a means to investigate the central hypothesis that Left Atrial Inflow Cannulation provides a greater reduction in *LVSW* compared with Trans-Aortic Left Ventricle cannulation with respect to acute left heart injury. Results suggest that at matched flow rates the magnitude of *LVSW* reduction is similar, but generate distinct profiles of *LV* unloading. Additionally, the use of mechanical circulatory support devices has been shown to increase organ perfusion through the augmentation of coronary flow, the reduction of ventricular volume and filling pressures as well as an overall reduction in wall shear stresses, ventricular stroke work and thus subsequent myocardial oxygen demand .

Left-atrial outflow cannulation has also shown benefits to surgical procedure by maintaining perfusion through the reduction of haemodynamic turbulence when returning physiological blood flow back from conventional retrograde perfusion. This presents a potentially viable procedure solution for allograft implantation without cessation of perfusion (Kapur et al., 2015).

2.2.2 Extracorporeal Membrane Oxygenation (ECMO)

ECMO machine functions similarly to that of the machine used during cardiopulmonary bypass grafting.

Two differing modalities of ECMO are currently in practice :

- **VA-ECMO** - connected via a vein and an artery and typically used in the treatment of acute cardiac and cardiac respiratory failure.
- **VV-ECMO** - connected to one or more veins, usually near the heart and has primarily been used for the treatment of respiratory failure.

(Appelt et al., 2020)

Due to the pressure drop that commonly occurs from the membrane, it is standard practice to connect the membrane oxygenator in series after the pump to negate subsequent pressure loss. This pressure drop has the propensity to have a direct impact on the pulsatile quality of any connected pumps. Lower pressure drops typically occur with the use of hollow-fibre membrane oxygenators and are thus more suitable than flat-sheet membrane oxygenators when used in conjunction with pulsatile pumps. The impact however of hollow-fibre oxygenators on pulsatile quality should not be considered negligible (Ji and Ündar, 2006).

2.3 Coronary Flow Analysis

In order to analyse coronary blood flow we must first isolate and fully contextualise its determinants with respect to the underlying cardiac physiology and vessel histology.

2.3.1 Rheological Properties and Mechanics of Blood Flow

Blood flow at a specified perfusion pressure is dependent on the number, size and arrangement of microvascular networks in relation to the hydrodynamic resistance present in the network. The arrangement of microvessels and geometric properties in addition to the apparent viscosity of the blood flowing through them by in large determine the resultant flow. Apparent viscosity of the blood is dependent on the distribution of suspended elements such as red blood cells. The spatial pattern of mass transport is thus influenced by flow distribution and inherent flux of contained red blood cells.

The mechanical properties of red blood cells are then an important factor for consideration in the context of blood flow behaviour especially due to their higher degree of blood composition. Blood is typically comprised of approximately 45% red blood cells and is termed *Hematocrit* (Pries, Secomb, and Gaehtgens, 1996). The cells themselves are constituded by cytoplasm which behaves as a non-compressible Newtonian fluid surrounded by a thin lipid bilayer viscoelastic membrane. These properties influence blood when aggregated in bulk shear flow to increase in density at lower shear rates. As shear rate increases, the progressive breakup of aggregates results in decreases viscosity termed *'Shear Thinning'*. Other blood cells such as leukocytes constitute a much smaller volume fraction of blood and are stiffer than that of red blood cells. This difference in mechanical property may contribute toward microvascular flow resistance according to (Schmid-Schönbein et al., 1981).

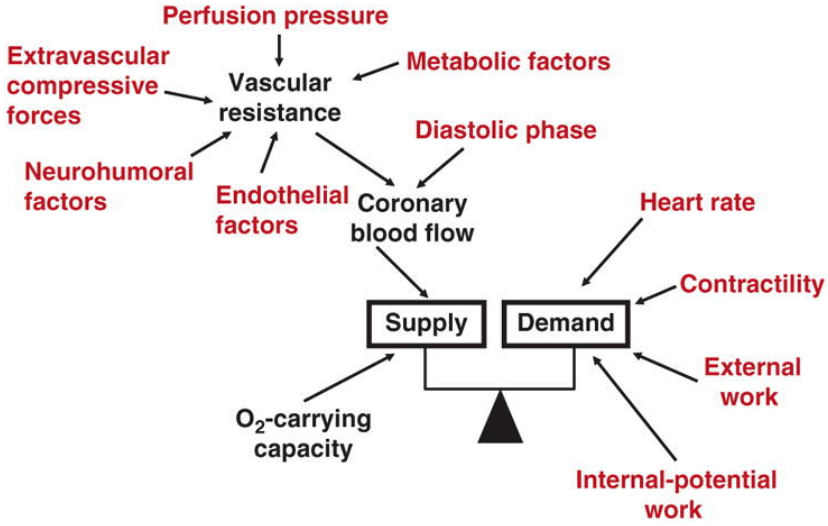

FIGURE 2.4: Factors Affecting Coronary Blood Flow (Goodwill et al., 2017)

2.3.2 Determinants of Myocardial Blood Flow

The flow of blood delivered to the myocardium depends largely on the existing pressure gradient present between the aortic root and the right atrium. The upstream pressure within the root can be thought of as the *driving pressure* and ultimately determines the magnitude of the potential pressure difference. Intra-coronary pressures have been reported to experience the greatest degree of dissipation when within the **300-100** μm diameter vessels. At this point in the vasculature, pressure typically remains constant at approximately **20-30** $mmHg$, which is sufficient to maintain an adequate gradient across the capillary network. This flow however is directly dependant on extravascular resistive forces directly related to left ventricular systolic pressure, heart rate and the contractile state of the myocardium (Schelbert, 2010).

The changes in myocardial work i.e metabolic dependant contractility, result in changes in energy demand and thus are accompanied by proportional auto-regulatory changes to myocardial blood flow through mechanistic regulation of the coronary arteries (Schelbert, 2010).

Approximating Myocardial Oxygen Balance

Myocardial oxygen demand has been established as a determinant of coronary blood flow. This is the underlying relationship governing Vasomotor tone. Oxygen delivery is thus a product of arterial oxygen carrying capacity and subsequent myocardial blood flow. In a comprehensive review of coronary blood flow physiology by (Ramanathan and Skinner, 2005), the term *Diastolic Pressure Time Index* ***(DPTI)*** is defined as a measure of coronary blood supply and expressed as the product of *Coronary Perfusion Pressure* ***(P_{cp})*** and *Diastolic Time* ***(t_d)***.

Similarly, the oxygen demand can be represented by the *Tension Time Index* ***(TTI)*** and expressed as the product of *Systolic Pressure* ***(P_{sys})*** and *Systolic Time* ***(t_s)***. Using these two terms in relation to one another yields what can be called the *Endocardial Viability Ratio* ***(EVR)*** and used as a measure of myocardial oxygen supply-demand balance. According to (Ramanathan and Skinner, 2005) a ratio of < 0.7 would be associated with sub-endocardial ischeamia. The aforementioned expressions are represented as follows

$$DPTI = P_{cp} * t_d \tag{2.1}$$

$$TTI = P_{sys} * t_s \tag{2.2}$$

$$EVR = \frac{DPTI}{TTI} \tag{2.3}$$

2.3.3 Determinants of Intra-myocardial Pressure

An earlier study by (Salisbury, Cross, and Rieben, 1962) explored the determinants of intra-myocardial pressure by investigating the relationship of left ventricular volume, coronary perfusion pressure, heart rate and finally similarly to (Kim et al., 2010) the present left ventricular pressure. Right ventricular pressure however was not considered. This was due to the nature of experimental setup where in the right heart was bypassed to direct all venous blood to be pumped through a heart-lung machine and returned by way of the left atrium. The relationship of determining

factors was assessed through comparison of measurements made during steady states when one of the controlled parameters was altered progressively while others were kept constant.

The study was able to conclude that intra-myocardial pressure tracings from hearts contracting *in-situ*, but not isovolumically produced two systolic peaks, whereas tracings from the isolated heart preparations produced only one systolic peak which occurred simultaneously with the left ventricular peak pressure. The magnitude of this peak was deemed to be related to aortic pressure, but not connected to subsequent cardiac output in the experiments carried out. The presence of two systolic peaks was presumed to coincide with peak contractile tension and maximal shortening of myocardial fibres in the non-isvolumically contracting subset. Within the physiological range of left ventricular volume, systolic pressures of the myocardium changed in the same direction in relation to variation of systemic resistance and coronary perfusion pressure. Intra-myocardial diastolic pressure however was observed to change in the opposite direction to that of left ventricular diastolic pressure, but only when left ventricular diastolic pressure was below **6 - 8 mmHg** and when cardiac performance was varied by alterations of left ventricular volume and/or heart rate. The inverse relation identified was attributed to changes of distensibility of the embedded artery segment with respect to its changing length.

In the diastolic case of lower left ventricular pressures, the subsequent relation to intra-myocardial pressure contradicts the application of the left ventricular pressure as a reasonable estimate for intra-myocardial pressure (Kim et al., 2010). It is likely that in the study conducted by (Kim et al., 2010), left ventricular pressures were simulated within the physiological range which exempts the conditional relationship uncovered by (Salisbury, Cross, and Rieben, 1962). This relationship is however relevant when considering the coupled impact on intra-myocardial diastolic pressure by varying magnitudes of heart rate, cardiac performance and left ventricular volume. The latter being of particular relevance when considering the altered state of an *ex-vivo* heart undergoing perfusion having left ventricular pressure and volumes outside of the normal physiological range. Additionally, when considering the contribution of myocardial blood flow during diastole - a case is made for the due consideration of this inverse relationship uncovered by (Salisbury, Cross, and Rieben, 1962) when analysing myocardial blood flow of the *Ex-vivo* perfused heart.

2.3.4 Coronary Perfusion Pressure

Due to the contraction of cardiac muscle tissue during systole, there is a compression and twisting of the intramuscular blood vessels that results in a reduction of flow. During systole, the intra-myocardial blood is propelled forwards in the toward the coronary sinus as well as in a retrograde direction toward the epicardial vessels. The epicardial vessels exhibit a capacitive effect on the incoming flow. Upon the onset of diastole there is a muscular relaxation that causes a resumption of flow. Impedance of flow in the epicardial vessels of the right ventricle are less pronounced because of the lesser force exerted from right ventricular contraction. The *Coronary Perfusion Pressure* (P_{cp}) can be defined as follows:

$$P_{cp} = P_{di} - P_{LVED} \tag{2.4}$$

where

$$P_{di} = \text{Aortic Diastolic Pressure}$$
$$P_{LVED} = \text{Left Ventricular End Diastolic Pressure}$$

Furthermore, because of the notable flow differences between systolic and diastolic phases, higher heart rate impinges diastolic time more than that of systolic and thus decreases total perfusion time (Ramanathan and Skinner, 2005).

2.3.5 Poiseuille's Law

The physics of coronary blood flow can be mathematically expressed using the *Hagen–Poiseuille* equation describing the relationship between pressure, fluidic resistance and flow rate as analogous to *Ohm's Law* in it's relation of voltage, resistance and current respectively. The main difference however stems from the non-slip condition applied to laminar flow (Zhang and Hoshino, 2014). The fundamental construct of the equation begins equating k to the change of pressure along a pipe segment of length l as follows

$$k = \frac{dp}{dx} = \frac{\Delta p}{l} \tag{2.5}$$

Where p is the pressure and x is the axial coordinate, positive in the direction of flow. The pressure difference Δp is measured in the direction of flow, that is

$$\Delta p = p_2 - p_1 \tag{2.6}$$

where p_1, p_2 are pressures at the upstream and downstream ends of the tube segment, respectively. Since p_1 must be higher than p_2 to produce flow in the positive x-direction, Δp is usually referred to as the *pressure drop* along the tube segment.

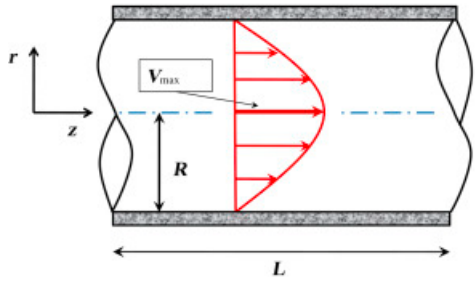

FIGURE 2.5: Parabolic Profile of Fluid Flow Through a Pipe

Equation 2.7 indicates that in Poiseuille flow, the flow rate Q through the tube given by

$$q = \int_0^a 2\pi r u dr = -\frac{k\pi a^4}{8\mu} \tag{2.7}$$

Thus, average flow velocity u is given by

$$\bar{u} = \frac{q}{\pi a^2} = -\frac{ka^2}{8\mu} \tag{2.8}$$

while maximum velocity $\bar{u}$ occurs on the tube axis where $r = 0$ and from Equation 2.9 given by

$$\hat{u} = -\frac{ka^2}{4\mu} \tag{2.9}$$

The two results show that maximum velocity in Poiseuille flow is twice the average velocity, that is

$$\hat{u} = 2\bar{u} \tag{2.10}$$

As described earlier, Poiseiulle flow is not established immediately on entry into the tube but evolves over a length of tube known as the *entry length*. Flow in that region of the tube is usually referred to as *developing flow* and an estimate of the entry length is given by

$$l_e = 0.04 N_R d \tag{2.11}$$

where d is tube diameter and N_R is the Reynolds number, defined by

$$N_R = \frac{\rho \bar{u} d}{\mu} \tag{2.12}$$

(Zamir, 2006)

By extension the *Hagen-Poiseuille* equation, based on the shear stress force occurring during flow, is a special case of the more comprehensive *Navier-Stokes* equations of fluid dynamics:

$$\Delta P = \frac{8\mu L Q}{\pi R^4}, \tag{2.13}$$

where ΔP is the pressure gradient, L is stenosis length, R is stenosis radius, and Q is the volumetric flow rate.

This physical theorem provides a potential link between a vessel's structure and its functional properties. In theory, if stenosis dimensions are accurately known, the equation yields stenosis resistance ($\Delta P/Q$), which is an intrinsic characteristic of the stenosis independent of the flow rate. If flow rate is also known, the pressure gradient can be calculated (Hirshfeld Jr and Nathan, 2020).

2.3.6 Parameterisation of Coronary Flow

Velocity and flow to the coronary arteries can be calculated based on the time-dependant average of the axial velocity component data V_{ax} over the elements located at the coronary ostia (Wald, Liberzon, and Avrahami, 2018). The mean flow rate is thus computed as an integral across the cardiac cycle as follows:

$$V_y = \frac{1}{A}\left(\int_A U_y \, dA\right) \tag{2.14}$$

$$Q = \frac{\pi d^2}{4} \int_0^T V_y \, dt \tag{2.15}$$

where

V_y = Time-dependent Average Axial Velocity
Q = Time Integration Flow Rate
U_y = Time-Dependent Nodal Velocity Component in the streamwise direction
d = Artery Diameter
A = Total Area of the elements group
T = Cardiac Cycle Time

Building on the quantification of coronary flow by (Garcia et al., 2006), we may thus define the pressure difference from the aortic root to the coronary ostia as

$$TPG_{ACo} = P_A - P_{Co} \tag{2.16}$$

where

P_A = Pressure at the Aortic root measured at a plane normal to the axial flow direction
P_{Co} = Pressure measured at the plane normal to the coronary inlet

We can thus determine the aortic-coronary pressure drop computed as above to quantify the driving pressure for *diastolic* coronary flow through the left and right coronary arteries respectively.

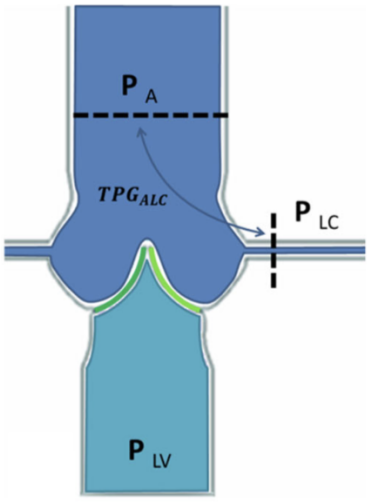

FIGURE 2.6: Pressure Measurement Planes in relation to Left Aortic-Coronary Pressure Drop Quantification (Wald, Liberzon, and Avrahami, 2018)

2.3.7 Murray's Law

Murray's Law describes the relationship between a parent blood vessel and it's branching daughter vessels by relating the cube of the radius of the parent vessel as as equal to the sum of the cubes of the daughter vessel radii. *Murray* first derived this law by defining a cost function summing the energy losses encountered by blood in a vessel with the losses of encountered by pumping blood through a vessel. This cost function becomes minimised when vessel radii remain consistent with *Murray's Law* (Painter, Edén, and Bengtsson, 2006).

The work of (Zhou, Kassab, and Molloi, 1999) has since made an effort to generalize *Murray's Law* to the entire coronary arterial tree/subtree by proposing the use of a **power dissipation function** expressed in terms of **Total Arterial Volume** (V), and the **Total Arterial Length** (L) as the new cost function as follows:

$$F(L, V) = Q_2(L)R(L, V) + kV \tag{2.17}$$

where $Q_2(L)$ is a function of L for a given pressure drop between the coronary ostia to the crown's terminal vessels, $R(L, V)$ is a function of L and V, and k is a metabolic constant of blood.

2.4 Modelling and Simulation of the Cardiocirculatory System

By modelling volumetric flow, pressure and volume in chambers of the heart and critical surrounding vessels, subsequent changes in flow conditions can be determined based on the parameterisation of flow dependent properties of the associated fluid domain. Additionally, by varying functional conditions of elements describing ventricular contractility and load to model the systemic hemodynamics of and *ex-vivo* heart can be achieved. This can be further applied to represent cases such as the organ in an *Ex-Vivo* state. In order to simulate and analyse hemodynamics of the human cardiovascular system *in-silico*, the development of a model able to emulate frequency and phase specific flow waveforms based on the the fluid dynamic principles specific to blood flow in the major vessels and chambers of the heart can be achieved by building on currently existing efforts present in literature.

Early model developments attempting to reproduce physical flow patterns within the aortic root consisted of hydraulic circuits capable of generating steady and/or pulsatile flow waveforms the likes of which were achieved by (Schichl and Affeld, 1993) through the use of a piston actuating pressure through connection to the aortic orifice. Former models such as those produced by (Bellhouse and Talbot, 1969) investigated aortic root haemodynamics with the use of rigid body vessels made from perspex or glass.

2.4.1 Mechanical Modelling of Coronary Artery and Aortic Root Dependant Flow

At the time, work produced by (Querzoli et al., 2016) sought to close what was believed to be a gap that existed based on the absence of any developed *In-Vitro* flow model of the aortic root and coronary arteries. Resulting work was able to generate a hydraulic circuit driven by a linearly actuated motor-piston complex used to regulate water flow through a prosthetic aortic valve.

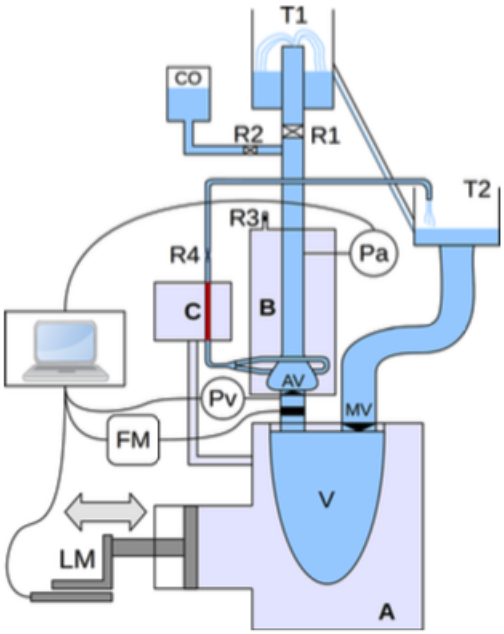

FIGURE 2.7: Pulse Duplicating *In-Vitro* Aortic/Coronary Lab Model (Querzoli et al., 2016)

This has been shown in *Figure 2.7*. This allowed for the analysis of physical coronary flow in relation to the varying pressure gradient developed across the aortic root and left ventricle with respect systolic-diastolic cycle time. Results were able to satisfy the expected flow outcomes expected in a healthy patient from an *In-Vivo* perspective.

2.4.2 Computational Haemodynamics

Fluid flow is modelled through the evaluation of the **Navier-Stokes** continuity equations iterating over each finite mesh element with respect to time. The incompressible **Navier-Stokes** equation for flow is given by

Mass Conservation Equation:

$$\nabla \cdot \mathbf{u} = 0 \tag{2.18}$$

Momentum Conservation Equation:

$$\rho\left(\frac{\partial \mathbf{u}}{\partial t} + \mathbf{u}\cdot\nabla\mathbf{u}\right) = -\nabla p + \mu\nabla^2\mathbf{u} + \mathbf{f} \tag{2.19}$$

where

$\mathbf{u}$ is the velocity field
p is the pressure
ρ is the density
μ is the dynamic viscosity
$\mathbf{f}$ is any external force

2.4.3 Lumped Parameter Modelling of the *In-Situ* Heart

The use of a model initially proposed by (Avanzolini et al., 1988) surfaces itself as a well accepted robust vehicle for use in the design and implementation of feedback control systems and thus lends itself very well for engineering utility. By simulating circulation physiology through the use of a closed loop electric circuit analog, instantaneous parameter tracking on varying time intervals assists the design methodology when applied to the implementation of a device using a feedback system directly affected by cardiovascular periodicity.

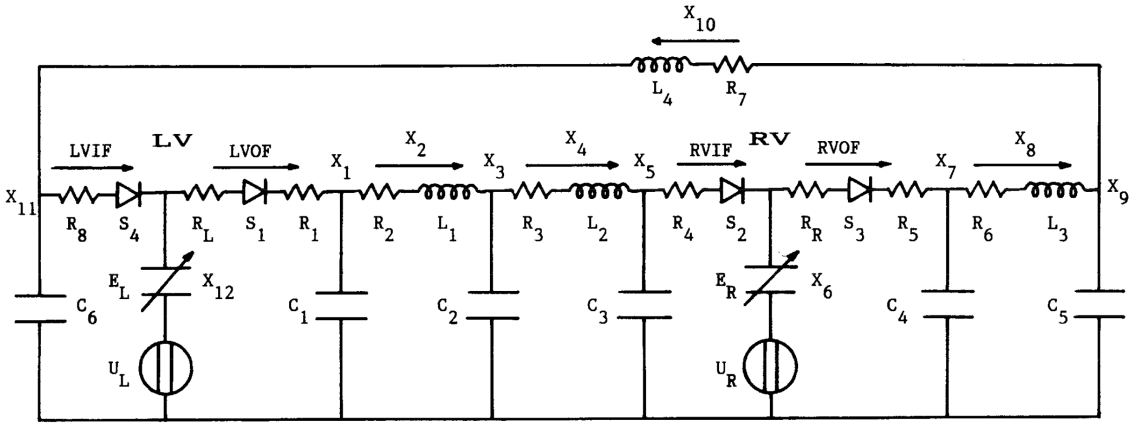

FIGURE 2.8: Closed Loop Cardiovascular System Model

The model builds on the effects of ventricular contraction on blood flow and the generation of the ventricular pulsatile pressure waveforms that determine flow. Modelling of *Excitation-Contraction* coupling was achieved by (De Canete et al., 2013), through the implementation of ventricular pressure governed by a piece wise function relating it to the rate of change of blood volume during Systole and Diastole. Ventricular pressure is thus given by

$$P_v = \begin{cases} U + E(V - V_o) + R\dot{V} & \text{(Systole)} \\ E_d(V - V_o) & \text{(Diastole)} \end{cases} \tag{2.20}$$

where

$V_r =$ Reference volume near which linearization is made
$CJ = U_{max}\cdot a(t)$, Isovolumetric Pressure at Volume $V(t)$
$E = E_d + E_a(t)$, Sum of Diastolic and Time-Varying Systolic Elastance
$R =$ Resistance due to Myocardial Viscosity

Left and right ventricular pressure signal generation can thus be implemented into the lumped parameter model by applying the ventricular piece-wise function as a block element in the circuit using the configuration shown in *Figure 2.9*

The resulting signal measurement achieved using this model can be seen in *Figure 2.10*, illustrating the relation between volumetric **Inflow** and **Outflow** of left and right ventricles respectively and the subsequent impact on **Right Venous Atrial Pressure** and **Aortic Pressure**. The presence of the dicrotic notch in proportion to duration of diastolic time present in the Aortic Pressure signal shown in the figure, verifies the expected signal/variable interdependency and justifies the models applicability for the emulation of pressure phenomena present in a clinical setting.

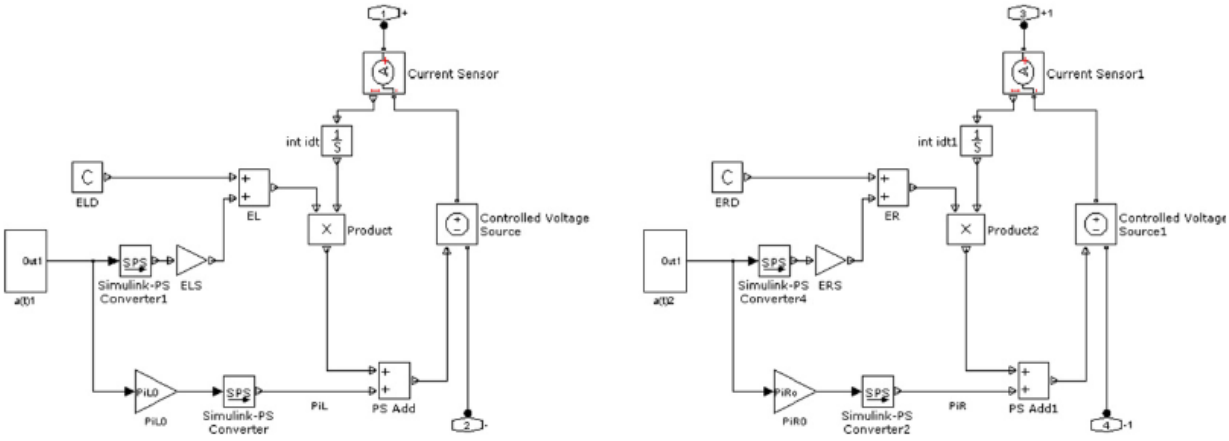

FIGURE 2.9: Isovolumetric Pressure Generation Configuration of Left (Shown Left) and Right (Shown Right) Ventricle Blocks (De Canete et al., 2013)

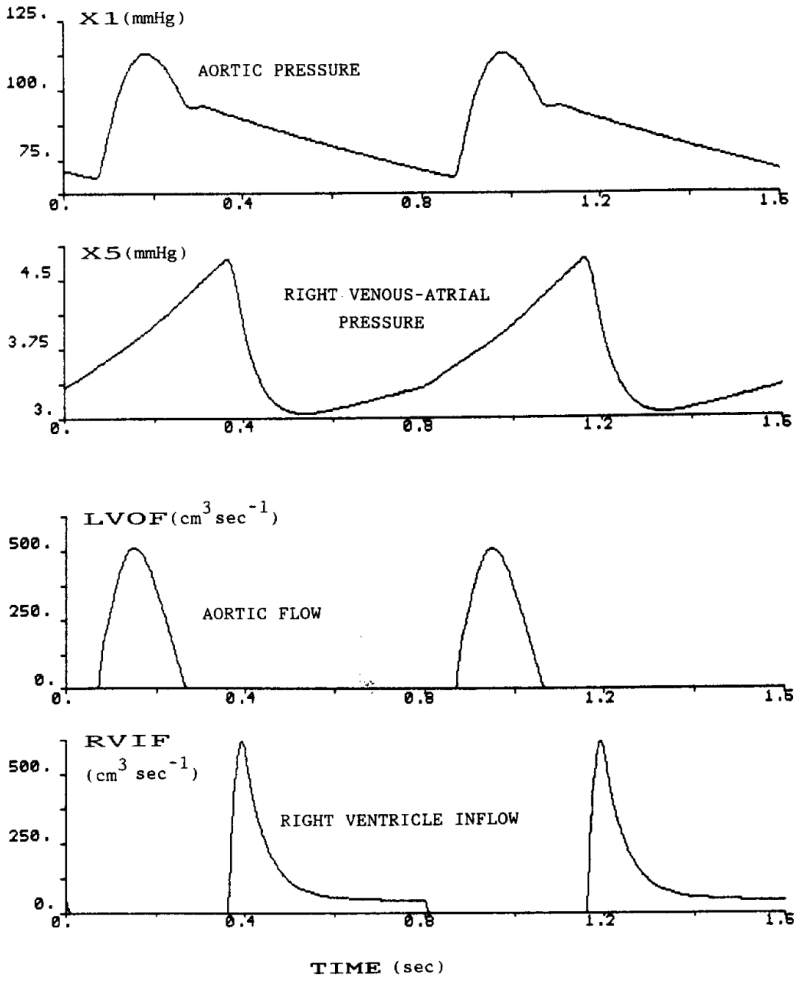

FIGURE 2.10: Time-Course of Relevant Systemic Variables in Steady-State Condition. (Avanzolini et al., 1988)

Resistance of Coronary Vascular Beds

In order to approximate accurate blood flow to the myocardium and considering the direct impact on blood flow by the pressure gradient from the aortic root across the coronary sinus, as well as the fact that resistances particularly within the coronary microvasculature vary with respect to external forces of contraction as well as internal changes of intra-myocardial pressure relative to the cardiac cycle. There is thus a requirement to simulate the downstream pressure fluctuation of coronary vascular beds in order to accurately quantify pressure gradient changes across the coronary blood flow path in order to account for the subsequent impact on flow.

A study that resolved to consider factors leading to significant flow variations was done through the patient specific modelling of coronary arteries by (Kim et al., 2010). The study proposed the use of a lumped parameter model defined at each of the respective coronary outlets coupled to an upstream three-dimensional finite element model for the implicit computation of velocity and pressure fields. The model is as illustrated in *Figure 2.11*.

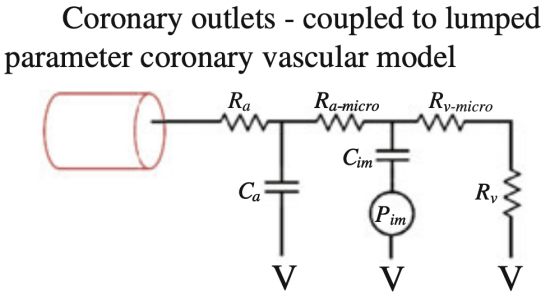

FIGURE 2.11: Modelling of Dynamic Coronary Vascular Bed Resistance (Kim et al., 2010)

The vascular bed model consists of impedance elements of coronary arterial resistance R_a, coronary arterial compliance C_a, coronary arterial microcirculation resistance $R_{a-micro}$, myocardial compliance C_{im}, coronary venous microcirculation resistance $R_{v-micro}$, coronary venous resistance R_v and intramyocardial pressure $P_{im}(t)$.

Coupling of flow and pressure fields with the upstream model was established by replacing the coronary outlet pressure P_t at each outlet surface $\Gamma_{h_{\text{cor}_k}}$ with the ordinary differential equation

$$
\begin{aligned}
&[\underset{\sim m}{M}(\vec{v},p)+\underset{\sim m}{H}]_{\Gamma_{h_{\text{cor}_k}}} = -\left(R\int_{\Gamma_{h_{\text{cor}_k}}}\vec{v}(t)\cdot\vec{n}d\Gamma\right.\\
&\left.+\int_0^t e^{\lambda_1(t-s)}Z_1\int_{\Gamma_{h_{\text{cor}_k}}}\vec{v}(s)\cdot\vec{n}d\Gamma ds\right)I\\
&+\left(\int_0^t e^{\lambda_2(t-s)}Z_2\int_{\Gamma_{h_{\text{cor}_k}}}\vec{v}(s)\cdot\vec{n}d\Gamma ds-\vec{n}\cdot\underset{\sim}{\tau}\cdot\vec{n}\Big|_{\Gamma_{h_{\text{cor}_k}}}\right)\underset{\sim}{I}\\
&+\underset{\sim}{\tau}\Big|_{\Gamma_{\text{cor}_k}}-\left(Ae^{\lambda_1 t}-Be^{\lambda_2 t}\right)\underset{\sim}{I}\\
&-\left(\int_0^t e^{\lambda_1(t-s)}\cdot Y_1P_{\text{im}}(s)ds-\int_0^t e^{\lambda_2(t-s)}\cdot Y_2P_{\text{im}}(s)ds\right)\underset{\sim}{I}\\
&\left[\vec{M}_c(\vec{v},p)+\vec{H}_c\right]_{\Gamma_{h_{\text{cor}_k}}} = \vec{v}|_{\Gamma_{h_{\text{cor}_k}}}
\end{aligned}
\tag{2.21}
$$

where

$P(t)$ = Pressure at the coronary outlet surface
$Q(t)$ = Flow at the coronary outlet surface
I = Identity Tensor

In order to quantify and initialise the parameter term for intra-myocardial pressure within the proposed model, calculated values of left and right ventricular pressure were used to represent the intra-myocardial pressures of the left and right coronary arteries respectively. Due to the pressure differences present within the left and right ventricles, the intra-myocardial pressures that affect the coronary arteries vary depending on which side of the heart they are located. Within the lumped parameter model, the calculated values of respective intra-myocardial pressure are applied in a parallel configuration as a voltage source. This is consistent with the relationship of pressure and potential difference when considering a lumped parameter model as an analog for flow modelling.

Chapter 3

Simulation and Modelling of Cardiovascular Haemodynamics

The proposed perfusion solution system adhering to the concept solution's functional requirements was modelled based on principles from existing literature and simulated using *Matlab Simscape/Simulink*. The final perfusion model was designed around the application of a pump control system exhibiting dynamic feedback pressure control to a hypothetical *ex-vivo* heart with the capability of simulating systemic haemodynamic signal data.

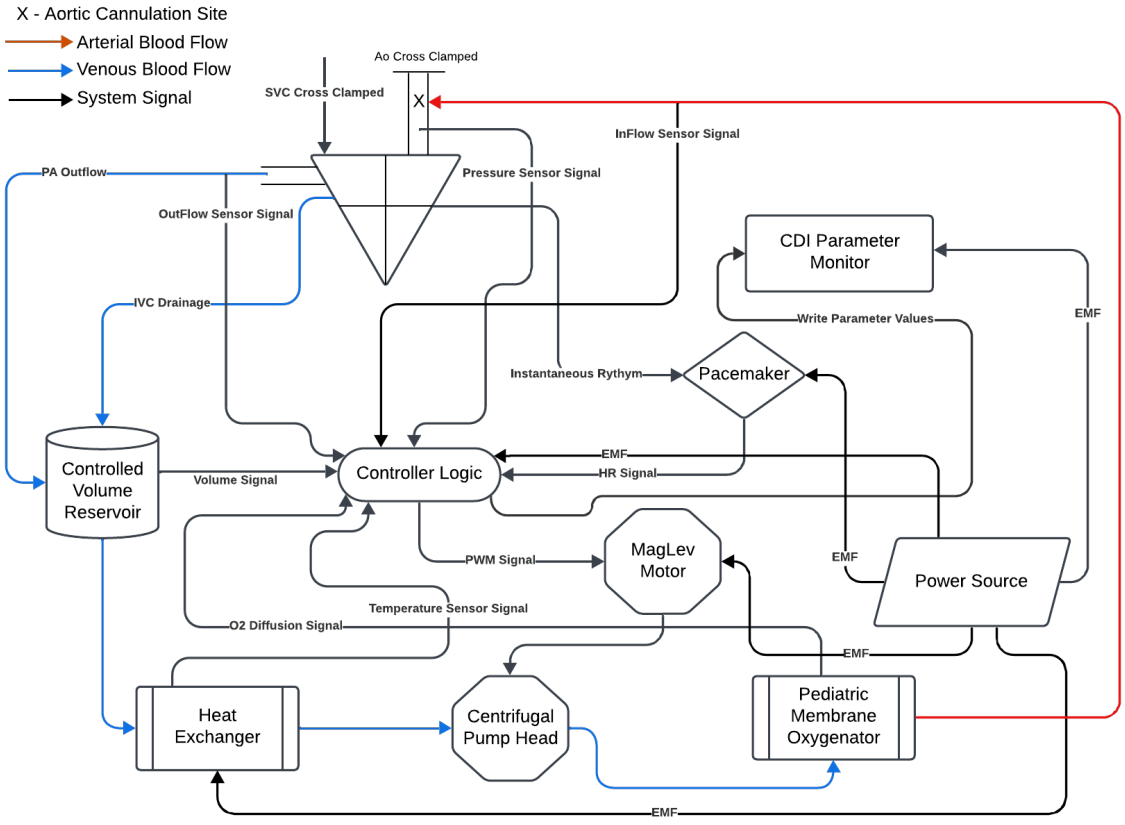

FIGURE 3.1: Systemic Concept Map

Verification of the *in-silico* perfusion model can be achieved by assessing the capability of the control loop to maintain a set target root pressure in response to different applied disturbances to the heart model presented as differing profiles of systemic resistance. The resulting heart model will then be adapted to include a coronary vascular bed element *(Figure 2.11)* with the intention of modelling blood flow out of the Aorta exclusively through the *Right Major, Left Major, Left Anterior Descending* and *Left Anterior Circumflex Coronary Arteries* along with the subsequent Aortic Root pressure changes associated with this outflow.

3.1 Systemic Modelling

Building on the generation of the system concept map shown in *Figure 3.1*, verification of the design configuration was undertaken using analysis of simulation signal data outcomes of the system model. The global system and its subsequent parameter considerations relating to blood circulation have been accounted for using a *Simscape* enabled

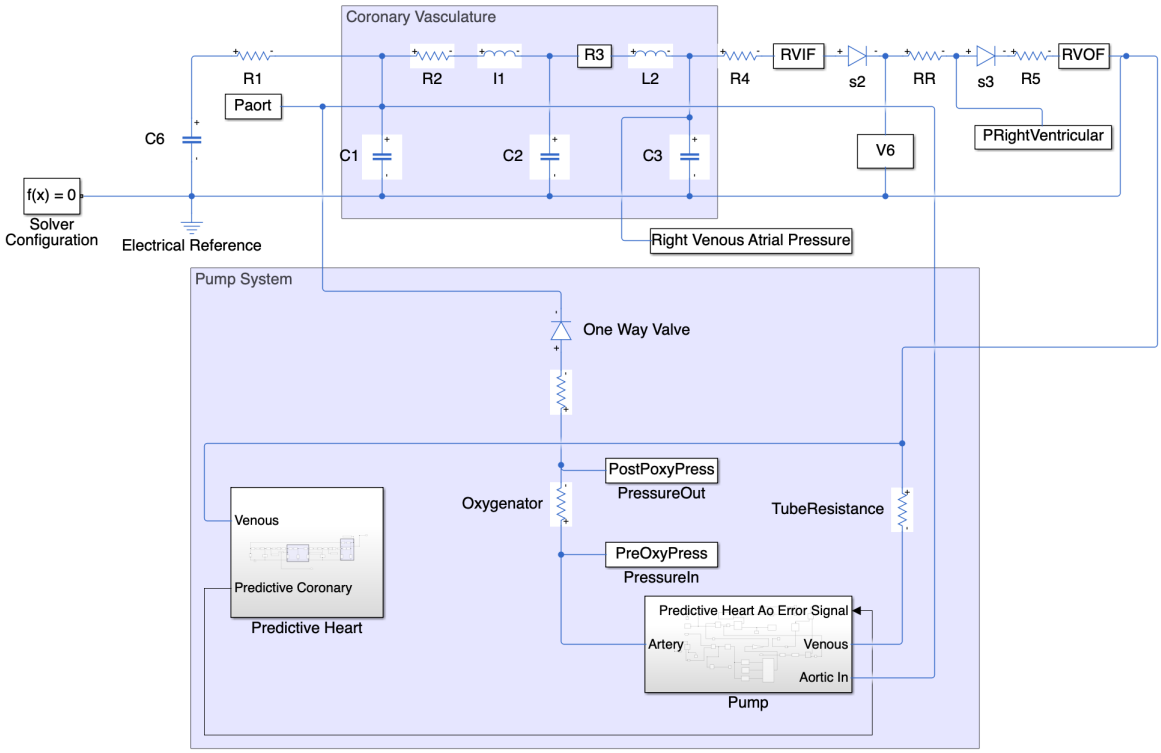

FIGURE 3.2: *Ex-Vivo* Pump Control Implementation

MatLab model developed by building on the research detailed in *Chapter 2.4.3*. Variable names, associated definitions and value used for model initialisation have been tabulated within *Appendix A.1, System State Initialisation* for reference. All values can be assumed equal to that stated in the initialisation procedure unless otherwise stated.

In order to simulate and analyse haemodynamics of a heart in the case of transplant undergoing explantation for the assisted by a perfusion device, there must be an adaptation made to the current state of the model. This would be to allow the model heart to emulate the equivalent function of a heart in the same state. To do this, it is first necessary to note the physiological and functional differences of the explanted *ex-vivo* heart. For instance, in the explanted state there will be no blood volume accumulation within the left side of the heart and thus left ventricular contractility does not result in ejection through the **AV Valve**. This changes the expected flow signal through the aortic root with respect to the model. Blood present within the Aorta however will continue to flow through the coronary arteries and systemic arteriole system, provided that present root pressure remains sufficient. Oxygenated blood then diffuses across the coronary sinus draining back into the right atrium. Blood remains present within the chambers of the right heart, but at notably lower pressure.

3.2 Development of an Antegrade Perfusion (AP) Model

Removing the contractile element responsible for left ventricular contraction within the model was the first step to negating any left ventricular flow dynamics. Once explanted, the heart is no longer connected in circuit with the pulmonary system and therefore does not fall within a closed loop circulatory system. Without a pulsatile element however, there will be a continuous loss of pressure during the simulation. Rerouting the pulmonary circulation signal to an external system modelling the oxygenation of the blood perpetuates the flow. The circuit is then closed and dynamic stability during simulation can be restored.

3.2.1 AP Model Outputs

The **AP** model configuration shown in *Figure 3.1* can be seen as an ideal perfusion model, not accounting for the ligation of the major connected vessels however. This model was configured to represent flow augmentation through the circuit system by replacing the role of the left ventricle, similar to the case of connection to heart-lung machine during cardiopulmonary bypass.

Blood flow modelled through this system makes use of the following assumptions:

1. Innertance and capacitance values of a vessels remain constant throughout the vessel's length.

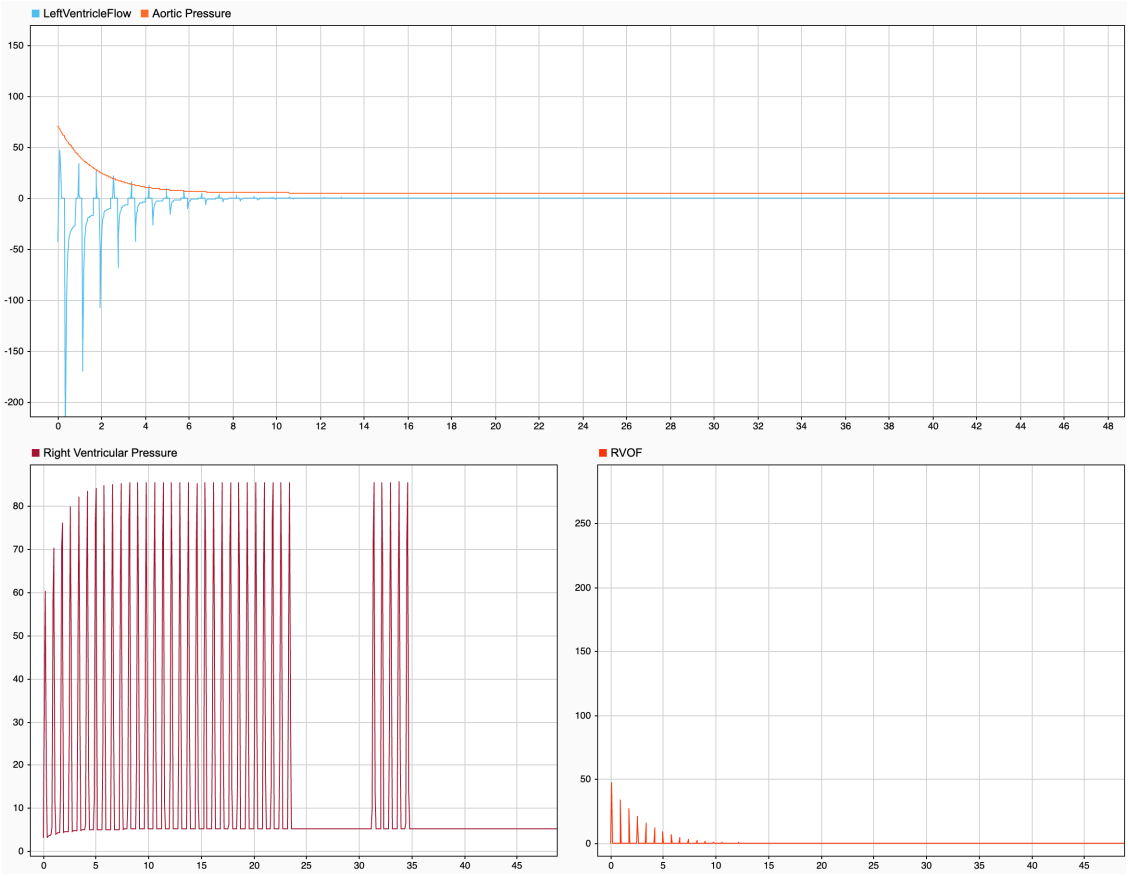

FIGURE 3.3: Signal Amplitude Degradation with respect to Time(s)

2. The heart is assumed to be present in it's normal expected *in-Situ* environment, but cannulated at the Aortic root and disconnected from the pulmonary circuit associated with the outgoing/incoming pulmonary artery and veins respectively.

3. All blood draining into the right atrium resulting in the accumulated **Right Venous-Atrial Pressure** is as a result of flow from the superior/inferior vena cava and coronary sinus.

4. The volume within the left atrium and ventricle are not included the in the fluid domain and thus remain empty.

5. Heart rate remains constant and independent of sympathetic nervous system drive removing the effect of any developed *Chronotropic Incompetency*, *Hyperaemia* and *Tachychardia*.

Systemic resistance values can be dynamically varied as a controlled variable in simulation trialing. This value represents resistance encountered as a result of downstream flow impedance through the peripheral circulatory network.

3.2.2 Implementation of Negative Feedback Dynamic Pump Control

In order to theoretically match the pulsatile pressure requirement of the heart model in question, we seek to implement a pump system that has been designed to make use of the same left ventricular contractile component from the *in-silico* model in order to approximate the required flow and pressure that must be returned to the aortic root. This logic defines the intention of the device to emulate *in-situ* haemodynamics. The left ventricular contractile element is thus placed within a circuit identical to the *in-silico* model and defined using the same initial conditions as the model being perfused. Outflow readings from the right ventricle of the modelled heart are then parsed to what will be termed the *Predictive Perfusion Model* ***(PPM)*** and used to dynamically define the instantaneous system state of the pump control element. This in essence would be the same as surgically conducting a heterotopic transplant where in the implanted heart takes over the role of ejecting oxygenated blood to the peripheral and coronary circulatory system.

The **PPM** dictates flow logic that can dynamically change in proportion to the perfused heart's requirement for a pulsatile inflow source and can be varied based on parameters governing requirement for optimal coronary

perfusion efficacy. This will be further expanded upon in following chapters. The signal can then be parsed to a pump control unit where the physical hydraulic system is modelled to approximate the aspects of sustained return flow.

Each prototype iteration builds on the previous by varying the way in which the **PPM** pump signal is translated into a viable control signal for the pump. Additionally, different variations were tested based on different circuit sensor configurations to determine the effect of differing feedback control signals on the performance of the closed loop system response. The final of the adapted model makes use of a pressure signal reference measurement at what is theoretically the cannulation site at which pump flow is directed into the Aorta. This forms the basis for all arterial blood flow monitoring. The corresponding venous measurement is achieved through the use of a flow sensor situated hypothetically at the ejection site of venous drainage which in this case would be the base of the pulmonary artery.

It should be noted that the configuration of the solution system for simulation trialling according to *Figure 3.2*, positions the oxygenating circuit element between the pump and the cannula inlet. In practice, having the oxygenator element in this position results in a pressure drop from the oxygenator to the cannula. The resistance of the oxygenator is modelled as a fixed constant and initialised pre-trial, and thus has no significance in control system operation other than introducing a constant disturbance from the time simulation begins.

Dynamic Negative Feedback Control Logic

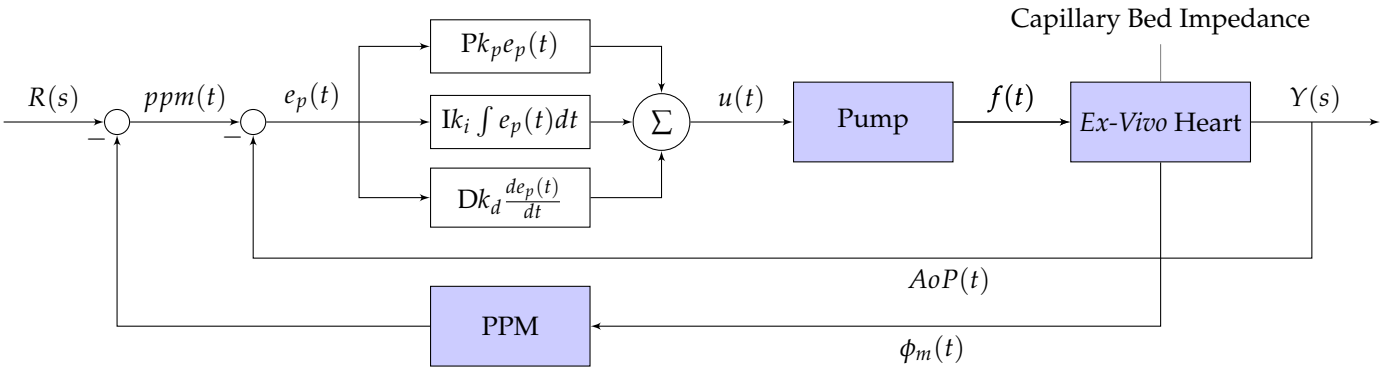

Signals illustrated in the Closed Loop Feedback Diagram are defined as follows:

- $R(s)$ = Target Reference
- $ppm(t)$ = Predictive Model Pressure Signal
- $e_p(t)$ = Transient State Pressure Error Signal
- k_p = Proportional Gain
- k_i = Integral Gain
- k_d = Derivative Gain
- $u(t)$ = Pump Control Signal
- $f(t)$ = Volumetric Pumpflow Signal
- $\phi_m(t)$ = High Frequency Phase Measurement
- $AoP(t)$ = Aortic Root Pressure Measurement
- $Y(s)$ = Transient State Output

In order to understand how fluid would effectively behave in this system, it is necessary to not only simulate and observe varying flow signals using an electrical analog equivalent but, additionally to incorporate a hydraulic model that can approximate isothermal liquid behaviour with more specificity in relation to system functional requirements. As previously stated, blood has been modelled in this system as an isothermal liquid, meaning that the flow characteristics of the liquid modelled are not subject to varying temperature. Due to the main requirement of the global model to simulate flow as a result of system feedback integration, the physical flow signal is not included in the negative feedback loop of the controller. Feedback control is thus achieved using the developed torque-signal distributed to the pump and is thus independent of physical fluid behaviour in the hydraulic aspect of the system. Fluid specific behaviour in the circuit will be discussed in the following chapter.

As illustrated in *Figure 3.4* showing an expansion of the pump system, the electric signal circuit has been coupled with a simple hydraulic model which is designed to transmute the calculated feedback signal into a motor torque

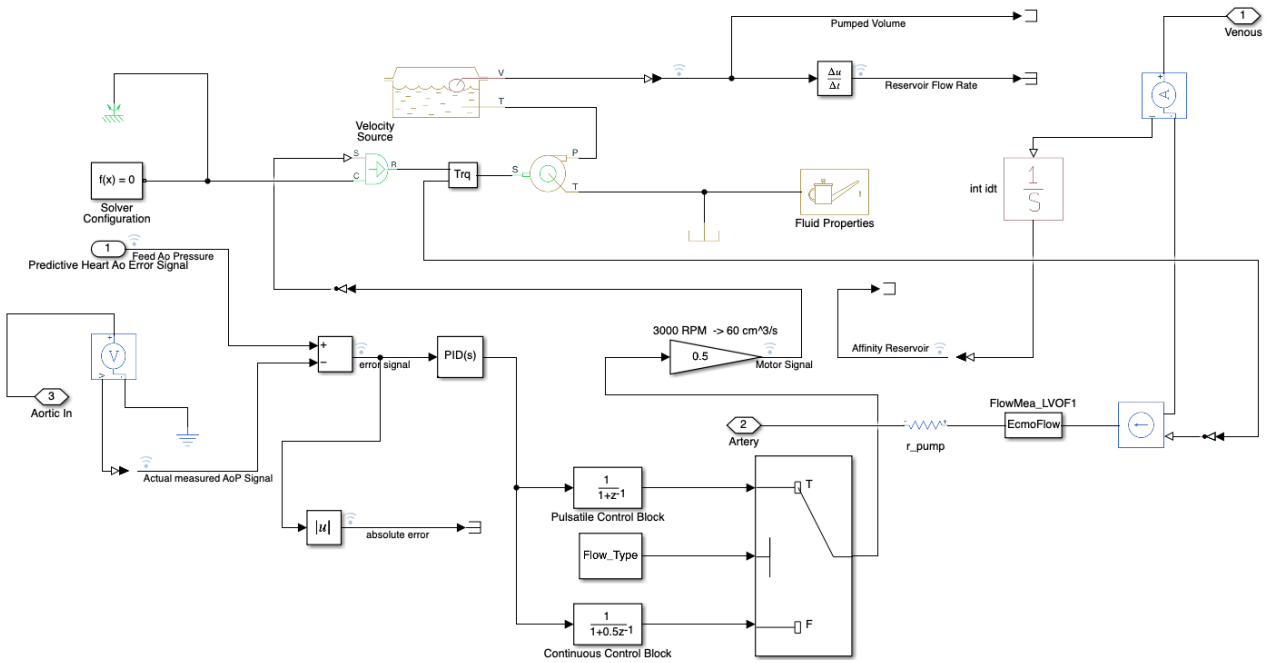

FIGURE 3.4: Pump Control Unit Subsystem

parameter measured across an ideal rotational velocity source. This signal then drives centrifugal pump actuation in order to parameterise the fluid flow from an ideal fluid source into a constant head reservoir. This allows for the analysis of changing reservoir volume as a result of pump control feedback with respect to time. The volume signal represents the idealised cumulative volume of blood pumped into the aortic root and has not been modelled subject to any impedances such as tube resistance or gravitational force. However, within the electric circuit analog system, tube resistance, pump resistance, valve resistance as well as pressure loss across the oxygenator have been accounted for. The system makes the assumption that the oxygenation device accounted for is a membrane oxygenator. In this case, it is essential to account for a pressure drop across the membrane and thus the **Pre-Oxygenation Pressure** and **Post-Oxygenation Pressure** have been used to model the resulting **Aortic Pressure** and pumpflow accounting for flow measurement prior to losses encountered by pump resistance. This modelling configuration is shown in relation to the pump system block in *Figure 3.2*.

3.3 Variable Pump Flow Profile Characteristic

Due to the inherent periodicity of the cardiac cycle we have developed pump operation in such a way that the effect of both a continuous as well as pulsatile flow profile can be analysed to determine any potential marginal utility of one flow type over another from the perspective control response.

3.3.1 Continuous Flow Response

Using a continuous flow of blood driven by control over the pump, the system is able to dynamically vary the flow rate leaving the pump based on the signal feedback of the instantaneously accumulated Aortic Root pressure. A continuous input flow profile allows for faster convergence toward the required input flow rate because the lack of pulsatility results in a faster build up of pressure. This means that the system is able to reach a steady-state and create stability with higher efficiency. In the context of organ perfusion, reaching a stable state as fast as possible is of highest priority when it comes to efficiently preserving the tissue with the adequate requirement for blood-oxygen delivery.

3.3.2 Pulsatile Flow Characteristic

In order to invoke a pulsatile characteristic to the flow profile fed into the heart model, the system has been designed with the use of a **(PPM)** which functions to track the frequency of flow exiting the right ventricle of the heart. The delineation of this signal thus defines the time points at which the pulmonary valve opens and closes as a result of right ventricular ejection. We make the assumption that both left and right ventricles are contracting at the same time, which is a reasonable approximation based on left and right myocardial activation triggered by the sino-atrial

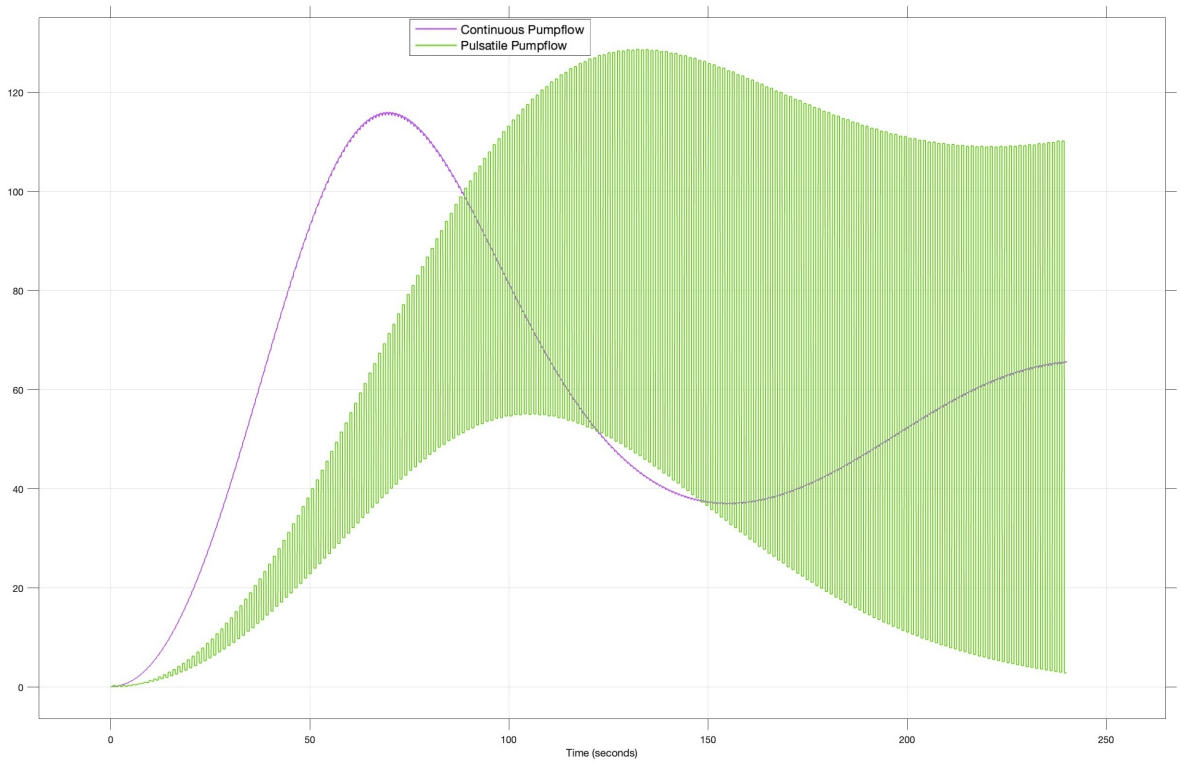

FIGURE 3.5: Pulsatile vs. Continuous Pumpflow Comparison

node. The method of flow signal frequency measurement can thus be implemented by applying the same logic employed in this model using hypothetically positioned flow sensors located at the pulmonary ostia.

The same time course delineation could be achieved *in-vivo* through the use of a pacemaker signal in conjunction with the same logic employed in the **PPM** to match phase of pump flow with that of the perfused beating heart.

The **PPM** model element thus uses the frequency of signal measured from blood leaving the right heart of the perfused organ to determine the frequency of the pulsatile characteristic needed by the pump in order to emulate the profile of flow expected from the organ's left ventricle. In essence, the **PPM** elements uses dynamic measurements of the perfused organ to assist the pump in copying the function of the organ's left ventricle so as to optimally provide pump feedback in a manor that simulates the *in-situ* state of the organ as similarly as possible. This is consistent with the theory previously discussed around concepts for optimal organ perfusion.

3.3.3 Continuous-Pulsatile Response

This flow-profile concept builds on the logic of optimal convergence toward the required flow rate necessary to establish an aortic root pressure that stabilises the organ's state of preservation using a continuous input, after which the flow profile is gradually transformed to include an element of pulsatility with the aim of further optimising myocardial oxygen delivery by maintaining the accumulated aortic pressure.

A continuous-pulsatile flow function has been created in this system through the use of the same pulsatile flow logic previously mentioned, but augmented using a discrete filter in order to create *Pulse Width Modulation* ***(PWM)*** for the purpose of simplifying the pulse variability in a manor that can be matched by rotational velocity source driving the pump. This pulsatile aspect of the flow profile works in synergy with the PID motor control in order to variably scale pump flow as in the previously mentioned continuous flow response. The parameters of the discrete filter can be varied experimentally to invoke varying degrees of magnitude in each pulse.

Pulse amplitude variation will not directly affect the system's capacity to drive mean aortic pressure to the targeted value, but will however affect the system's requirement for tuning in order to achieve **gain** and **phase margin's** consistent with improved transient state performance. In essence, the system is able to create a continuously varying flow waveform that has a pulsatile profile in phase with varying coronary blood flow. The same varying blood flow that would be expected as a result of changing epicardial constriction and pressure gradient variation associated with systolic-diastolic pressure fluctuation within the Aorta. The pulsatile logic thus aims to sync flow with the perfused organ's cardiac cycle thus leveraging the downstream pressure gradient changes in the coronary vascular beds previously discussed.

It can be seen according to *Figure 3.6* with reference to the pulsatile pumpflow signal illustrated in green, that the magnitude of pulsatile gain proportionately increases as a function reducing negative feedback error i.e the closer to

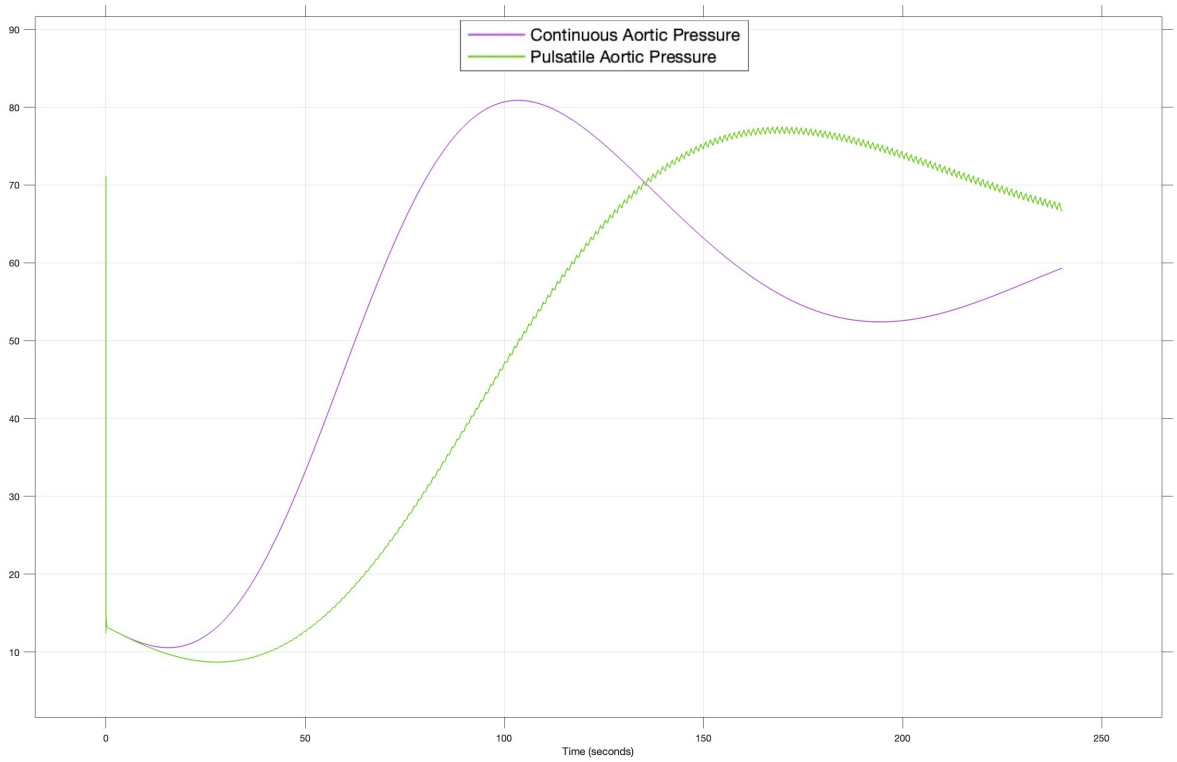

FIGURE 3.6: Pulsatile vs. Continuous Flow Effect on Developed Aortic Pressure in the absence of Coronary Resistance

the system is to reach steady state convergence, the greater the magnitude of pulsatility. This ensures that the system is able to reach the necessary *Root Mean Square* ***(RMS)*** perfusion pressure, before attempting to increase magnitude of each pulse.

This distinguishes the resulting mean perfusion pressure as the driving metric for feedback response. The range of pulsatile amplitude and the rate at which the system scales the value results in it's own dynamic convergence toward an optimal steady state value and is thus also a transient state variable parameterised by the coefficient of **z** within the denominator of the flow control blocks seen in *Figure 3.4*. Simply put, for as long as the absolute value of overshoot and undershoot of the RMS perfusion pressure decreases with each crossing over of the targeted steady state value, the system proportionally scales the pulsatile gain ultimately seeking to reduce the duration until the next target crossing, which is indicative of convergence.

Inevitably, depending on the chosen coefficient of pulsatility previously stated, the system will converge to a purely pulsatile flow feedback profile once the required gain has been established in relation to the resultant **RMS** perfusion pressure. In this way, the system has been designed to leverage an initial continuous feedback response to improve the time taken to reach a steady state, after which it then transitions toward a purely pulsatile characteristic for steady state maintenance and optimal *in-situ* state perfusion emulation.

3.4 Disturbance Based Control Verification

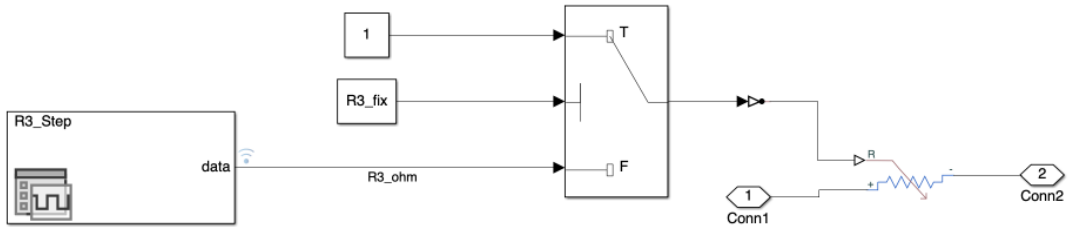

FIGURE 3.7: Varying Resistance Signal Input Configuration

In order to verify the systems's capability to dynamically converge toward the desired steady state using negative feedback across a PID component, we introduce a range of distinct varying disturbances that trigger the different requirements for pump feedback. A measure of feedback efficiency may then be computed in the context of varying pump modality in response to varying disturbances.

In reality, the heart has a dynamically varying coronary resistance due to functional and geometric changes within the coronary vascular beds *(See Chapter 2.4.3)* during the cardiac cycle. This resistance thus varies respectively and is thus periodic. To evaluate system function we consider the impact of variable downstream resistance. Three different resistance signals were implemented as inputs to a variable resistor within diagram block **R3** as seen in *Figure 3.7*.

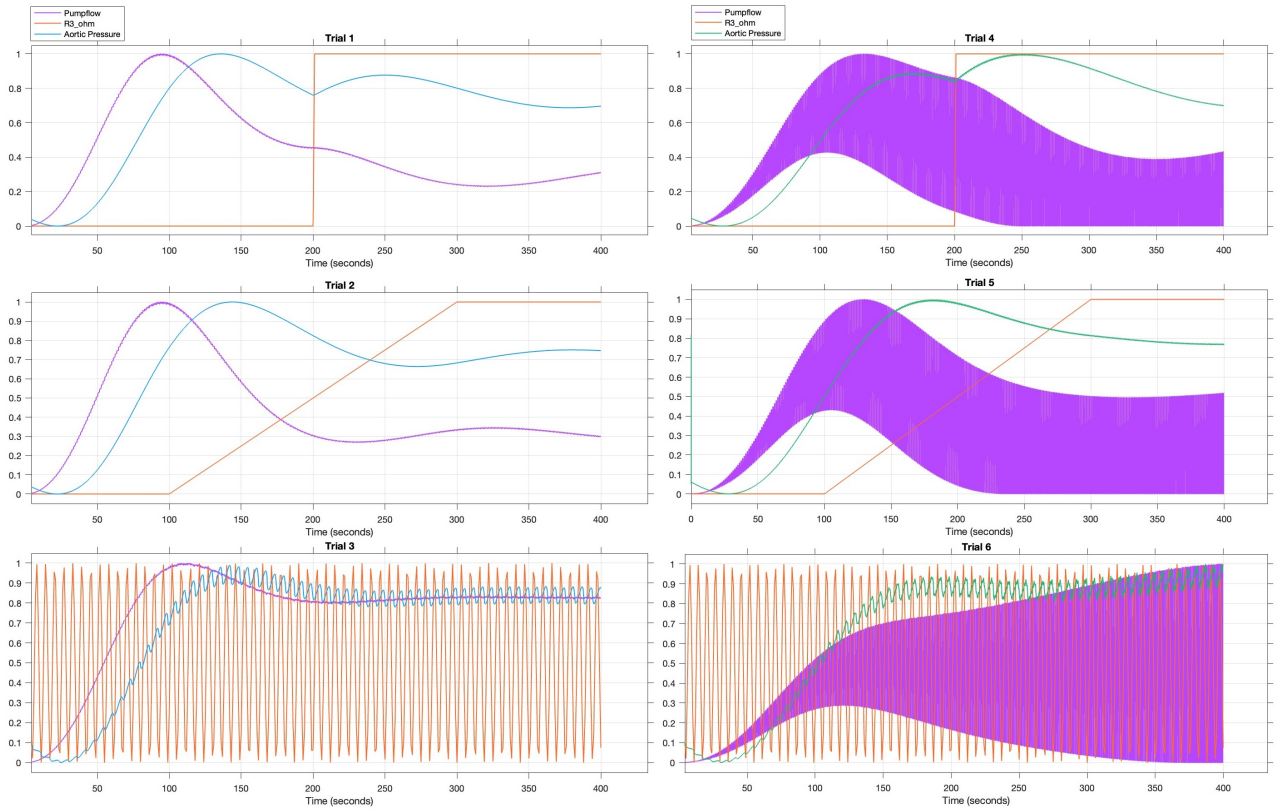

FIGURE 3.8: Continuous and Pulsatile Trial Runs with respect to varying Resistance Types

Each signal length was specified over the chosen simulation run time domain, which in this case was selected to be **400 seconds**. This time was chosen because it is approximately the duration of time the system takes to reach steady state convergence in the absence of disturbances using a continuous pump flow with and added buffer to account for additional convergence expected when introducing disturbance. Thus **400 seconds** allows for an adequate measurement window in which to measure disturbance affected responses and creates an empirical contrast with non-disturbance tested system performance.

3.4.1 Step Function Resistance Input

A step function for the resistance input was initially tested to determine the effect that a sudden change of resistance will have on resulting aortic pressure as well as other system variables that affect pump control response. By determining the impact of instantaneous changes in resistance using a step-function that invokes only one significant variation, we may better come to an initial understand of how pump control is affected. This is essentially an effort to isolate the impact of variable resistance before analysing system behaviour in response to more complex cases of systemic variability.

3.4.2 Linearly Increasing Resistance

The aim of determining system response in relation to an linearly increasing resistance is to determine how feedback control of the system responds to what is in essence the simulation of a degrading state of stability within the hypothetically perfused organ. As resistance gradually increases, this can be considered analogous to detrimental physiological changes within the organ. This could hypothetically represent a case of sudden haemorrhage and/or thrombosis within the coronary vasculature. While the onset of these occurrences is not expected in a heart that has been considered healthy and viable for transplant, the system must be designed based on considerations that account for ideal and non-ideal cases.

3.4.3 Sinusoidal Resistance

Due to the periodic nature of *in-vivo* disturbances, the sinusoidal signal is likely the best emulation of coronary resistance. The propensity for the system to execute both continuous and pulsatile feedback response varies the degree to which convergence criteria can be satisfied with respect to trial time. In order to assess the impact of this and determine any marginal utility present using a pulsatile input flow signal, all three resistance scenarios were tested against both the continuous and pulsatile flow variations of the system.

3.4.4 Feedback Control Performance Analysis

Simulating both the pulsatile and continuous-pulsatile pump flow modalities against each of the three varying coronary resistance input function yields the six experimental results illustrated in the normalised plot in *Figure 3.8*. Factors defining the parameters of effective control feedback were measured in the case of each trial and tabulated in *Table 3.1*. Where "*Variation (Flow Type)*" is shown as "*(FALSE)*" this denotes a continuous flow trial and continuous-pulsatile conversely in the case of "*(TRUE)*".

Determination of Endocardial Viability Ratio

In order to quantify and approximate system perfusion from the perspective of global system pump function, we require to determine a measure for blood oxygen delivery to the myocardium with respect to time and dependent on the flow profile exhibited during system response. Drawing on the theory discussed in *Chapter 2.3.2*, we can resolve perfusion efficiency to a measure of approximated myocardial oxygen delivery in relation to theoretical demand using **EVR**. In order to use this metric there must be a measurement of *Coronary Perfusion Pressure* with respect to time.

Taking note of the blood flow path during diastole from the ostia of the coronary arteries in the aorta to the coronary sinus and draining into the right atrium, we may thus derive perfusion pressure using the pressure gradient defined along this path. Therefore, the aim was to calculate the pressure across the coronary vasculature from the Aorta to the right atrium at the initiation of diastolic onset.

Due to the organ being in a state of perfusion, there is no aortic pressure that can be measured for accurate signal delineation. Instead we make use of the **PPM** element to approximate the left ventricular pressure signal and use it to define the phase of the perfused organ. This is the same signal used to sync the pump control with the organ's ventricular contraction. *Algorithm 1* was used to calculate the pressure differential between the *Right-Venous Atrial Pressure* and the *Aortic Pressure* at the approximated onset of diastole as determined through the delineation of the *Predictive Left Ventricular Pressure* signal from the **PPM** signal element. The delineation of the *Predictive Left Ventricular Pressure Signal* was achieved by analysing the signal to determine three distinct points being the **systolic onset**, **peak** and theoretical **dicrotic notch** and the subsequent points in time at which they occur with respect to each passing cycle.

By then using these time points defining cardiac phase applied to the signals in question we are able to determine a measurement of each pressure signal at the point in time at which coronary blood flow is theoretically in effect. The resulting coronary perfusion pressure is calculated as a vector in *Algorithm 1* (See *Appendix A.5*). This in essence measures coronary perfusion pressure as the aortic pressure change during isovolumic relaxation.

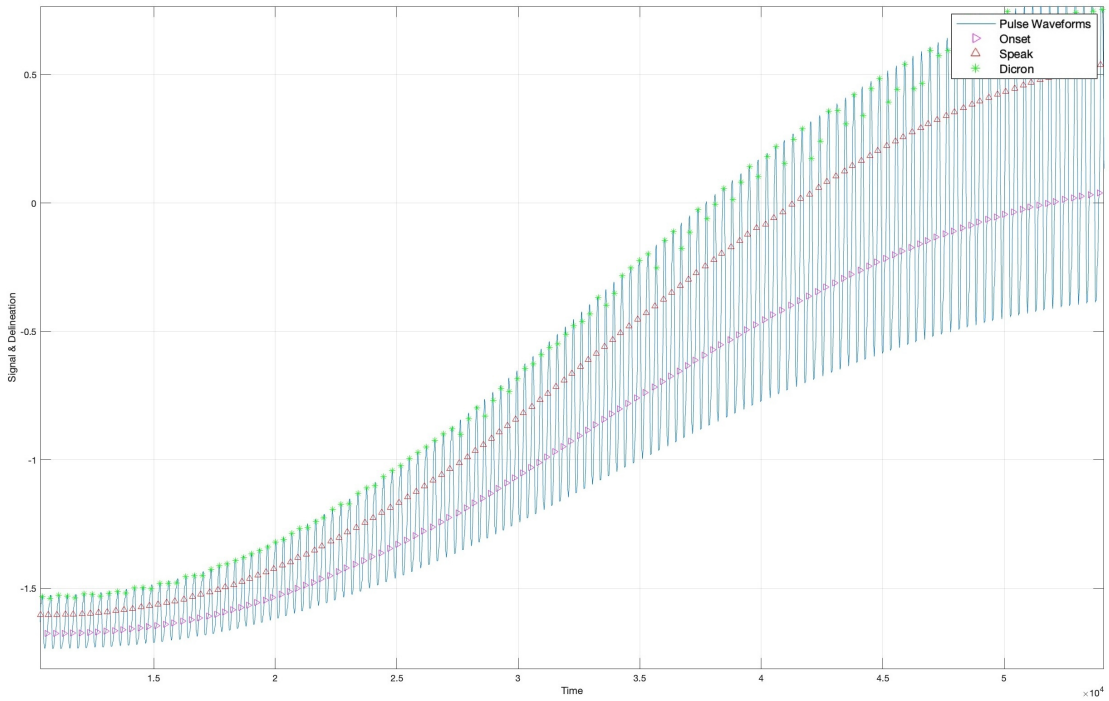

FIGURE 3.9: Predictive Left Ventricular Delineation Points applied to Right Venous Atrial Pressure Signal

The algorithm calculates the point of diastolic onset by applying the proportionate ratio of systolic time (t_s) to total elapsed time over one cycle (t_c). Assuming left ventricular pressure and aortic pressure peak at approximately the same point during systole and that the peak occurs at approximately median systolic time, the peak values ($Pressure_{peak}$) are calculated using the predictive signal and shifted one half cycle forward in time. This yields the theoretical point of diastolic onset, labelled as **dicron** in *Figure 3.9*.

Trial Outcomes

Observing the results of each of the six respective trials, it is evident that each type of pump flow characteristic is better suited to each specific use-case from the perspective of the time taken for the measured feedback signal to converge within the **0.02-Settling Time**. This variable effectively parameterises the rate at which the system response in each respective trial is able to reach a steady state and stabilise the organ at its required target perfusion pressure, in spite of the resistance disturbance function applied in each case. The associated trial settling time and degree of overshoot is illustrated in *Figure 3.8*

Parameter	**Trial 1**	**Trial 2**	**Trial 3**	**Trial 4**	**Trial 5**	**Trial 6**
Variation (Flow_Type)	(FALSE)	(FALSE)	(FALSE)	(TRUE)	(TRUE)	(TRUE)
Resistance Type (R3-Fix)	Step	Linear	Sinusoidal	Step	Linear	Sinusoidal
Mean CPP	59.55	59.81	53.77	65.98	65.08	55.52
Mean EVR	1.383	1.384	1.350	1.388	1.389	1.362
Rise Time	0.00	0.00	100.62	0.00	0.00	144.05
Transient Time	345.30	342.58	202.55	386.29	341.23	354.91
Settling Time	343.46	339.80	200.70	384.84	337.18	353.17
Settling Min	9.52	9.52	54.37	8.68	8.68	63.22
Settling Max	77.44	80.75	67.18	86.09	85.10	70.34
Overshoot	36.30	28.81	11.22	36.70	25.86	0.12
Undershoot	0.00	0.00	0.00	0.00	0.00	0.00
Peak	77.44	80.75	67.18	86.09	85.10	70.34
Peak Time	138.16	144.70	141.48	236.78	167.60	391.65
Sim Time	400.00	400.00	400.00	400.00	400.00	400.00
Heart Rate	100.00	100.00	100.00	100.00	100.00	100.00
Gain	0.50	0.50	0.50	0.50	0.50	0.50
Target	60.00	60.00	60.00	60.00	60.00	60.00
Target Residual	0.45	0.19	6.23	5.98	5.08	4.48

Parameter	Trial 1	Trial 2	Trial 3	Trial 4	Trial 5	Trial 6

TABLE 3.1: Summary of Experimental Trials

It should be noted that the continuous flow trials outperformed the continuous-pulsatile trials in the case of step and sinusoidal resistance, but not however in the case of the linearly increasing resistance.

Taking note of the effect that each input resistance signal exhibits on the corresponding aortic pressure, it can be observed that an increase in coronary resistance results in an increase in accumulated upstream aortic root pressure. By extension, an increase or decrease in coronary resistance and the subsequent effect on aortic pressure results in a proportionately opposite requirement for hydraulic work delivered from the pump. This is evident when observing the pump flow response to decrease in *trials 1 and 4* at the point in which the resistance steps up in relation to the aortic pressure.

Observing the respective **EVR** values of each trial run, it is evident that the result measured **(> 1)** in each case, indicates that theoretically, there is a greater supply of blood-oxygen than the corresponding demand of the hypothetical heart being perfused.

Due to the required oxygen demand of the organ being largely dependent on the degree of contractile myocardial energy expenditure, it should be emphasised that this metric represents an attempt to parameterise perfusion in a pragmatically oversimplified way. A true quantification of myocardial oxygen demand relies on the ability to measure the degree of myocardial work and resultant blood lactate as a result of cellular metabolism. **EVR** in the case of this trial however purely aims to qualify perfusion according to measurement at discrete points in the cardiac cycle that correlate with the degree of what actual blood-oxygen delivery would be if measured in a real-life test. Therefore, in the context of this simulation model, **EVR** represents system pump flow function from the perspective of the hypothetical perfused heart's requirement for diastolic blood-oxygen delivery.

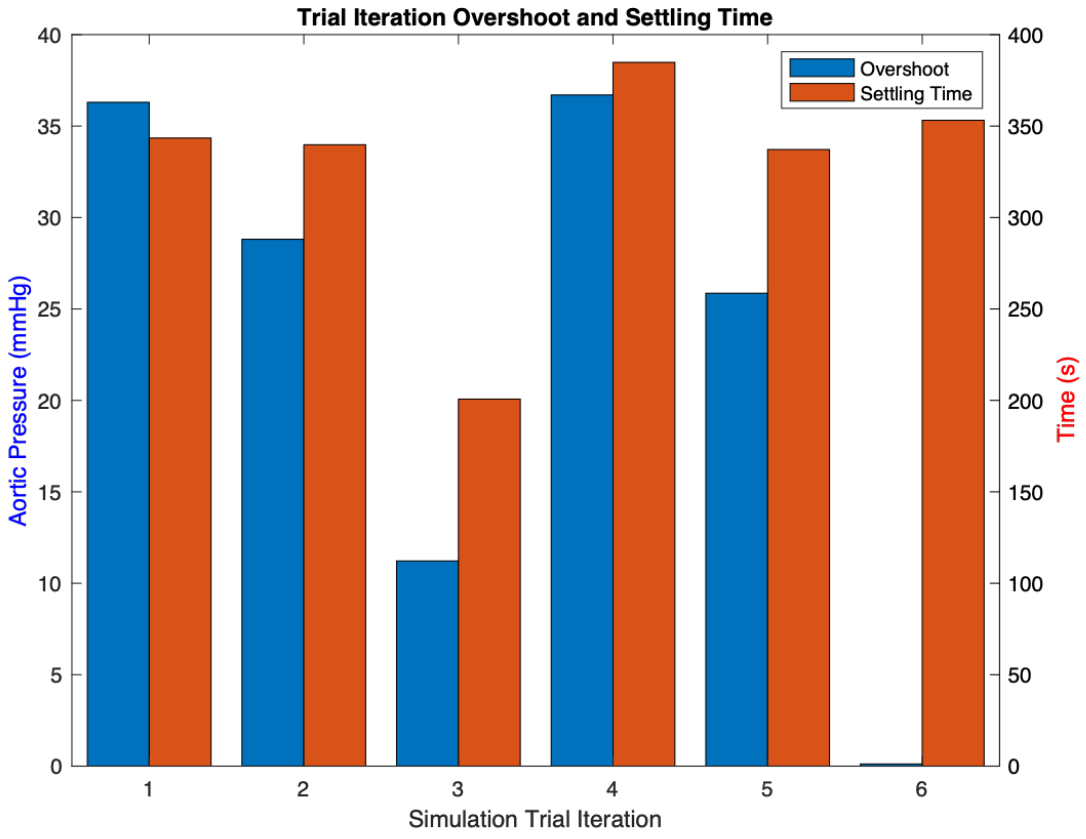

FIGURE 3.10: Respective 0.02-Settling Time and Overshoot of Respective Trial Runs

Taking the above into consideration, the greatest degree of hypothetical myocardial blood delivery is associated with *trial 5* where in the continuous-pulsatile modality is used in response to the linearly increasing resistance signal. This trial is also associated with the lowest overall settling time measurement. We can see that by observing settling time as a measure of the system's capacity to efficiently achieve stability there may be a correlation with the effectiveness of resultant perfusion when considering the associated **EVR** measurement.

An important observation comes when considering results of both flow types with respect to the sinusoidal resistance input. Bearing in mind that results of the sinusoidal resistance trials should be considered with larger

weight in the context of overall system operational effectiveness because of the higher degree of clinical relevance that this resistance signal has when aiming to emulate expected *in-vivo* coronary resistance. Observing the degree of noise present in both aortic pressure signals, it is evident that using a *0.02-Settling Time* metric would be an inaccurate way of quantifying the control response efficacy because the level of noise present within the respective signal has an amplitude that falls outside of the **2%** cutoff mark. In this case, we have used a measurement of **Signal to Noise Ratio (SNR)**, to trigger the system to measure the respective response parameters of the aortic signal augmented with a *3rd Order Bessel Filter*. This aims to eliminate the high frequency noise component that causes the signal to fall outside of the *0.02-Settling Time* range.

When considering results of *trial 3* and *trial 6*, in relation to one another we notice that the Mean EVR measurements differ by approximately **0.012**, while settling time differs by as much as **152.47** seconds. In the context of perfusion where organ stability is of primary concern, minimising settling time is thus a priority. *Trial 3* data indicates that a continuous mode of pump flow produces favourable settling time while providing a very similar degree of blood-oxygen efficiency as the continuous-pulsatile trial result. This result concludes that in the case of a sinusoidal resistance input where system performance results in largely different rates of stabilisation, myocardial oxygen is hypothetically delivered with greater effectiveness when perfusion is facilitated using a continuous input flow waveform.

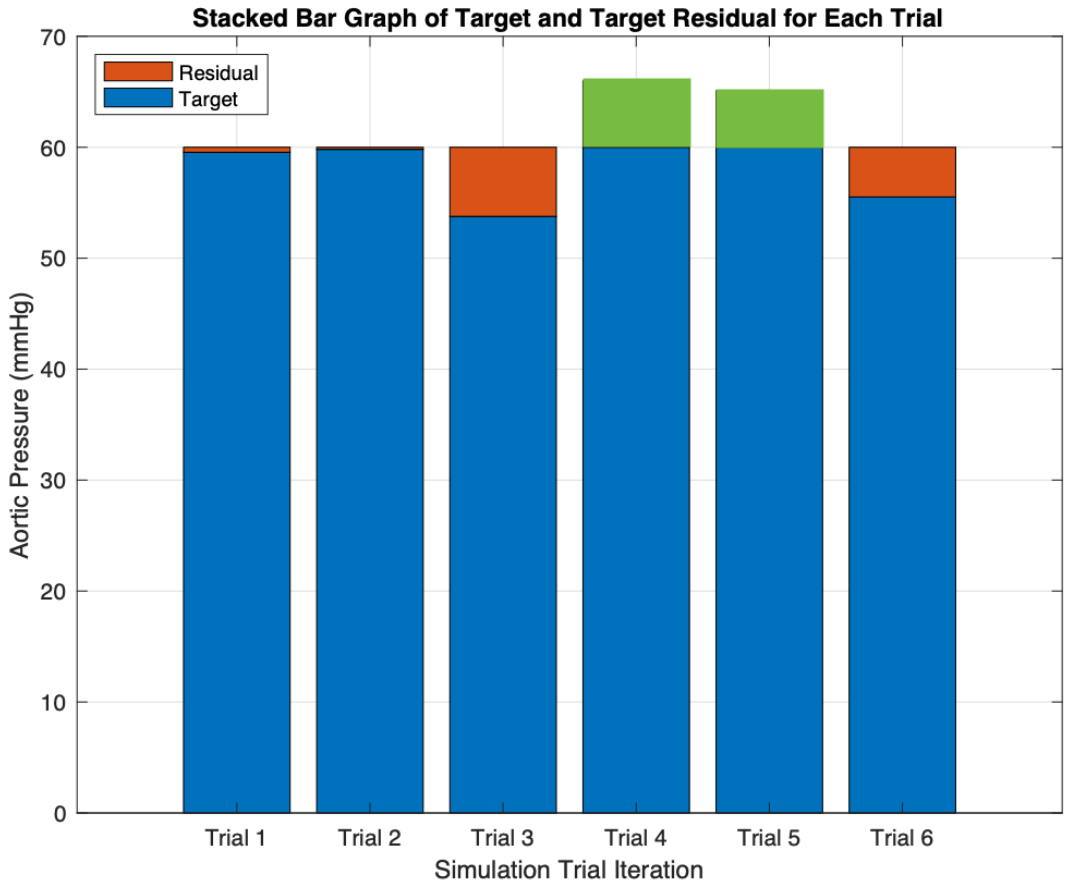

FIGURE 3.11: Final Value Residuals in relation to Target Coronary Perfusion Pressure

When taking note of the resultant mean coronary perfusion pressure of each trial we can supplement settling time data to get a better idea of control response with respect to simulation time. Referring to *Figure 3.11*, where mean coronary perfusion pressure is plotted in relation to chosen trial target pressure value, we notice that the continuous flow *trials 1* and *2* exhibit mean pressure values with the lowest degree of variance from the steady-state target value. Residual values above the **60 mmHg** target have been illustrated in green, while residual values below target are shown in red. *Trial 3* however, results in a higher target residual value of **6.23**, which is expected when considering the resulting periodic profile of developed aortic pressure. *Trial 6* displays the same degree of residual variance in comparison to the other continuous-pulsatile trial results. The greatest degree of target accuracy can thus be attributed to trial flows that result in an aortic pressure profile with the least amount of high frequency noise. Due to the periodicity of the resulting aortic pressure signal in *trial 3*, residual results are closely related to that of the continuous-pulsatile trials and thus justify the degree to which signal noise contributes to final value pressure targeting.

3.5 *Ex-Vivo* Perfusion Transplant Specific Use-Case

Building on the performance analysis and observations of differing pump control modalities made with respect to the *in-situ* case of perfusion, we can further investigate system operation when applied to the transplant setting. As opposed to the *in-situ* perfusion setting where all major vessels remain connected to their respective peripheral systems and blood flow is modelled in an analogous sense to cardiopulmonary bypass, we now endeavour to apply system operation in the context of perfusion of the heart outside of the body. Achieving this model relies on replication of blood flow paths according to the new environment of the heart. Previously, where the **AP model** simulated blood flow into the aorta from an inserted cannula and accounted for its path through the normal peripheral circulatory system inclusive of the cardiovascular arteriole networks - the ligation of major vessels and cross clamping of the Aortic Root in the case of transplant results in a different blood flow path to be considered for perfusion.

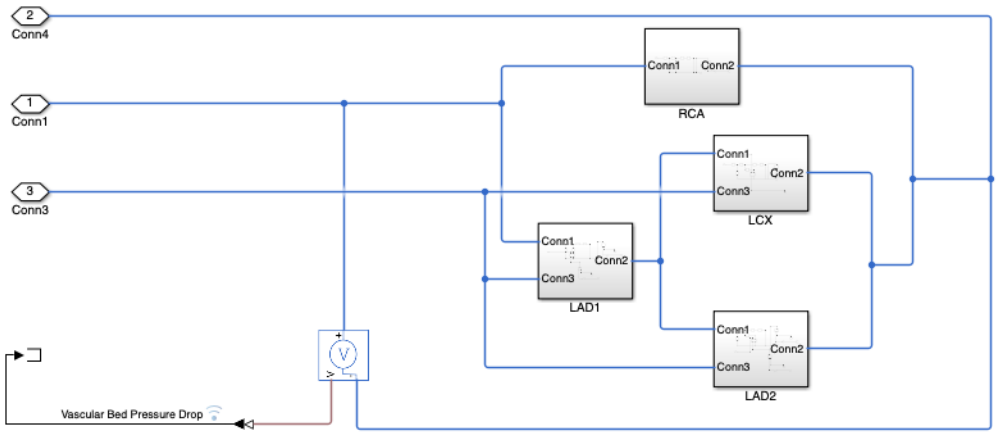

FIGURE 3.12: Application of Coronary Branch Specific Resistances

In the case of *ex-vivo* perfusion, all blood entering the aortic root as a closed compartment enforced by the cross-clamping and shut AV valve superiorly and inferiorly respectively, is now forced to solely travel through the coronary arteries to diffuse oxygen across the coronary vascular beds and finally drain into the coronary sinus. This blood flow path must now consider the downstream pressure variability of the epicardium and the resultant upstream impact on accumulated aortic pressure. As previously discussed in *Chapter 2.4.3*, pressure changes in the coronary vascular beds are chiefly affected by the local contractile myocardial tissue. This remains the case in both the left and right myocardial tissue, but at different degrees of magnitude due to the differing after-load pressures that the left and right ventricles are required to contract against. *Ex-Vivo* perfusion results in zero myocardial work of the left heart and thus an empty ventricle, which vastly reduces pre and after-load pressures. Ongoing contractility however does still result in pressure fluctuations within the microvascalature.

In order to account for these factors, we have implemented the model presented by (Kim et al., 2010), which resolves flow at each respective coronary outlet as a function of cardiac cycle dependant pressure fluctuations. This has been incorporated using the subsystem shown in *Figure 3.12* within block **R3**, previously used to simulate various systemic resistances within model simulation. This block now applies time varying complex impedance to model the pressure gradient fluctuations in each respective coronary branch. We are now able to compute an approximate estimate of flow within each of the coronary arteries by applying the *Kirchoff's Law* applied to current split. Each of the values for subsystem circuit elements can be found in *Appendix B.1*.

Due to the effect of intra-myocardial pressure on pressure gradient within the coronary vasculature and the established variable impact this can have depending on which side of the heart is considered - we apply an element of complex flow impedance to the branches of the left and right coronary artery blocks within subsystem **R3**. Due to the open nature of the new cardiovascular system as a result of explantation and before initiation of perfusion, we set the initial condition defining initial intra-aortic pressure (**X10**) to zero in order to simulate a complete loss of pressure. In reality, this pressure loss can be controlled through the integration of inlet flow to augment aortic pressure and maintain ideal root pressure during the ligation of the pulmonary veins and the cross clamping of the root during explantation. By simulating flow from an initial aortic pressure of zero we are also able to better determine the pumps capability to maximally restore required aortic pressure in the event of an unknown or spontaneous large degree of pressure loss. This aids in fully defining the operating characteristic of required pump function inclusive of both normal and unexpected clinical operating circumstances.

In contrast to the coronary vascular bed model originally recruited by (Kim et al., 2010) where normal cardiovascular haemodynamics were present, we adjust the model setup for use in a perfusion use-case by removing the effect of right intra-myocardial pressure on coronary vascular flow. In the case of perfusion during transplant where there is an absence of a connection with the pulmonary circulation - blood leaving the right ventricle does so via tubing

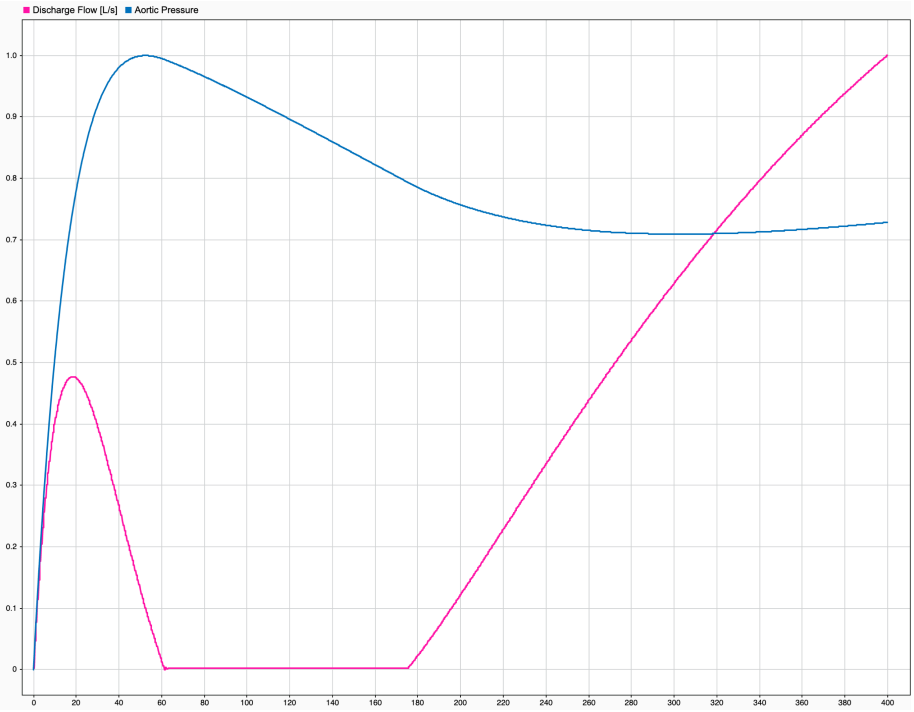

FIGURE 3.13: Effect of Vascular Bed Impedence on Accumulation and Dissipation of Aortic Pressure

connected to a reservoir open to atmosphere. In this case right ventricular afterload pressure is greatly diminished during perfusion. This is consistent with the experimental setup detailed in *Chapter 2.4.3* where in the effect of intra-myocardial pressure in the right side is considered negligible due to the lack of after-load pressure present within the ventricle.

Left intra-myocardial pressure is determined based on the findings presented according to *Figure 2.11* within *Chapter 2.4.3*. During perfusion, the left ventricle remains empty due to the back pressure present within the aortic root against the aortic valve forcing it to remain shut. To account for the empty left ventricle, we set the initial condition for simulation of left ventricular volume (**X120**) equal to zero. Intra-myocardial pressure is thus determined by using the value of left ventricular pressure from the **PPM** element provided as an argument to each block modelling respective artery impedance.

3.5.1 Analysis of Flow

Considering aforementioned characteristics of the transplant specific perfusion model, we can now better observe the consequence of pulsatile versus continuous pump flow in relation to steady state convergence of a targeted Aortic root pressure.

The continuous and pulsatile pumpflow signals and the associated developed aortic pressure can be seen in *Figure 3.8*, and made evident by the observable change of aortic pressure in the absence of any input flow from the pump. It should be noted that gradient on either side of the peak aortic pressure is unequal, indicating that the rate in which pressure is dissipated from the aortic root is significantly less that that at which pressure is initially accumulated. This is attributed to the presence of the vascular bed model which impedes instantaneous changes in pressure and flow within the surrounding coronary vasculature. Furthermore, because the initial conditions for left ventricular volume is initialised to be zero, there is no blood being ejected through the aortic valve that can contribute to an initially present aortic pressure. Therefore, the rapid rate at which aortic pressure is accumulated at the onset of pump discharge is attributable to the rapid filling of the Aortic Root from zero volume until the first point of overshoot observed in the aortic pressure signal in response to initial inflow.

The observed difference between the gradient of rising and decreasing Aortic Pressure contrasts this heart model from the **AP model** previously discussed in *Section 3.2*. Additionally, reduced rate of Aortic Pressure dissipation within the vascular bed block implies a reduced natural frequency (ω_n) from that of the **AP model**. This reduced natural frequency serves to inform future control system tuning, particular when considering improvement of response time and maximum rate at dynamic feedback control. Both filters responsible for the respective flow profiles remain the same as in trials conducted on the **AP model** (i.e Coefficients of z remain [1; 0.5]), in cases of pulsatile and continuous flow filtering respectively.

Drawing on the resulting data from *Table 3.1*, we are able to differentiate the more efficient flow profile with respect to coronary perfusion in relation to target residual data relative to the **60 mmHg** target pressure. From this

perspective and without any additional system tuning, the continuous flow profile results in a final pressure residual of **1.13 mmHg** contrasting against the pulsatile result of **9.79 mmHg**. In context of the targeted pressure, this results in a **14.43%** deviation within the **400 second** trial time. In spite of pulsatile flow achieving a shorter-settling time of **193.3497** in comparison with **196.303**, in the case of this trial these values are taken with respect to **2%** of the final value and not of the target pressure. Therefore, we expect pulsatile flow to continue to converge toward the target pressure.

Similarly, **MeanEVR** measurements are in favour of continuous flow when comparing results of **1.402** with **1.3962** respectively. This indicates that flow to the coronary bed occurs with greater efficacy when delivered using continuous pumpflow in the case of this model simulation. This result comes purely from an analytical perspective based on the definition of the $MeanEVR$ measurement as calculated in line with the logic of *Algorithm 1*.

Parameter	Continuous	Pulsatile
Variation (Flow_Type)	FALSE	TRUE
Mean CPP	61.1281	69.7860
Mean EVR	1.402	1.3962
Rise Time	15.7306	15.6209
Transient Time	196.297	193.3496
Settling Time	196.3003	193.3497
Settling Min	50.9139	62.2668
Settling Max	72.3588	76.5860
Overshoot	20.8922	10.7154
Undershoot	0.0184	0.0159
Peak	72.3588	76.5860
Peak Time	37.0096	35.2496
Sim Time	400	400
Heart Rate	100	100
Gain	0.012	0.012
Target	60	60
Target Residual	1.13	9.79

TABLE 3.2: Summary of Vascular Bed System Trials

Pulsatile flow results in a greater range of flow magnitude which is less suitable for transplant perfusion when considering the lower rate of blood drainage from the root through the coronaries. Pulsatile flow can be seen to result in a lower degree of efficacy when targeting a final pressure value, because of the time taken to drain larger pulses of blood in comparison to a single continuous stream of lower flow. In this way, continuous flow results in a more reactive system model allowing the control element to better vary input flow with a higher frequency. This improves the system's ability to converge toward a targeted root pressure within the simulation time domain. By extension, this higher inflow frequency associated with continuous flow equips the system to better account for changing pressure requirements in the presence of randomly occurring disturbances encountered by the heart during perfusion and transport.

3.6 Summary of Investigation and Key Findings

a) PID control in conjunction with dynamic negative feedback control theory has been implemented and implementation verified through the analysis of system response in relation to varying systemic resistances from the perspective of continuous and pulsatile flow variations.

b) The degree of pulsatility for a given flow profile can be varied based on the value parameterising the coefficient of z within the following transfer function $\frac{1}{1+z^{-1}}$ when applied as a filter block to the model input flow signal.

c) Continuous flow has been shown to converge toward a steady state with greater efficiency, corresponding to a lesser settling time when compared with the results of pulsatile flow.

d) Continuous flow results in lower residual values when comparing final pressure values with the targeted value of the control system over the same elapsed time period.

e) Continuous flow can be seen as a more robust input flow modality for a system that may have variable degrees of disturbance that cannot be accounted for.

Chapter 4

Computational Hemodynamic Method

In order to determine and consider the impact of different device design considerations, blood flow through the Aortic Root from via an inlet cannula and through the major coronary arteries can be simulated using computational fluid dynamic calculation methods.

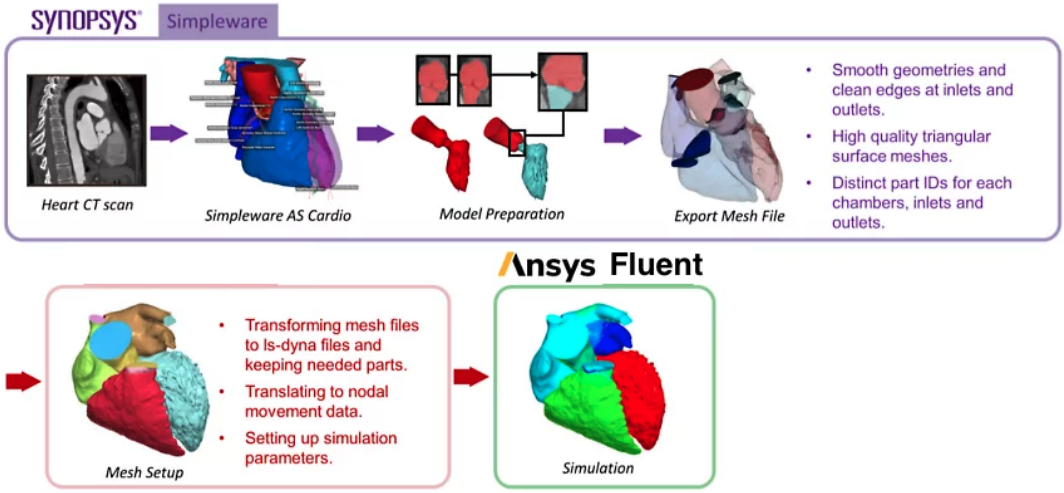

FIGURE 4.1: Mesh Development Workflow (Michael Rochette, 2024)

Segmentation techniques applied to the region of interest within CTA-data was achieved using *Synopsis Simpleware* for the extraction of the Aortic Root geometry. The segmented geometry was then augmented to include a cannula geometry in addition to a representation of root cross-clamping consistent with surgical transplant procedure.

Model mesh independence can be verified through the comparison of different iterations of the segmented model mesh through comparison of total mesh size with solution values of velocity at the boundary conditions. This was achieved using *Ansys Discovery* and *Ansys Fluent*. Development of a mesh model associated with a size yielding solution values deemed independent of the mesh, was then converted to a polyhedric mesh to achieve improved computational efficiency for use in longer simulations. Creation of a *Matlab* script allowed for pump discharge signal values from the *Simscape* perfusion model to be written to an *Ansys Fluent* flow profile. This flow profile was then applied to the polyhedric mesh in a transient flow simulation and subsequent data values of **Pressure, Pressure Gradient, Velocity** and **Wall Shear Stress** were then computed.

4.1 Computational Model Mesh Development

The utility of a CHD model describing the perfusion use-case allows for the transient approximation of pressure-velocity coupling as function of inflow with respect to anatomically sound geometry. Blood was modelled as an incompressible, isotropic homogenous fluid of constant viscosity and density. Thus, blood was assumed to be Newtonian with measures of **0.0037 Pas** and **1060 kg/m^3** for viscosity and density respectively. Walls were modelled as solid and stiff while zero-velocity boundary conditions were assumed corresponding to a no-slip condition at the vessel walls.

4.1.1 Computer Tomography Image Segmentation

To achieve a three-dimensional model that details the necessary geometry of the aortic root and it's interconnected vessels, the best practice is considered to be the creation of a mesh object from the segmentation of a patient specific

computed tomography of the thoracic cavity. Using the CT dataset previously recruited in a peer reviewed study by (Zeng et al., 2023), and the application of *Simpleware* software, a segmentation was carried out in which all major regions and vessels of a patient's heart were segregated and individually saved under appropriate masking labels. All image acquisition data other than that pertaining to the Aortic Root and its tributaries was removed from segmented region of interest. A combined geometry was achieved through combination of these masks using the application of a combinatorial boolean operation.

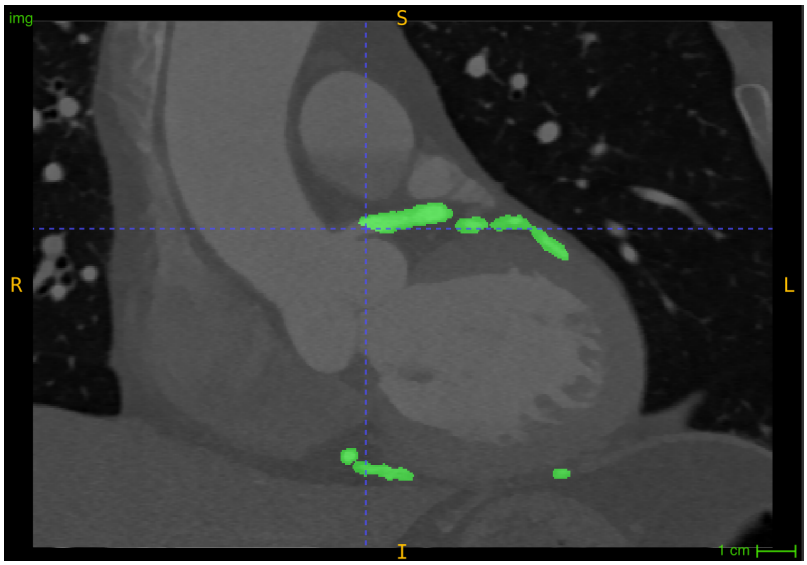

FIGURE 4.2: Coronal Slice of Chest CT Image with Coronary Label Overlay

A recursive Gaussian smoothing filter was then used to remove any artefacts and noise anomalies present in the segmentation. Using a centreline generation algorithm, the median distance of each vessel from the vessel wall was calculated and is shown in a model geometry render *Figure 4.3*.

4.1.2 Aortic Root Surface Meshing

In order to generate a 3-D geometry of the segmented shape we require to first generate a surface mesh based on the extracted segmentation from our region of interest within the CT-image shown in *Figure 4.2*, showing the targeted coronary segments highlighted in green. This process was conducted using *Simpleware* software to extract the Aorta and Right + Left Coronary Arteries as separate shapes. A boolean operation was then conducted in order to merge these three masks into one continuous surface shape.

A gaussian smoothing filter was then applied to the segmented data associated with the combined mask in order to reduce inevitable noise and create continuous surfaces. Any additional and unnecessary artefacts were then removed using a three dimensional frustrum selection.

Finally, a centreline generation algorithm was used in order to track the median paths from the bifurcating vessels into the Aorta. Each of the centrelines represent the mean blood flow direction field at the instantaneous axis of the respective vessel. Using the centrelines, the artery boundary conditions were created by specifying cut-off planes oriented normal to the centreline at a user specified length proximal to the aortic centreline. The associated centre line lengths are shown in *Appendix B.4*.

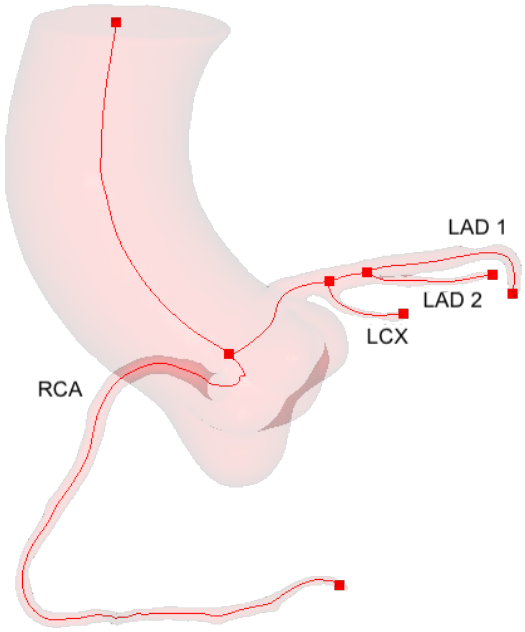

FIGURE 4.3: 3-Dimensional Centreline Render of Aortic Root CT Segmentation

4.1.3 Volumetric Mesh Rendering and Clinal Geometry Augmentation

In order to represent the perfusion use case in the most practically accurate sense consistent with the clinical setting for transplant perfusion we must address both the modality of inlet flow delivery in conjunction with the tendency of blood in the aortic root to continue in an antegrade direction unless otherwise restricted. Thus, we introduce the implementation of the cannula and the replication of a superiorly cross clamped geometry respectively.

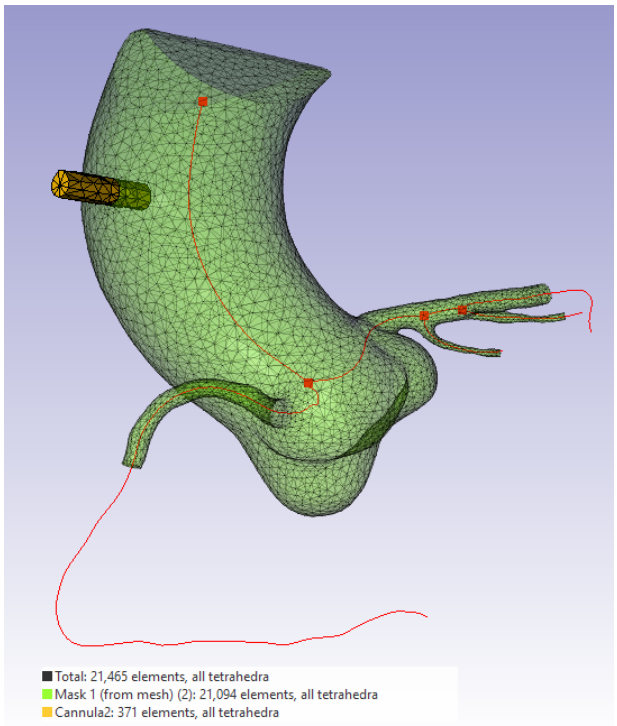

FIGURE 4.4: Combined CAD and CFD Model Meshing

4.1.4 Boundary Conditions

It should be noted that in *Figure 4.4*, there is a clear distinction that can be seen in the segmentation from the left ventricle blood domain and associated cusps of the **AV** forming the Z_{Min} boundary condition of the root model. This

is a boundary geometry rarely established in existing studies and surrounding research, but is crucial in the case of this investigation where in the accumulated perfusion pressure within the root against flow direction on the cusps of the aortic valve cause a closed compartment and can thus be modelled as a boundary wall in latter processes. Additionally, as with the case of aortic perfusion in the case of transplant as presented in *Chapter 1*, there exists a cross clamping along the root of the aorta marginally superior to the cannulation site. This closes the fluid domain superiorly and thus defines the Z_{Max} boundary condition also taken as a wall.

Table 4.1 Boundary Condition Definitions

The following boundary conditions and their definition at each boundary are as follows:		
Boundary	**Definition**	**Quantity**
Aortic Root Cannula **(AoRC)**	Velocity Flow Inlet	Velocity Flow rate
Right Coronary Artery **(RCA)** Circumflex Artery **(LCX)** Branch 1 of Anterior Interventricular Artery **(LAD1)** Branch 2 of Anterior Interventricular Artery **(LAD2)**	Pressure Outlet	Volumetric Flow Rate
Cross Clamp Zone	Z_{Max} Boundary	Wall
Shut Aortic Valve	Z_{Min} Boundary	Wall

4.1.5 Physics Setup

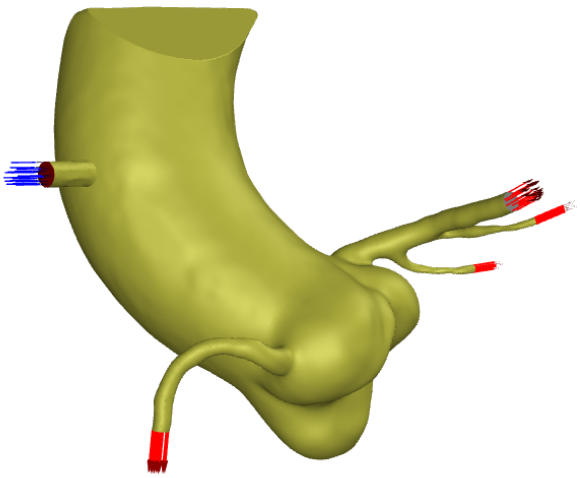

FIGURE 4.5: Mesh Boundary Condition Render

The setup of the physical conditions under which the model is simulated begins by specifying the most appropriate solving model for our case. This case will be calculated using a *Transient-State Laminar Viscous* model. This subsequently models the system based on the premise that there can only be laminar flow of blood and that fluid is considered to have viscous properties and thus behaves as such. The requirement for the analysis of haemodynamic parameters dependent on the changing inflow profile with respect to time defines the nature of this transient system.

4.1.6 Solution Setup and Initialisation

Simulation flow trial time was taken as a control variable and fixed at a total of **0.5** seconds achieved using **500** timesteps of **0.001** seconds per time step. This step size was chosen in order maintain a Courant number of approximately $\leq$ **200** at an inlet velocity of **80** cm/s. In all cases the **Viscous-Laminar** model for incompressible fluid flow was employed and the **SIMPLE** fluent solver algorithm was used as the method for pressure-velocity coupling. Furthermore, each iteration's solution data was compared using the same respective sample time at **0.5** seconds. This time point was chosen with the aim of comparing solutions based on maximally developed flow profiles within the mesh. Due to the use of a constant inlet velocity, we expect the solution at the final time step to be inherently more accurate than the solution data at prior time-steps.

4.2 Model Verification

In order to verify that the aortic mesh model performance was independent of the mesh used in the calculation, variance of the computational output data associated with five distinct mesh models of differing respective total element size were investigated.

4.2.1 Mesh Independence Study

Each mesh represents an iterative increase in the total number of mesh elements and thus an increase in computational complexity. As computational complexity increases, the accuracy of the solution is expected to converge toward the theoretical ground truth which would in theory be achieved using a model with an infinite number of mesh elements. In order to ensure that the results of simulation are as accurate as possible without resorting to an unnecessary level of computational expenditure, we proceed by determining the approximately ideal number of mesh elements required in the model such that the resulting solution residual between the ideal mesh and subsequent iterations falls within an acceptable and pre-defined margin of error. This established margin of error represents the minimum required degree of solution independence for consecutive iterations and represents a stopping criteria in the determination of the optimal mesh yielding a solution having a statistically significant degree of impact on the overall fluid model validity.

To analyse the point at which iterative solutions converge with respect to an increasing number of grid elements, we need to determine the window of possible solution meshes that we may use to measure the varying output against. Using a total of five distinct mesh models of varying size, we determine what the computational constraints are that determine the maximum and minimum number of elements that can be used. Once the range of total elements is determined we may then aim to divide this total number of elements across the five mesh iterations in order to select mesh sizes incrementing on an approximately linear basis.

Iteration	**Mesh Grading**			**Total Surface Elements**
Mesh #	**Target Edge Length**	**Max. Error**	**Meshed Edge Length**	**Tetrahedra**
1	0.55	0.001	0.57998	8392215
2	0.49	0.001	0.55000	10066193
3	0.47	0.001	0.54609	10353244
4	0.45	0.001	0.54240	10701479
5	0.43	0.001	0.53882	11065418
6	0.41	0.001	0.53200	11581981
7	0.39	0.001	0.52600	12111505
Mean	0.455714286	0.001	0.545041429	10610053.57
Variance	0.002481633	0	0.000260676	1.24172E+12
Std. Dev.	0.049815988	0	0.01614545	1114324.527

TABLE 4.2: Mesh Properties

Constraints determining the upper bound of possible elements is the capacity of the mesh solver to produce a the measure with chosen input parameters (In this case, a minimum and maximum target edge length was used). Additionally, as total mesh elements increases, so does the subsequent computational time required to reach a solution. Practically speaking, the upper bound constraints come down to the total number of computer cores that can be accessed for use. These trials were conducted using a computer with a total of 12 cores available for multiprocessing.

The lower bounded mesh is determined by the finest mesh that still results in numerical instabilities or floating-point exceptions. In other words, this mesh results in a solution divergence across the maximum number of allowable solver iterations conducted per time step with respect to the minimum specified margin of error. This divergence is an indication that with each solution iteration the resultant measurements are decreasing in accuracy. The margin of error in this case is approximately 10^{-3}.

Mesh	**Area Average Velocity [cm/s]**	**Area Velocity Integral [cm^3/s]**			
Iteration #	**Inlet**	**LAD1**	**LAD2**	**LCX**	**RCA**
3	80	9.96630	0.238233	0.27445	5.29336
4	80	9.52049	0.384118	0.397632	5.53007
5	80	9.50174	0.397173	0.39390	5.54397
6	80	9.50451	0.396790	0.389901	5.54551
7	80	9.49210	0.397427	0.392414	5.55280
Mean	80	9.60	0.36	0.37	5.49
Variance	0	0.042717286	0.004876808	0.00284089	0.012540374

Mesh	**Area Average Velocity [cm/s]**	**Area Velocity Integral** [cm^3/s]			
Iteration #	**Inlet**	**LAD1**	**LAD2**	**LCX**	**RCA**
Std. Dev.	0	0.170869144	0.019507234	0.011363561	0.050161495

TABLE 4.3: Mesh Solution Measurements

Taking both the upper and lower bound into consideration, we establish target edge length input parameters for the meshing process of **0.7 mm** and **0.3 mm** respectively. Linearly decreasing the edge-length with each mesh resulted in the five mesh iterations with associated characteristics as seen in *Table 4.2*.

4.2.2 Optimal Mesh Size Determination and Refinement

Once the mesh independent model has been determined, converting the domain of the mesh geometry from a tetrahedral to a polyhedral standard becomes an advantageous consideration. This allows for maximally improved computational efficiency allowing for the generation of solution data over a larger total simulation flow-time. The time interval chosen can now be representative of the perfusion specific use-case in the context of the system design discussed in *Chapter 3*.

Interpolation to Determine Optimal Mesh Size

Taking note of the resultant meshing solutions illustrated in *Figure 4.6 & 4.7* with respect to a **5%** specification limit shown above and below the respective signals, we may derive an optimal mesh size. The **5%** limit in both cases is drawn with respect to the final data point associated with the finest mesh. This is value is theoretically the most accurate data point in relation to the absolute truth of the computation. Therefore, we seek to determine a mesh size that will produces results within a **5%** given margin of error in relation to our most accurate data point.

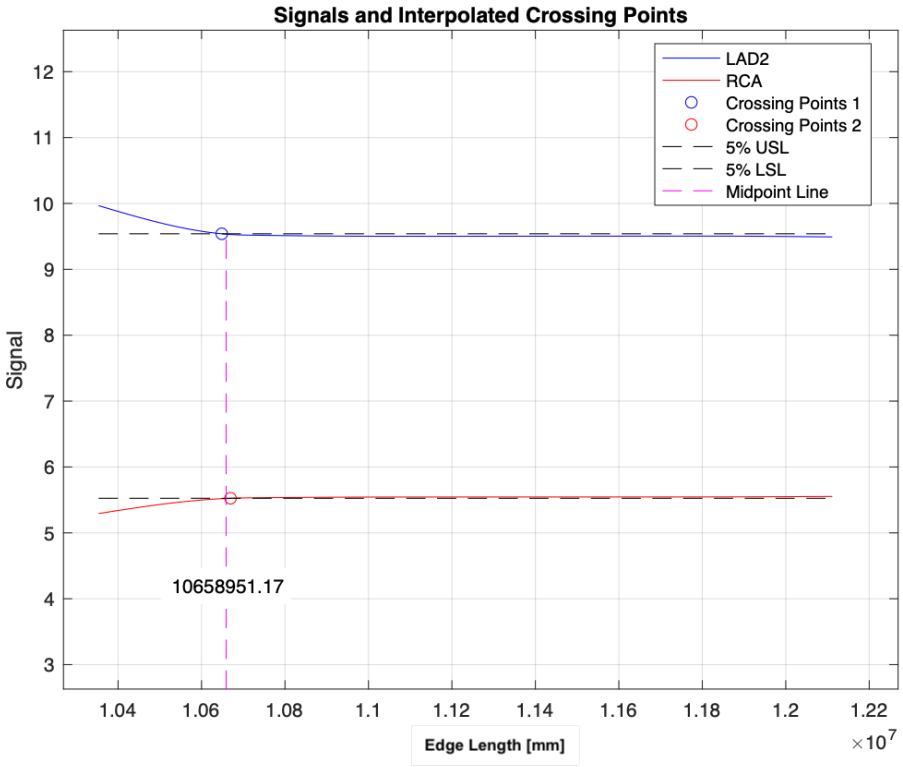

FIGURE 4.6: Midpoint Intersection of Interpolated Crossing Points with X-Domain

By interpolating the respective signals around the point in which they intersect the specification limit we may deduce the x-value of the intersection. Furthermore, by taking the midpoint of both intersections and tracing a guideline perpendicular to the x-axis we are effectively determining the average value in which in each measurement diverges out of the **5%** specification zone. This method yields two total mesh size values of approximately **10 658 951** and **10 720 331**.

Using *Equation 4.1* we determine the midpoint of these two values rounded up to the nearest integer.

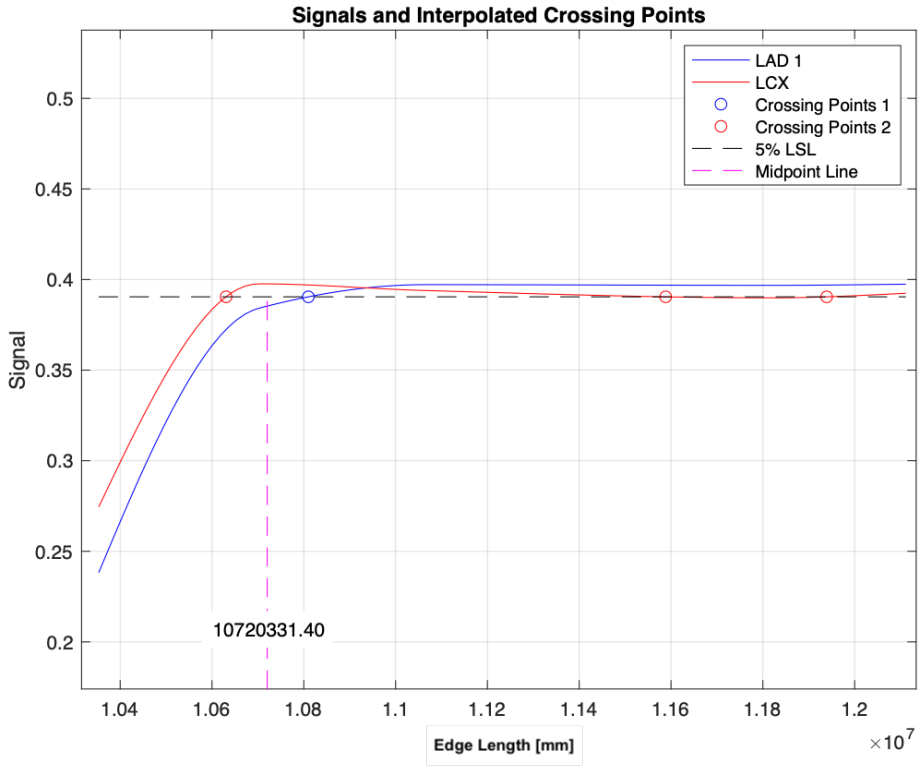

FIGURE 4.7: Midpoint Intersection of Interpolated Crossing Points with X-Domain

$$x_{\text{mid}} = \lceil m \rceil = \left\lceil \frac{x_1 + x_2}{2} \right\rceil \tag{4.1}$$

The resultant optimal mesh grid size that serves to produce solutions within a 5% margin of error of the most accurate solution has been determined to use a total of **10689641** tetrahedra.

The resulting mesh would thus be produce solutions that would be considered to be independent of it's total mesh element size and be the greatest degree of accuracy in relation to the computational cost required to produce the solution.

Using the established relationship between mesh size and edge length the calculation required to determine the associated meshing parameter follows:

Using the linear relationship interpolated from *Table 4.2*:

$$y = -9 \times 10^7 x + 6 \times 10^7 \tag{4.2}$$

where:

$\mathbf{x} =$ is the targeted edge length in millimeters.

$\mathbf{y} =$ is the resultant total number of model meshed elements.

Using the determined linear **Size-Edge Length** relationship, *Equation 4.2* yields the optimal element edge length as approximately **0.54789** *mm*.

Optimal Solution

Using optimal meshing parameters determined from the grid independence study and replacing the use of tetrahedral mesh elements with that of polyhedral the resulting configured a mesh of consists of **6 986 892** faces for computation.

4.3 Generation of a Three-Dimensional Physical Flow Phantom

Building upon the generation of the aortic root perfusion model, a physical flow phantom of the model was designed and built for the purpose of validation of the flow and velocity outcomes of the perfusion specific use-case.

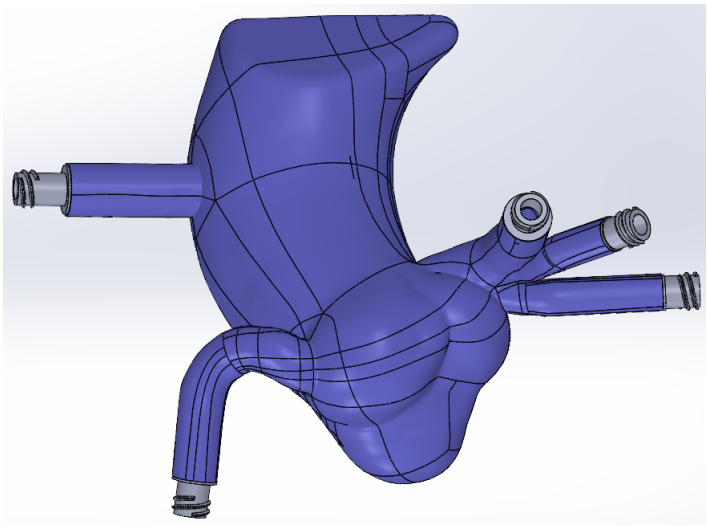

FIGURE 4.8: CAD Generated Aortic Root Model

The phantom in this study was created with the use of a *FormLabs 2* 3D resin printer to generate a hollow structure specified by a *Solidworks* mechanical part design. For the purpose of phantom implementation into a potential testing rig created for flow validation which will be further discussed in the following chapter, a positive phantom model was designed and fabricated. **The methodology for fabrication is detailed as follows:**

1. **Tetrahedral Facet Manipulation**
   This entails utilising various **normalisation, reduction** and **Gaussian smoothing** algorithms in order to create a geometry of adequate element and surface consistency, particularly in regions of bifurcating structures such as the distention of Right Major Coronary artery from the aortic root. These regions contain a higher degree of geometrical complexity and in order to preserve the detail inherent in the mesh, it necessitates a greater number of surface elements of smaller edge length in order to create planar surfaces with a sufficient degree of freedom that fully define the structure without contributing to a loss of geometric information. An example of the augmentation to surface element density is illustrated in *Figure 4.9*

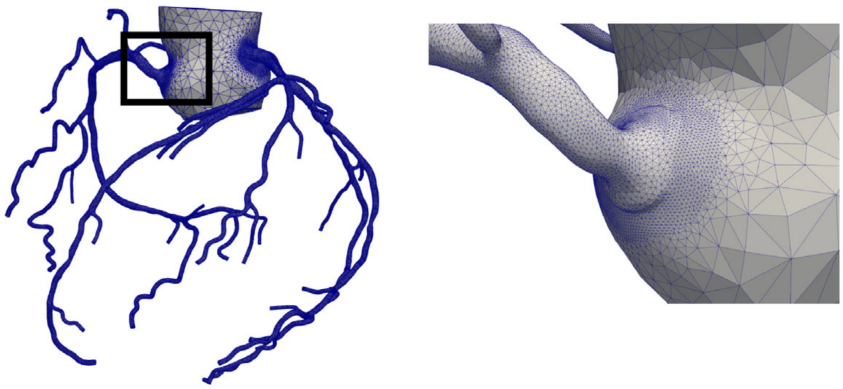

FIGURE 4.9: Surface Element Density Refinement of RCA Root (Taylor et al., 2023)

2. **Contribution to Wall Thickness**
   To create a model part that has structural integrity sufficient for flow testing while preserving the true shape of the interior fluid domain, a mesh shell was created by extruding the outer surface of the tetrahedral surface mesh by a chosen wall thickness. In this case, **3 mm** represented an adequate degree of thickening that would provide adequate structural integrity to the wall without compromising the true shape of the structure. In this way the total fluid domain has been preserved and is consistent with the geometry of the model intended for validation.

3. **Solid Surface Patch Segmentation**
   In order to convert a collection of tetrahedral surface elements into a continuous solid volumetric shape, the total geometry was segmented into distinct regions of geometrical interest. The resulting smoothed and continuous surface plane is called a patch and is a geometrical aggregation of all of the tetrahedral surface elements contained within the patch boundaries.

4. **Boolean Patch Recombination**
   A combination of patches joined at congruent edges creates a surface. A combination of surfaces to form an enclosed region creating a solid volumetric shape which can be converted into a mechanical part file. Once all regions are patched, the implementation of geometrical boolean algorithms were used in order to determine common sub-regions of the patches that are considered coincident. The resulting collection of new boundary lines among overlapping surface sub-regions are used to combine adjacent patches into common surfaces through the use of a joining algorithm. Once the entire inner surface wall and outer surface wall of the mesh model have been combined, patch lines can be adjusted until a solid closed shape enclosing the entire continuous fluid domain can be solved using meshing software to preserve a geometrically hollow cavity.

5. **Augmentation of Inlet/Outlet Features**
   In order to integrate the part into a flow testing apparatus, there must be a means in which flow can be directed into the cannula and received from the outlet of the coronary vessels into the surrounding circuit. Tubing typically used has a double-start thread in order to be firmly secured with other components typically found in a perfusion circuit. The associated thread profile was measured and recreated in *Solidworks* and fabricated in **PLA** using 3D printing technology. The seal was tested by running fluid through the connection at high pressure and ensuring no leakage. The verified thread design was then merged to the solid mesh model part at the inlets and outlets. Each threaded part was then individually adjusted in dimension to ensure that its connecting base surface plane was consistent with the vessel wall when merged. The result produced a mechanical part model of the aortic root with specific inlet and outlet geometrical features that allow for a seamless integration into a perfusion circuit using standardised perfusion tubing and fixation supports.

6. **Printing and Fabrication**
   The resultant part geometry was then converted into a **.3mf** file type in order to be configured within the 3D printing software for use with the *FormLabs 2* printer. A resolution of **25** μm was used in order to maximise interior and exterior surface detail. The model was tested for adequate connection with the aforementioned perfusion tubing at all connection areas and verifying no leakage at any of the connections by introducing a continuous fluid flow at the cannula inlet region. The resulting physical model generated allows for flow model verification by emulating the patient specific geometry of the interior fluid domain of the Aortic Root.

4.4 Summary of Investigation and Key Findings

(a) The use of CTA image segmentation techniques allowed for the development of a three-dimensional mesh model incorporating perfusion specific root cannulation and cross-clamping.

(b) The procedure of carrying out a mesh independence study resulted in the optimal mesh size of **6 986 892** achieved using the proposed *Equation 4.2* for size-edge length determination specific to the model geometry.

(c) Further development of the geometry resulted in the fabrication of a physical resin based anatomically accurate aortic root phantom that can be implemented into a hydraulic circuit through the use of fitted mechanically modelled outlets consistent with universally recognised tube threading.

Chapter 5

Bench Test Design, Assembly and Calibration

In this chapter the proposed bench test model solution is designed, assembled and configured according to observations made based on *Simscape* perfusion simulations that govern optimal circuit configuration when tested in conjunction with model circuit elements that enable the representation of fluid flow through a hydraulic isothermal liquid network in conjunction with a physical fluid circuit.

5.1 Bench Testing Rationale

In order to confirm observations made from the simulation trialing presented in *Chapter 3*, and to justify potential future design considerations for a fully integrated system model, there requires to be an investigation into the error and degree of reliability of physical fluid variable output measurements of the simulation model. This allows us to verify the relationship between the applied motor signal, the developed torque in the driving/driven shafts and the resulting hydraulic signal profiles through the theorised circuit. Furthermore, by investigating and determining the magnitude of variability between a physical flow circuit and the simulation outputs, we may derive necessary scaling and correction factors that can be applied to correct for any losses not modelled and therefore not accounted for. This results in the generation of a model that is now specific to a physical circuit configuration and the properties of the fluid used within it.

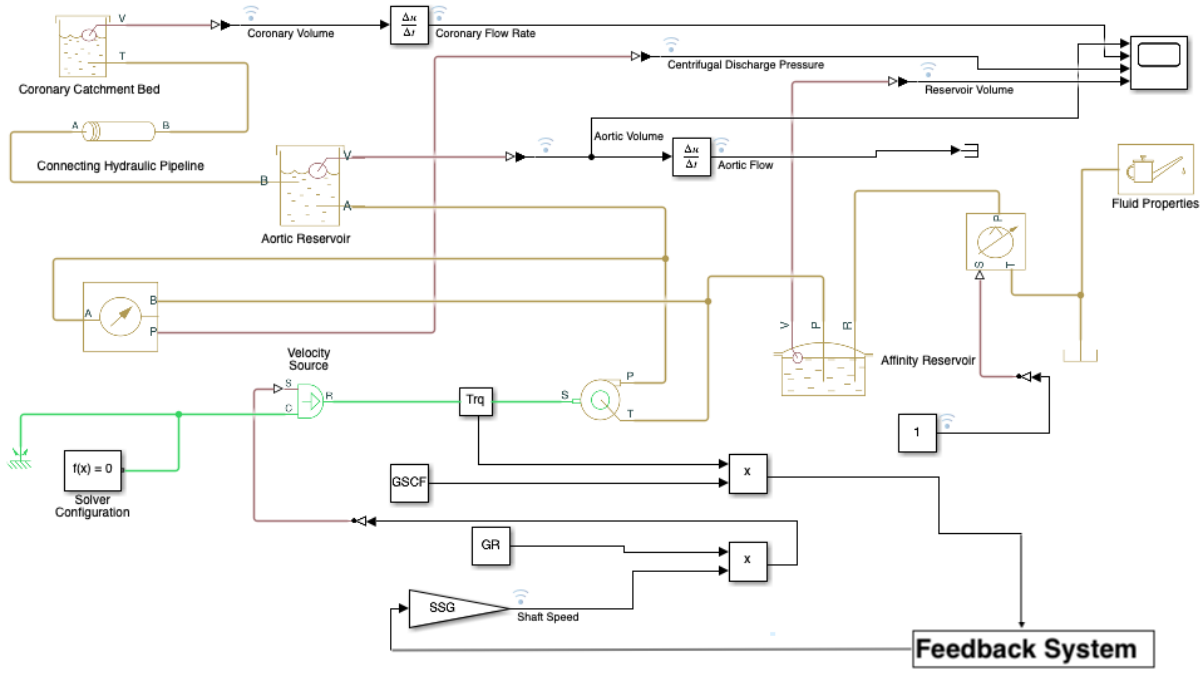

FIGURE 5.1: Simulation Flow Circuit Configuration

Inevitably, there will be variation between measured simulation and physical flow outputs because the simulation model does not completely account for all vessel dimensions, mechanical friction, power losses and circuit specific components of unknown impedance. The model does however, allow for the establishment of

working relationships between relevant input and output signals that govern flow. This relationship can thus be validated using a physical circuit by applying the input motor signal from the simulation into a physical motor pump assembly. The difference of resultant flow measurements with respect to flow time can then be quantified and compared to the simulation trial results using the same input over an equal length of time. Such a comparison can effectively be achieved using the developed flow rate and volume values from one reservoir tank to another. By carrying out this bench testing protocol we are able to validate the implementation of pump control with respect to the theoretical requirements for pressure and flow variation in response to the simulated dynamic requirements of the *Simscape* heart model.

By scaling the simulation model to accurately represent actual physical flow behaviour, we may better quantify the developed pressure in the aortic root in relation to actual pump flow discharge. By extension, the PID feedback loop may then be tuned to handle realistic flow volumes with greater accuracy and efficacy and contribute towards better future design iterations. The main aim of the methodology within this chapter serves to report and outline the procedure followed during the determination of scaling and correction factors that were used to validate the simulation perfusion model.

5.2 Hydraulic System Configuration

Using physical circuit components, our aim is to create an assembly representative of the hydraulic subsystem modelled in *Figure 5.1* and the physical fluid flow network diagram shown in *Figure 5.3*. Considering the feasibility of assembling a fully operational system, circuit design must be simplified to facilitate the measurement of parameters that are exclusively necessary for the aforementioned model validation purposes.

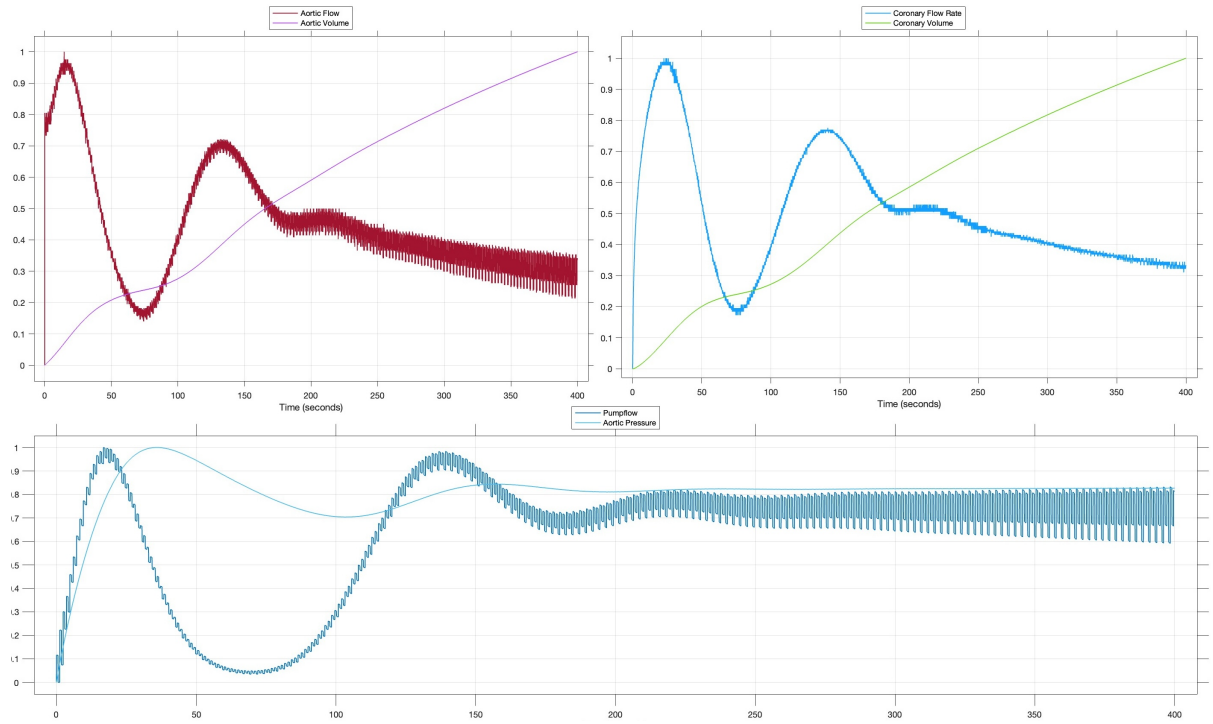

FIGURE 5.2: Normalized Coronary and Aortic Flow Simulated Output Signals

The hydraulic aspect of the pump system block from *Chapter 3*, did not directly feedback into the control loop. In contrast, the model used for validation in this chapter focuses on modelling the fluid in a manor that accounts for the relevant losses attributed to the haemodynamic properties of blood as a fluid medium. Furthermore, the flow of fluid from one reservoir to another is subject to the surface pressure present. These factors may result in variable degree of pump head required to be developed by the pump. To take these factors into consideration and bring model parameter outputs within a range that can be accurately scaled using observations from the bench test analysis - the hydraulic aspect of the pump system has been modelled as an open isothermal-liquid system. This means that hydraulic signals generated by the pump components and downstream pressures do not feedback into the control loop as an error signal, but rather serve as a physical parameterisation of the control system response. Therefore, we can think of the pump system being connected to two theoretically parallel analogous systems. One system being the *Electrical Feedback Response* defines the domain in which PID response is determine, while the other system being the *Hydraulic Flow Response* was

used to measure the resultant fluid flow response in terms of physical parameters in relation to the model pump control. The two systems remain in parallel concurrent operation through the use of globally defined system-state variables used in initialisation. Initial conditions and associated set constants can be referenced in *Appendix A.1*

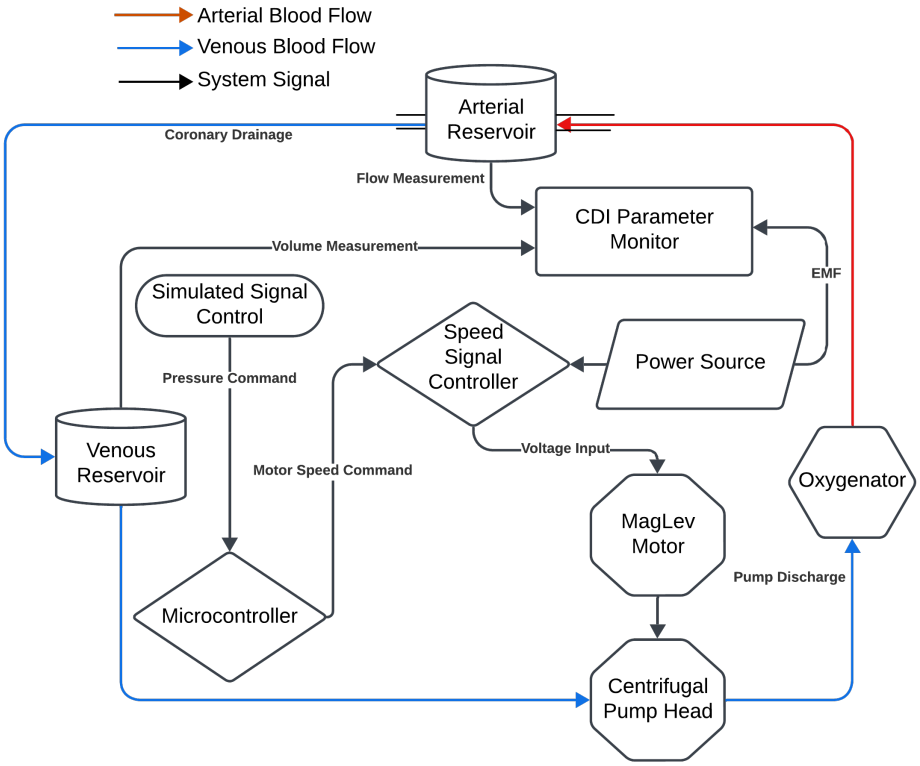

FIGURE 5.3: Physical Flow Circuit Configuration

Each of the reservoir's modelling aortic and coronary fluid levels have been initialised to maintain a constant pressurisation level of **1 atm**. This allows the hydraulic circuit to model the effect of fluid flow while open to atmosphere. Due to the hydraulic circuit being implemented in parallel to the heart model where the aortic pressure feedback requirement is calculated, the hydraulic circuit is modelled open to atmosphere so as to ensure that the effect of pressure accumulation is not being accounted for twice and that the resultant downstream coronary fluid level value is not the product of a compounded upstream pressure gradient. Despite the reservoir components not being used to derive signals fed back into the heart model, the presence of pressure within the aortic reservoir block causes a change in the resultant pressure gradient against which the centrifugal pump block is required to pump against. The signal driving pump operation has already been transmuted to a flow command based on the calculation of discharge pressure required to achieve the target root pressure. If there exists an additional flow impedance to the pump in the form of an added static/pressure gradient, the upstream required torque calculated to drive the pump with the specified discharge pressure is affected.

The use of the parallel hydraulic circuit serves purely to model and inform resultant fluid flow in relation to the pressure dynamics modelled within the simulation of aortic root pressure changes within the heart model. These measurements allow for insight and observation to be made about pump operation in response to differing control settings under which the heart model is simulated. By extension, the model can also then be better corrected to account for energy and hydraulic losses of actual physical components when run in parallel with a test rig making use of reservoirs that are open to atmosphere. Pressurisation of the actual reservoir components to the value of modelled aortic and coronary pressures within the test rig, would not only be challenging and likely an infeasible task for this study, but would also not be necessary because the main purpose of the test rig is the measurement of fluid flow of specified components. Additionally, there is no physical feedback of pressure residuals that takes place outside of the simulation, therefore there is no requirement to emulate heart model pressures within the test rig circuit because the pump response to the hypothetical aortic root is not the subject of verification within the bench testing protocol.

5.2.1 Fluid Flow Properties

In order to simulate the hydraulic behaviour of blood as a result of changing pressures within the circuit, we initialise the model to simulate flow of fluid that has properties as similar to blood as possible. We thus

consider the values established for blood and comparative fluids in *Table 5.2* according to (Kim, Prasad, and Kim, 2016).

Table 5.2 Fluid Properties

Viscosity (mPa·s)	
Component	Value
blood (37°C)	$3 \sim 4$
distilled water (20°C)	1.002
10% glycerol solution	1.310
20% glycerol solution	1.615
40% glycerol solution	3.686

Density (g/mL)	
Component	Value
plasma	1.025
lymphocyte	$1.06 \sim 1.1$
red blood cell	$1.09 \sim 1.2$
distilled water	0.998
10% glycerol solution	1.0221
20% glycerol solution	1.0425
40% glycerol solution	1.097

Taking note of the comparable properties of a 0.4 **Aqueous-Glycerol** mixture to blood, we have selected this fluid for use *In-Silico* by way of the *Simscape* hydraulic fluid properties library.

5.2.2 Flow Pattern Relationship

Testing the hydraulic system yields the signals illustrated in *Figure 5.2*. From this we are able to ascertain the relationship between accumulated pressure of the aortic root and the resultant flow developed from the root into the coronary catchment reservoir. In this figure the gradient changes of the volume measurement of each reservoir occur in phase with the variation of the respective flow rates to the same reservoir. A change from positive to negative flow rate reflects in the reduced positive gradient of fluid level accumulation in the associated volume signal. This illustrates that the rate of change of volume in the vessel is proportionately affected by the changing rate of flow. Observation of this relationship serves to verify correct configuration of the hydraulic system reservoir components in relation to the function of variable pumpflow as determined by simulation of changing aortic root pressure.

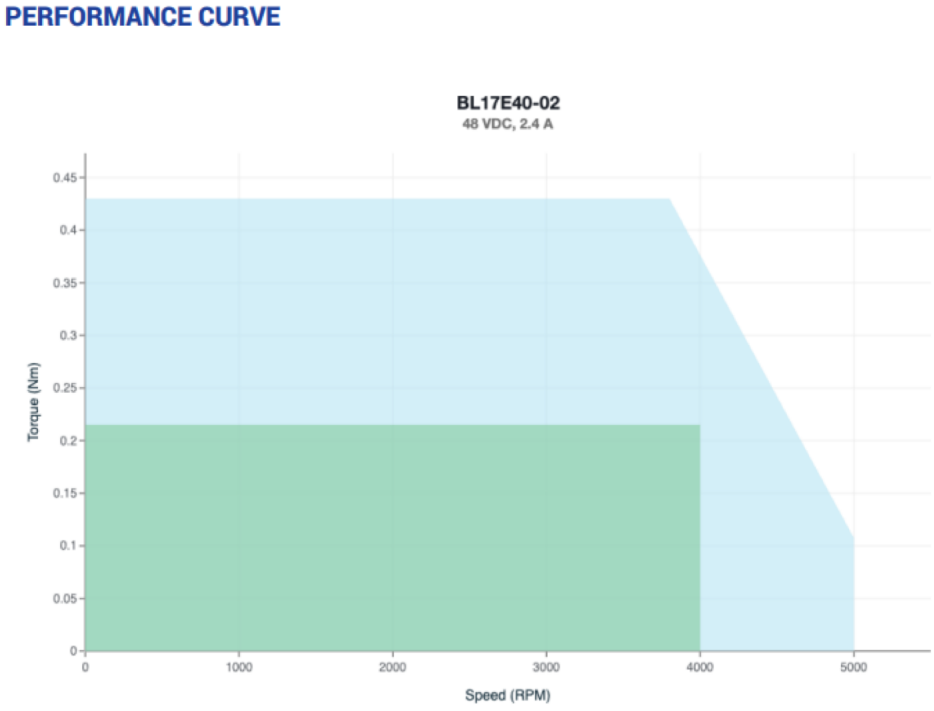

FIGURE 5.4: Motor Input Torque-Speed Duty Cycle

For the purposes of this investigation we have used a continuous pumpflow profile to determine and verify the hydraulic flow signal relationship. Furthermore, the continuous profile has a high signal to noise ratio than that of the pulsatile flow, which allows for a clearer representation of the relationship of downstream flow patterns developed between the aortic and coronary reservoirs.

5.3 Extracorporeal Circuit Configuration

The circuit can be assembled using basic components typically used in conjunction with ventricular assist and ECMO devices. This is representative of the medical grade of components standardised for use within the cardiac perfusion space.

5.3.1 Motor Design Specification

Motor

The high-level flow configuration of this system relies on a motor coupled to a shafted fixed to the gearing of a magnetic bearing head that coupled to the coned centrifugal pump head. The centrifugal pump and bearing are only coupled to the impeller on positive rotation of the shaft, which means that shaft torque only exists as a result of bearing friction and is independent of fluid inertia and relative momentum. This is advantages when needing to accurately match the speed of shaft rotation with a dynamically varying input signal. An important consideration when designing and procuring components for the test model then becomes choosing a motor with the correct dimensions and operating characteristics that allows for full utilisation of the centrifugal pump capability. We therefore, aim to choose a motor with rotational speed matching accuracy with little requirement for torque capacity. This leads us to consider the category of brushless DC motors due to the efficiency with which they can be used to match speed requirements and dynamically varied according a variety of different control modalities.

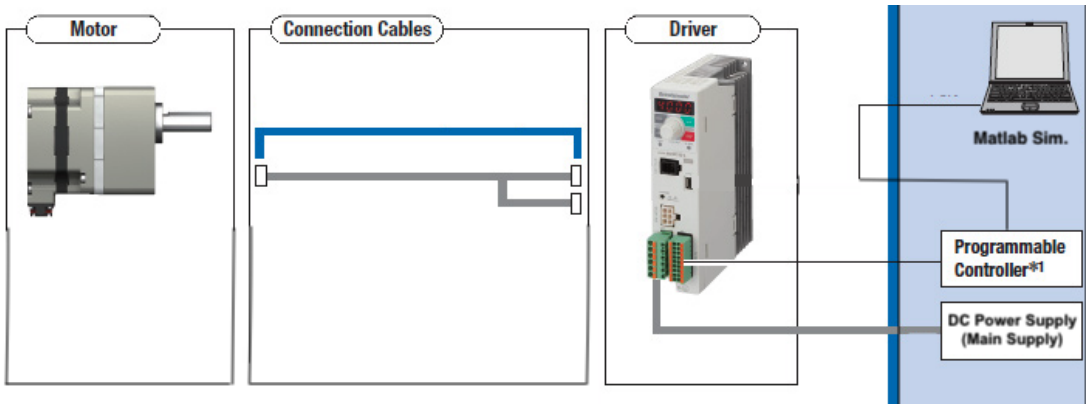

FIGURE 5.5: Bench Test Motor Control System Configuration

The magnetic bearing drive unit is designed for use between **1000-4000 rpm**. The drive unit exhibits negligible changes in torque during operation at approximately **0.1 Nm**. Furthermore, the driving head couples the shaft to the magnetic bearing by a gear ratio of approximately **1:35**.

The motor operating requirements are thus established based on the capacity to maintain **>= 0.1 Nm** of torque during operation of **<= 4000 rpm**. In practicality, considering the pump head maximum capacity for **800 mmHg** discharge pressure corresponding to approximately **3500 rpm** and applying this across the gear ratio of the driving head means that the maximum required shaft speed that a motor is needed to produce is approximately **100 rpm**.

$$\dot{\theta}_{\text{max shaft}} = \frac{\dot{\theta}_{\text{max impeller}}}{\text{GR}} \tag{5.1}$$

Where *GR* is the given gear ratio.

We now consider the performance curve in *Figure 5.4* for a **48 V DC Brushless Motor**. Taking note of the extent of the continuous-duty cycle indicated by the green rectangle, we may deduce that the associated motor is able sustain **0.2 Nm** of torque while operated at shaft speed between **0-4000 rpm**. Furthermore, the motor can achieve a maximum torque of approximately **0.425 Nm**, but proportionately diminishes at shaft speeds greater than equal to approximately **3800 rpm**. The maximum torque that can be generated at the motor's maximum rated shaft speed is thus **0.1 Nm**.

Accounting for the maximum required torque, the maximum required shaft speed and the subsequent largest possible pump discharge pressure, it is evident that the motor associated with this performance curve is more than adequately specified in terms of it's capacity to achieve the desired operation for use in the bench test

model. We have therefore chosen the **BL17E40-02** and associated driver for use in this circuit assembly. Device specific operating characteristics were gained through the associated specification data that can be found in *Appendix C.1 & C.2*.

Motor Control Specification

Speed control over the motor to a required degree of accuracy is a vital aspect of system performance because of the impact of speed control accuracy on the discharged flow rate and the requirement for changing flow as a time dependent dynamic response. Speed control over the motor was thus achieved using the **BLDC-50** control element supplied by *Lin Engineering inc.*. In order to drive the motor at the instantaneous speed resulting in the pumpflow required by the system feedback logic to duly regulate pressure, time varying speed commands must be able to be directed from the system (simulation) to the control output. Due to the specifications of the controller, there is greater utility in making use of analog input control because of it's property to be continuous in the time domain. Digital input to this controller would be limited to 8 finite speed settings and resolves itself to a discrete signal input, which would limit the efficacy of the simulation to communicate speed commands to the controller with a certain degree of specificity. Analog control therefore provides a greater degree of input signal resolution and lends itself well as an input control modality in the context of time dependent control of mechanical actuation.

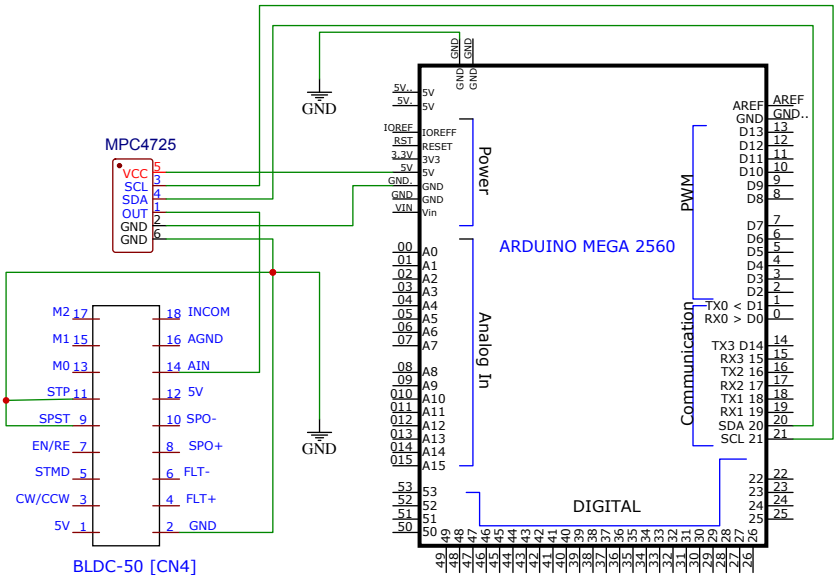

FIGURE 5.6: Pin-Out Configuration for Communication between Controller and DAC

Signal data was thus communicated from the simulation to the speed controller by making use of the **I2C** protocol for data transfer. This protocol enables the instantaneously generated speed command signal to be parsed in a digital format to the **Serial Data (SDA)** port of an **Arduino Mega 2560** micro-controller. From the micro-controller, the signal is converted to an Analog format through a digital to analog converter (*DAC*) **MPC4725**. In order for the DAC to convert this signal into a proportionate speed command, the simulation system must normalize the speed command signal relative to the speed range that can be achieved by the motor using analog input in the range of **0V - 5V**. This is the subsequent EMF signal domain with which the *I2C* protocol is built on.

The simulation system thus normalizes the instantaneous speed command signal within the range of the *uint16* data type in order for the necessary bit shifting operations to generate the appropriate data packet necessary to communicate with the DAC and produce the required output voltage. This is only possible by standardising the rate of data transfer to be a consistent **9600 bits/second** across all control elements resolved for signal data handling. The block system leverages the I2C library within the *Arduino Support Package* made available by *Mathworks* for use within *Simulink*. The resulting circuit wiring configuration from the micro controller to the DAC is illustrated in *Figure 5.6*.

5.3.2 Coupled Pump Design Specification

Choosing the correct pump consistent with a suitable driving force (motor) can pose extensive functional constraints on flow execution and is thus a vital design consideration. The innovation of low friction magnetically

levitated centrifugal pumps have allowed for efficient and accurate maintenance of flow while minimising resultant blood damage. These pumps have thus been extensively recruited in the perfusion space and have become a preferential option for use during cardiopulmonary bypass in some case. Depending on the control signalling, centrifugal pump heads can be used to dynamically vary the flow profile by varying the instantaneous pressure gain developed across their inlet/outlet. This allows the pump to exhibit both pulsatile and steady continuous flow dynamics. A centrifugal pump is thus an ideal choice for use in this circuit configuration.

Driving Unit

FIGURE 5.7: *Sorin* Pump Driving Unit (Sorin Group Italia, 2020)

As previously stated, the impeller of the pump cone is driven using magnetic coupling provided through a static fixed assembly of the pump cone casing to the driving unit. The driving unit creates rotation of the impeller through the changing magnetic field of an internal bearing driven by an input shaft. One rotation of the input shaft translates to approximately **35** rotations of the cone impeller, which is indicative of a **1:35** gear ratio of the driving unit pictured in *Figure 5.7*.

Centrifugal Pump Cone

In order to generate pump head without hemolysis we rely on the use of a magnetically rotated impeller within a pump head casing. It is important to note that the impeller has no direct bearing or shaft coupling which allows it to freely accelerate and decelerate in accordance with the corresponding driving load and upstream fluid pressure changes. This free movement of the impeller creates minimal blood damage during operation which means that it can be operated with greater responsiveness to changing flow/pressure requirements. Furthermore, the lack of direct coupling means that there is no negative rotation possible. By extension this means that the maximum rate of impeller deceleration during operation is directly dependant on the net effect of impeller rotor and fluid inertia.

The curve in *Appendix C.3*, shows the operating parameters of the *Liva Nova Revolution* pump head illustrated in red. The figure plots established pump head in millimetres mercury as a function of revolutions per minute of shaft speed. Its maximum rated discharge pressure is **800 mmHg** and can thus produce a maximum flow rate of **8 lpm**.

Considering the parameter ranges and variable characteristics of input and output signals to the pump control block in *Figure 3.4*, the pump head is considered suitable for this use case where maximum pump discharge pressure is not required to be greater than approximately **150 mmHg** as an upper design specification and non-conservative estimate. Furthermore, according to the characteristic curve, **150 mmHg** is achieved at an impeller speed of approximately **1700 rpm**.

5.3.3 Test Rig Design and Assembly

Design of the testing rig was conducted in *Solidworks* mechanical design software. Using a CAD model for the motor made available by the supplier, an assembly of all prospective components and their spatial positioning in relation to one another was achievable. Where *CAD* files for a component were unavailable, a best effort was

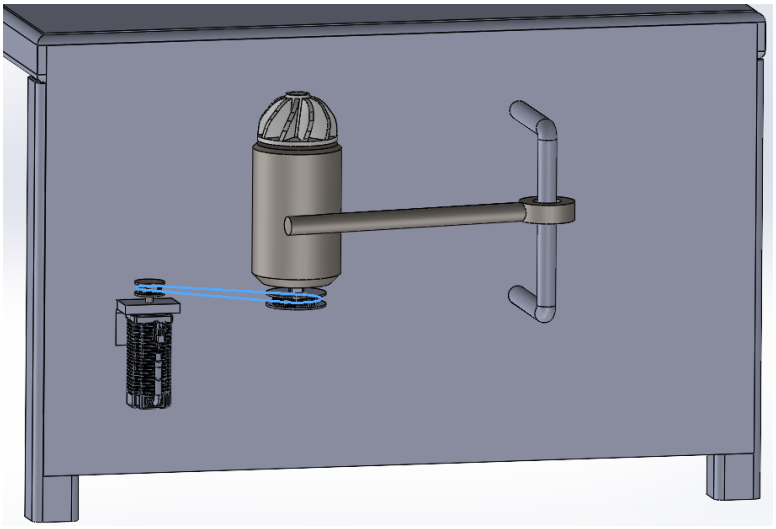

FIGURE 5.8: *Solidworks* Test Rig Assembly Design

made to emulate the part in the software by creating a part model based on measurement of existing physical part dimensions. This was the case for the pump driving unit. Due to the use of a belt coupling the driving and driven gears, consideration of component positioning within the assembly ensured that the faces of the gears were oriented so that the belt may run horizontally and with a sufficient clearance from the rig.

The driving unit was positioned horizontally on the rig so that during assembly it may be adjusted vertically to ensure that gear faces are ideally aligned for horizontal belt coupling relative to the fixed position of the motor. Furthermore, the ability of the driving head to be axially adjusted and fastened means that when mounted to the rig in a vertical manor, axial adjustment to the length of the horizontal leaver arm creates a method in which belt tension may be created. This modality of belt tensioning ensures that small position variations of mounted components can be accounted and that optimal tension between the two gears can be achieved. This is an essential aspect of the test rig design, because without adequate and maintainable belt tension, the motor will not be able to control the driven shaft with its designed functionality.

5.4 System Pump Profile Matching

In order to adjust the system to accurately represent the flow characteristic of the pump as defined by it's operating specification, we must appropriately configure the block representing centrifugal pump operation within the system model. Configuration of the model pump requires specification of a set of operating parameters that govern its operating characteristic across a specified input domain. These parameters are exclusive to model pump operation and do not account for any energy losses outside of the immediate input/output terminals of the pump. The main aim of determining and assigning these parameters is to ensure that the recruited physical pump of certain dimensions and specification having its characteristic discharge is in an ideal sense represented by pump model within the system.

Once validated, we may then look to the flow outside of the pump in relation to it's operation within the circuit and use measurement observations of physical flow in relation to modelled flow as a means to correct for hydraulic, frictional, mechanical and gravitational losses that otherwise are misaccounted for. Doing this correctly directly hinges on the accuracy with which the spec. sheet pump is modelled in an ideal sense.

5.4.1 Operating Characteristic Curve Interpolation

We begin by taking note of flow measurement data and extracting a low-resolution dataset of points on the curve (see *Appendx B.3*). Using the set of given data points we use linear interpolation to derive the characteristic cartesian equation of the *P-Q curve* for the pump defined by the specification sheet.

Using the resultant characteristic curve, we may then generate a dataset of points on the curve that represent pump operation with a greater degree of resolution which allows for more accurate curve fitting. The resulting dataset of discharge pressure with respect to the angular velocity at which the impeller is driven can then be used as input in to the characteristic pump equation of the theoretical model pump. The model characteristic equation is defined as a polynomial approximation of the *Euler Pulse-Momentum* equation as follows:

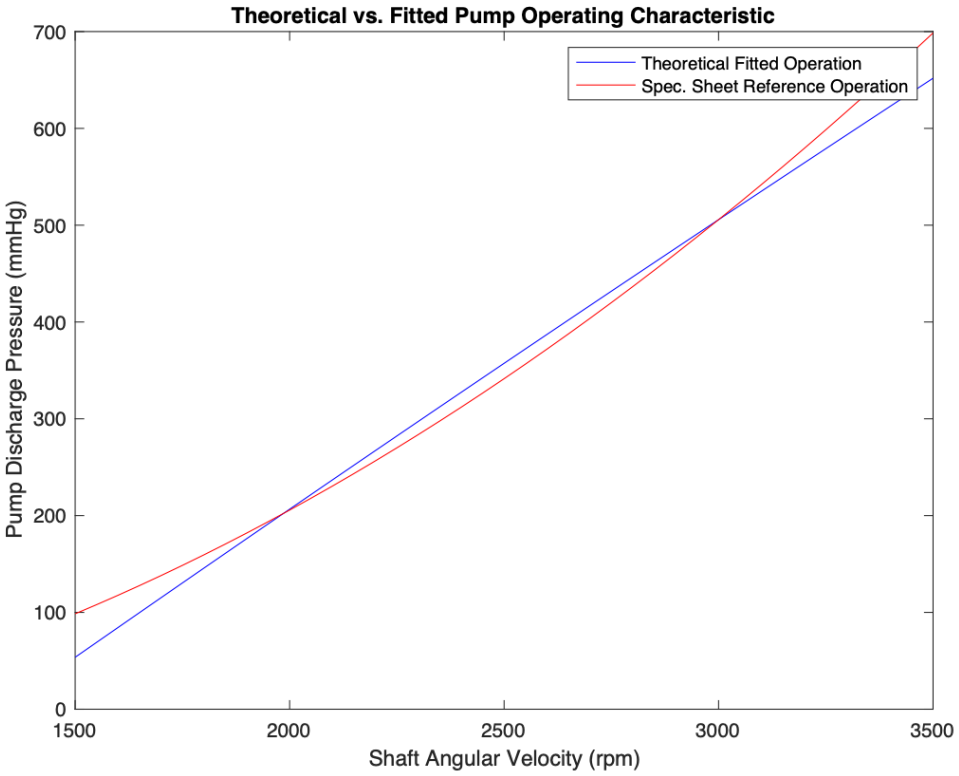

FIGURE 5.9: Quadratic Interpolation of Pump Operation as per specification sheet using Estimation for C - approximating pump coefficients

$$p_{\text{ref}} = \rho_{\text{ref}} \left(k(c_0 - c_1 q_{\text{ref}}) - c_2 q_{\text{ref}}^2 - c_3 (q_D - q_{\text{ref}})^2 \right) \tag{5.2}$$

5.4.2 Heuristic Non-Linear Objective Function

The discharge pressure can then be computed with respect to the input parameters governing the shape of the theoretical performance curve (i.e c_0, c_1, c_2, c_3, k). The resultant sum of errors between the actual output values and theoretical output values can be used as an objective function for minimisation in the formulation of a non-linear solver problem . Thus, the optimal parameter values that yield a curve as closely related to the specification sheet pump can be solved for by iterating through solutions calculated through the use of a **Generalized Reduced Gradient** nonlinear solving algorithm. The cost minimisation problem setup can thus be set up in terms of either the parameters of c or in this case θ with respect to the ω domain denoting input shaft angular velocity in rad/s as follows:

Find the parameters θ that best fit the transfer function $H(\omega)$, such that:

$$\min_{\theta} \sum \left\| H(\omega) - \frac{\theta_1 \omega^2 + \theta_2 \omega + \theta_3}{\omega^2 + \theta_4 \omega + 1} \right\| \tag{5.3}$$

5.4.3 Theoretical Model Pump Parameter Assignment

Taking note of the residuals with respect to the actual and theoretical pressure results across the input domain - the lowest residual value using the current dataset resolution occurs at $\omega = 3000rpm$. This is then chosen at the value for ω_{ref} which produces a q_{ref} value that optimally matches ideal spec. sheet pump operation. The simulation model pump can subsequently be configured using the set of parameters shown in *Appendix C.1*.

5.5 Model System Identification

Modelling the theoretical system hydraulic flow in an ideal sense neglects factors such as tubing friction and other losses. This is why we expect a certain degree of inherent flow measurement variance in comparison to simulated signal measurements.

Drawing on the results of trial data, we are able to determine the degree to which the theoretical *(Simulation)* system and the physical *(Bench Test)* system differ. By quantifying the magnitude of actual and theoretical system variability with respect to the relevant flow measurements, we may interpolate empirical parameters for the physical system pump operation and apply them in conjunction with pressure-velocity correction factors to the theoretical system. This thus increases accuracy of system flow simulation in the context of its ideal designed operation and with respect to specific physical circuit components and physical fluid behaviour.

This is the subsequent, final step of hydraulic simulation validation. In context, the remainder of the simulation model *(i.e that which falls outside of the hydraulic simulation aspect)*, purely serves to create the specific perfusion scenario and fundamental set of signals under which we would expect the pump system aspect to operate in relation to.

5.5.1 Method

In order to match the theoretical system to emulate the dynamics of the perfusion test rig, we must define the system using equations associated with the relevant energy transfer principles. By doing this we are able express the output measurement of the theoretical system in terms of it's input, state variables and free parameters. The system of equations should represent the dynamics across every component in the system between the input and output signal that may deviate total energy dynamics in a nonlinear fashion. Additionally, every subsequent equation must be expressed in terms of the model block parameters are intended to be corrected for.

Using *MatLab's* system identification toolbox we may parse in vector of input-output samples of a given simulation. By employing the use of a **Non-Linear Grey Box Model**, we may conduct parameter estimation that allows us to fit the output of the differential equation simulation against the actual measures theoretical output. By iteratively varying the value of initial parameters to the subsequent model estimated values we may configure the set of differential equations to closely resemble the theoretical output of the model system. We have therefore, defined a non-linear system of equations and linearised it around components in the system that involve the estimation of free parameters. This serves as an empirical verification of the non-linear grey box model.

By extension, using the same non-linear grey box system model and the same input signal, we may now provide a set of input-output sample pairs measured based on outputs of the actual pump-tank system. This set of sample points can now be used as a validation set from which the model may conduct parameter estimation. Parameter estimation is achieved through the iterative varying of free parameters to calculate the result of an objective cost function. Minimisation of the cost function is achieved using the **Trust-Region Reflective Newton** algorithm. The result of this process yields a set of scalar parameter values that fit the output measurement signal of the theoretical model to the output measurement signal of the actual model.

A system matching validation step can be followed by using the set of estimated parameter values from the actual data validation set and plugging into the respective block components in the model. Running a simulation using the plugged in values should yield a final measured output signal that matches the actual physical measured output signal within a reasonable degree of error. Ideally, the general input-output proportionality should be closely matched and the order of the output measurement curves should correlate.

5.5.2 Non-Linear System of Ordinary Differential Equations

The formulation of the Non-Linear System is defined using the mathematical relations as follows:

Assuming a **Linear Time Invariant (LTI)** system for the pump, the output signal $y(t)$ is the convolution of the input signal $u(t)$ with the impulse response of the pump $h(t)$:

$$y(t) = u(t) * h(t)$$

Given $U(\omega)$ and $Y(\omega)$:

Compute the Fourier transforms of the input and output signals:

$$U(\omega) = \mathcal{F}\{u(t)\}$$

$$Y(\omega) = \mathcal{F}\{y(t)\}$$

In the frequency domain, this relationship can be expressed as:

$$Y(\omega) = H(\omega)U(\omega)$$

where $U(\omega)$ and $Y(\omega)$ are the Fourier transforms of $u(t)$ and $y(t)$, respectively, and $H(\omega)$ is the transfer function.

$$H(\omega) = \frac{Y(\omega)}{U(\omega)}$$

Parameterize the transfer function $H(\omega)$ by the pump parameters $\theta = [\theta_1, \theta_2, \theta_3, \theta_4]$:

$$H(\omega) = \frac{\theta_1\omega^2 + \theta_2\omega + \theta_3}{\omega^2 + \theta_4\omega + 1}$$

The second-order differential equation describing the system in the time domain is thus:

$$\ddot{y}(t) + \theta_4\dot{y}(t) + y(t) = \theta_1\ddot{u}(t) + \theta_2\dot{u}(t) + \theta_3 u(t)$$

where $y(t) = p_2(t)$ and $u(t) = p_1(t)$.

And the approximating polynomial from the *Euler Pulse Moment Equation*:

$$p_{\text{ref}} = \rho_{\text{ref}}\left(k(c_0 - c_1 q_{\text{ref}}) - c_2 q_{\text{ref}}^2 - c_3(q_D - q_{\text{ref}})^2\right)$$

Two-Tank Transfer Equations

The next step is to specify a model structure describing the two tank system. To do this, let $x_1(t)$ and $x_2(t)$ denote the water level in the upper and the lower tank, respectively. For each tank, fundamental physics (mass balance) states that the change of water volume depends on the difference between inflow and outflow as (i = 1, 2):

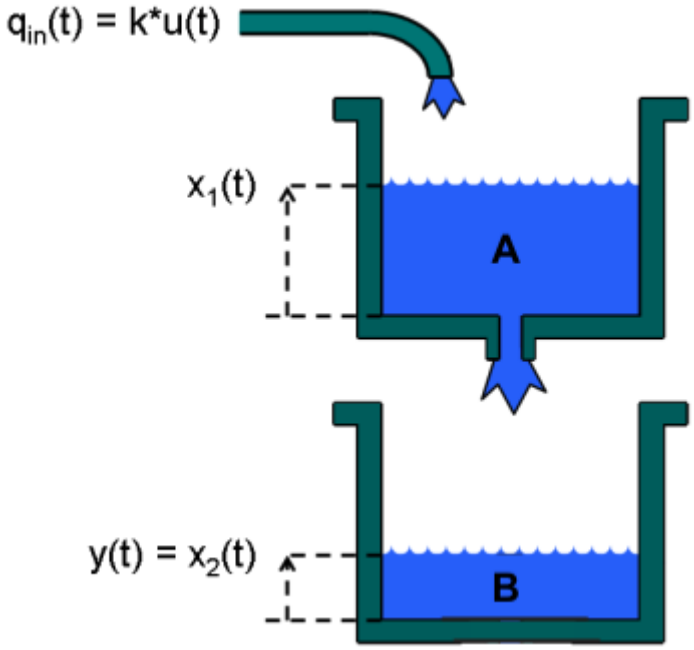

FIGURE 5.10: Two-Tank Flow Diagram

$$\frac{d}{dt}(A_i x_i(t)) = Q_{\text{in}i}(t) - Q_{\text{out}i}(t)$$

where A_i [m^2] is the cross-sectional area of tank i and $Q_{\text{in}i}(t)$ and $Q_{\text{out}i}(t)$ [cm^3/s] are the inflow to and the outflow from tank i at time t.

For the upper tank, the inflow is assumed to be proportional to the voltage applied to the pump. Since the outlet hole of the upper tank is small, Bernoulli's law can be applied, stating that the outflow is proportional to the square root of the water level, or more precisely that:

$$Q_{\text{out2}}(t) = a_1\sqrt{2gx_2(t)}$$

where a_1 is the cross-sectional area of the outlet hole and g is the gravity constant. For the lower tank, the inflow equals the outflow from the upper tank, i.e., $Q_{\text{in3}}(t) = Q_{\text{out2}}(t)$.

Putting all these facts together leads to the following state-space structure:

$$\frac{d}{dt}x_1(t) = \frac{1}{A_1}\left(ku(t) - a_1\sqrt{2gx_1(t)}\right)$$
$$x_2(t) = \frac{1}{A_2}\left(a_1\sqrt{2gx_1(t)}\right)$$
$$y(t) = x_2(t)$$

State-Space Representation

The system of equations is given by:

Input Equation:

$$\mathbf{u}(t) = \omega(t)$$

$$\dot{x}_0(t) = \frac{\theta_1 \cdot \omega(t)^2 + \theta_2 \cdot \omega(t) + \theta_3}{\omega(t)^2 + \theta_4 \cdot \omega(t) + 1}$$

$$\dot{x}_1(t) = k \cdot \frac{(x_0(t) - p_{Ao}(t)) \cdot \pi \cdot a_1^4}{128 \cdot \rho}$$

$$\dot{x}_2(t) = \frac{1}{A_1(t)}\left(\dot{x}_1(t) - a_2 \cdot \sqrt{2 \cdot g \cdot x_2(t)}\right)$$

$$x_3(t) = \frac{1}{A_2(t)}\left(a_2 \cdot \sqrt{2 \cdot g \cdot x_2(t)}\right)$$

Output Equation:

$$\mathbf{y}(t) = x_3(t)$$

5.6 Non-Linear Grey Box Calibration

In order to accurately estimate parameter values and correction factors that of the theoretical model such that the output signal matches that of the physical model output measurement, we must ensure that the current set of parameters and the non-linear system of equations are able to sufficiently approximate theoretical model output. We begin by taking the parameter values for estimation represented in the system and setting their value to the current value of the same parameters modelled in the component blocks within the model. Using these values as initial settings, we run the inputs through the non-linear system and produce a simulated output.

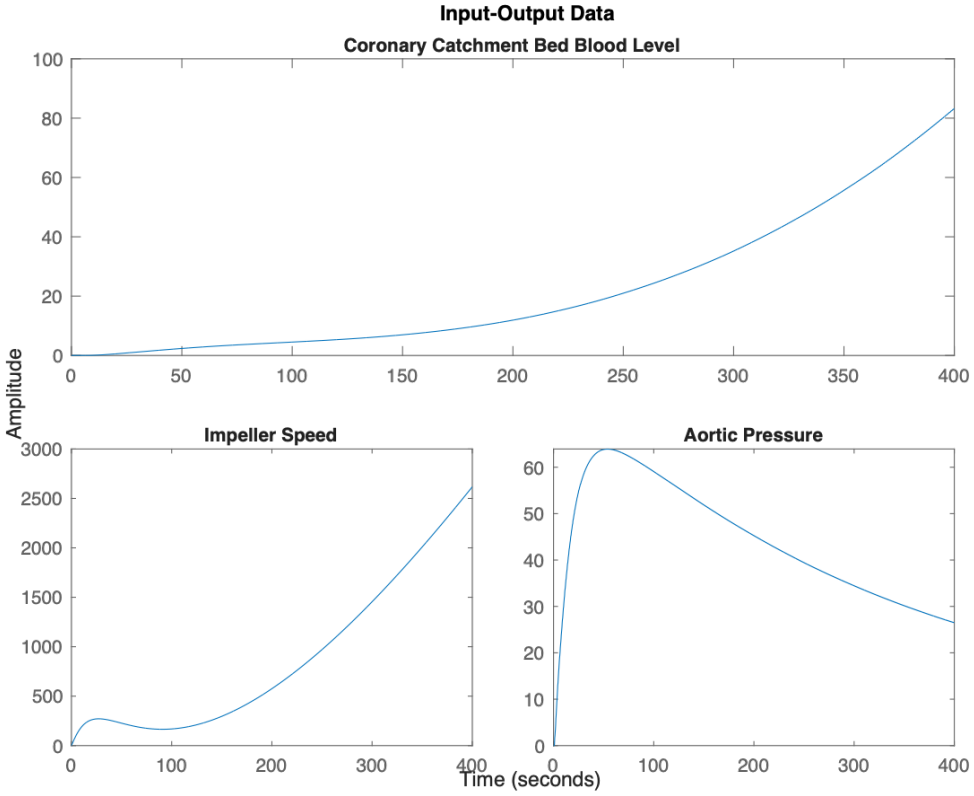

FIGURE 5.11: Input and Outputs of Theoretical Pump Model

The parameters determined for estimation relate to the variables not considered to be fixed constants within the system. For example, the parameter governing fluid density is considered a fixed constant and therefore does not require estimation. In this case, the initial specified value will remain the same.

Of the total number of parameters expressed within the system of equations each of the parameters that are considered for estimation can be thought of as free parameters and as such do not contribute towards an increase in the degree of solution constraint toward a particular solution space. Therefore, the total number of free parameters denote system's number of degrees of freedom. Additionally, due to the manor in which the parameters are expressed within the system equations, variance of parameters are not commensurate. This means, that a set of parameters impacting the solution of one of the states of the system will not proportionately affect the other states. Therefore, parameters represented in the equations expressing other states will dynamically change in range according to the specific region of the solution space specified by the original set of parameters chosen to be estimated. This shows that parameters are not independent of each other and can therefore can cause conflict during estimation when attempting to converge toward a local or global minimum relative to an objective cost function. For this reason, priority of parameter approximation was implemented by varying the total number of degrees of freedom of the estimation process in order to converge toward a global minimum, before remaining parameters are free'd allowing for the refinement of the solution further toward a more optimal final value. This was carried out by focusing on parameter estimation values of the set of Theta constants denoting the pump's operating characteristic as a dynamic response. By iteratively estimating these parameter values and replacing them as the new initial conditions after which another degree of freedom is made available, we were able progressively converge toward a solution outcome that optimally models the theoretical system output response.

5.6.1 Model Initialisation

Validation using the obtained parameters θ^* can be seen in *Figure 5.12* by comparing the reconstructed signal using these parameters against the original signal. A close match indicates that the parameters θ^* effectively model the pump behaviour. We notice marginal deviation of the two curves across the operation domain of angular velocities.

Using initial estimates for free parameters and actual measurements of fixed parameters based on initialisation values of the *Simscape* component blocks, a simulated system response may be generated based on the

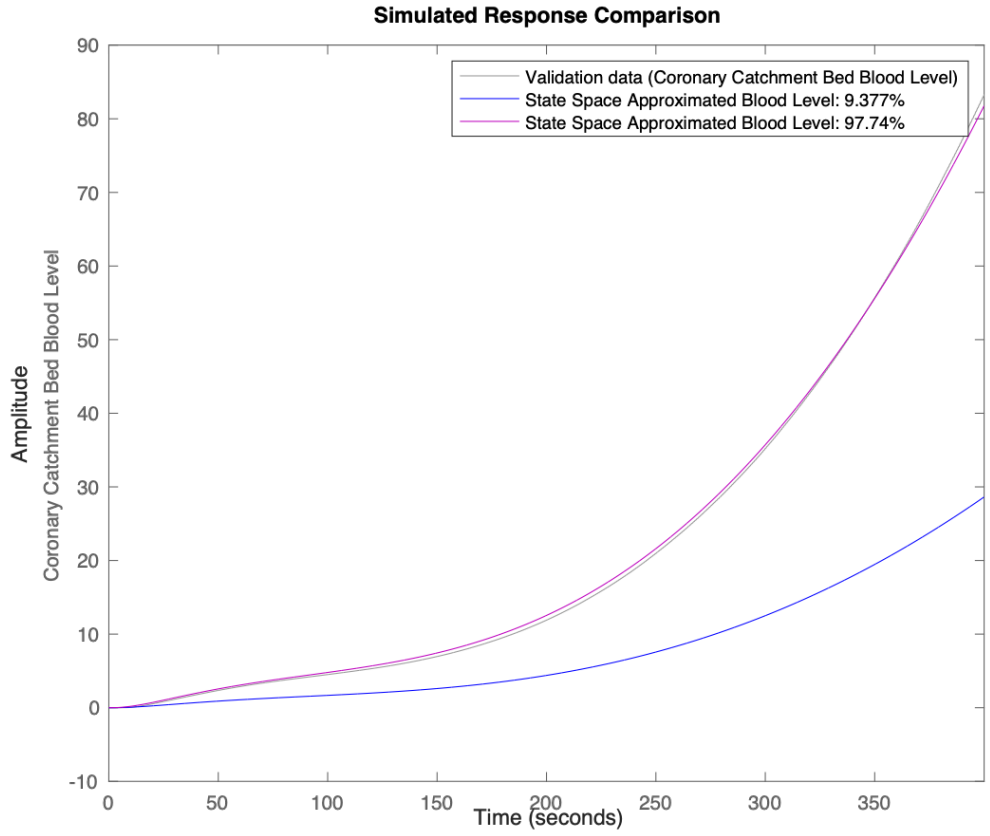

FIGURE 5.12: Parameter Estimated Output Comparison

simulation of the nonlinear system of equations using the two input signals of **Aortic Pressure** and **Impeller Speed**.

Then by constraining fixed parameters and we allow for the estimation of free parameters using an iterative nonlinear solving process. Upon completion of this step we notice the optimised output response associated with the purple signal estimation of free parameters in *Figure 5.12*. The signal shown in blue is associated with the initial free parameter estimates, the signal shown in purples corresponds to the estimated parameter estimates and finally the grey line in the figure serves as the validation output data from the simulation against which the optimisation cost measurement is derived from.

Table 5.3 Initial and Estimated Parameter Comparison

Variable	Parameter	Initial Value	Estimated Value	Estimation Status
P_1	Upper Tank Cross-Sectional Area [cm^2]	35.911	35.671	Free
P_2	Pump constant	0.30974	0.89838	Free
P_3	Upper Tank Area of Inlet Port [mm^2]	1.0087	1.0293	Free
P_4	Upper Tank Area of Outlet Port [mm^2]	0.39398	0.64099	Free
P_5	Gravity constant	9.81	9.81	Fixed
P_6	Lower Tank Cross-Sectional Area [cm^2]	9.9793	9.3497	Free
θ_1	**First Approximating Coefficient**	1.35e+05	1.3508e+05	Free
θ_2	**Second Approximating Coefficient**	-1587.6	-1845.4	Free
θ_3	**Third Approximating Coefficient**	4485.4	4103.5	Free
θ_4	**Fourth Approximating Coefficient**	3.5783e+05	3.5918e+05	Free
P_7	Fluid Density	1069.68	1069.68	Fixed

Using the same **Generalized Reduce Gradient** nonlinear solving method used for initial pump parameter estimation based on specification sheet data, we may estimate the parameters of c using the same pump correction factor k to determine the associated approximating coefficients used to initialise the pump in the *Simscape* model. After each estimation process, the estimated parameter values are used to replace the initial values used while another set of validation data is generated using the new values for the parameter set of c. Model

calibration is completed by iteratively varying the *c-value* parameters upon successive estimations of the θ parameters. The parameters corresponding to the values of θ are shown in bold in *Table 5.3*. This step is repeated until the cost function of the estimation process has converged to an absolute minimum and there are no longer any subsequent improvements of the estimated curve's fit to the validation output. This indicates that the non-linear system of equations using the set of estimated parameters is optimally configured to numerically model the system dynamics of the theoretical *Simscape* model.

The grey-box model defined using the estimated parameters may now be used to complete parameter estimation against physical signal measurements as the validation set. The resulting best fit is associated with a similarity of **97.74%**. Upon inspection it can be seen that the initial output simulation and optimised parameter simulation produce to curves overlapping and indistinguishable from one another. This illustrates the convergence of the initial parameter estimation with the estimated solution of highest achievable accuracy with respect to the current system of nonlinear equations. It can be seen that the resultant pump discharge pressure-speed relationship based upon the approximating coefficient parameters of θ produced observably higher magnitudes of pressure discharge than that indicated from the spec. sheet of the pump in *Appendix B.3*. This is an expected deviation attributable to the requirement of varying flow magnitude as a control response within the simulation from which the profile shown in *Figure 5.12* was measured. The pressure to impeller-speed relationship from the specification sheet plot in *Appendix B.3* shown in red is however, a steady-state response in which the flow delivery is kept at a constant **5 lpm**, thus differentiating this pressure profile from that of the established dynamic pump response produced *in-silico*.

5.7 Summary of Investigation and Key Findings

(a) In this chapter, the design development and assembly of a test rig perfusion circuit was detailed to investigate design factors required for control of fluid flow discharge delivered by a centrifugal pump as determined and by signal computation of an *in-silico* hydraulic simulation circuit.

(b) The perfusion simulation was implemented and executed through serial connection via a microcontroller to a computer concurrently executing the *Simscape* model.

(c) Parameters and system state initialisation of the simulated hydraulic circuit informed design considerations of the test rig such as the height and orientation that components were fixed at in relation to a common datum.

(d) Hydraulic signals were configured to use initial values representative of a best estimated starting point for the characterisation of the components used in the physical test rig such as the centrifugal pump. These parameter starting points were determined through the use of non-linear numerical solving techniques to relate simulation model parameters governing characteristics such as **Torque Dependent Pressure Differential, Pump Delivery** and **Brake Power** to actual test rig circuit components by applying minimisation principles to the residuals of specification sheet curve fitting.

(e) The methodology for correction of the simulation based on test rig trial results was developed and discussed by showing the initialisation and calibration of a state-space based non-linear grey box estimation model for system identification. Calibration was carried out by determining the state-space set of parameters needed to optimally and most accurately represent the dynamics of simulation model outcome signals such as accumulated volume theoretically delivered to the hypothetical coronary vascular bed. The resultant calibration accuracy achieved was **97.74%**.

(f) Finally, the implementation of the hydraulic circuit and the subsequent *in-silico* generated signals such as the approximated **Centrifugal Discharge Pressure** was shown in relation to **Impeller Speeds** anticipated during the operation of the test rig in parallel with the perfusion simulation.

Chapter 6

Testing Outcomes, Analysis and Model Validation

This chapter details the process undertaken to investigate characteristics of fluid flow through the test rig circuit designed and assembled in *Chapter 5*. The simulation executed detailed by the *in-silico* simulation model was initialised to replicate perfusion of the Aortic Root and it's major arteries through the implementation of the rigid body phantom presented in *Chapter 4.3*. A heart rate of **100 bpm** was used in simulation and target root pressure for control and maintenance was set to **60 mmHg**. Due to mechanical limitations of the pump-gear complex, **PID** control parameters of the feedback control loop were relaxed to slow the rate of dynamic response reducing the resultant torque load and current draw from the power delivery system. This created a longer real-time simulation time domain allowing for the current design configuration to be used in trialling without exceeding maximum operational conditions and/or overheating and damaging any circuit hardware. This was achieved through iterative refinement of initial parameter values and component functional parameters relating to the motor, pump, reservoirs and other associated hardware components.

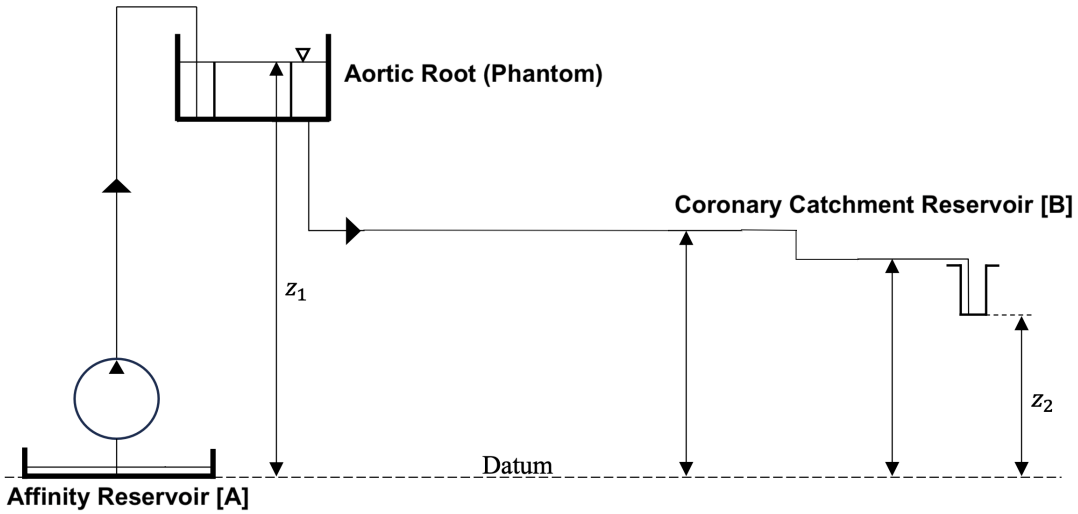

FIGURE 6.1: Experimental Test Rig Setup

Correction factors applied to the hydraulic aspect of the *Simscape* model will be determined through application of the calibrated **Non-Linear Grey Box** system identification and parameter estimation procedure detailed in *Chapter 5* to resulting flow data measured during trial testing. The calibrated **Non-Linear Grey Box** procedure will then be used to compare the the *Simscape* signal data of Coronary Reservoir Fluid Level/Volume and Coronary/Aortic Flow against the same measurements from the inferred from physical data captured during bench testing.

Validation of the hydraulic aspect of the *Simscape* model can be achieved through the comparison of simulation output signals with the analogous physical flow measurement dataset after the application of relevant correction factors. Closely matched signals indicate that the *Simscape* model has been correctly adjusted to account for the physical fluid flow dynamics expected within the assembled test rig perfusion circuit.

Final analysis made use of a cross-comparison between the CFD Aortic Root model velocity and flow measurements at boundary conditions of the polyhedric mesh simulation against measured volumetric flow and inferred velocity data captured through each of the respective phantom arteries.

6.1 Trial 1: Steady-State Flow Analysis

Conducting a set of steady-state flow experiments using the test rig, enabled observation of fluid behaviour under varying pressure conditions within the test rig circuit. Non-ideal flow conditions, influenced by factors such as mechanical, hydraulic, and frictional losses, introduce variability in resulting flow. Deviations from expected ideal flow behaviour allow these losses to be quantified in relation to configuration of the test rig circuit elements. Primary factors believed to contribute to divergent flow behaviour include reduced mechanical efficiency associated with belt slipping, frictional impacts of interconnected tubing of varying lengths, pressure losses encountered at tubing connections, hydrodynamic pump losses associated with impeller slip resulting in reduced discharge pressure, fluid loss at the tube-cannula attachment and finally varying degrees of of hydrostatic pressure in the circuit reservoirs contributing to differing resultant pump head. An overview of the experimental setup can be referenced in the diagram of *Figure 6.1*.

These losses contribute toward a net reduction of mean flow during experimental flow time. Other losses that contribute to variable circuit flow behaviour have been accounted for in the simulation model design detailed in *Chapter 3*. For example, pressure loss across the oxygenator is modelled as a constant pressure drop using a model resistive element. This informs calculation of required input flow at the cannula required to achieve desired target pressure. The factor that contributes to variable flow rate with respect to simulation run time is however the change in hydrostatic pressure present within the affinity reservoir. The reduction of fluid volume results in a drop in fluid level causing a change in instantaneous pump head. This phenomenon obviously only occurs when fluid is being transported against gravity and into a separate reservoir. Therefore, in order to approximate the effect of this loss, flow data was measured with respect to varying degrees of fluid level height within the affinity reservoir. In order to isolate the effect of changing pump head, this data was captured in relation to a steady continuous flow through the circuit achieved using a constant pump delivery associated with an impeller speed of **15 rpm**.

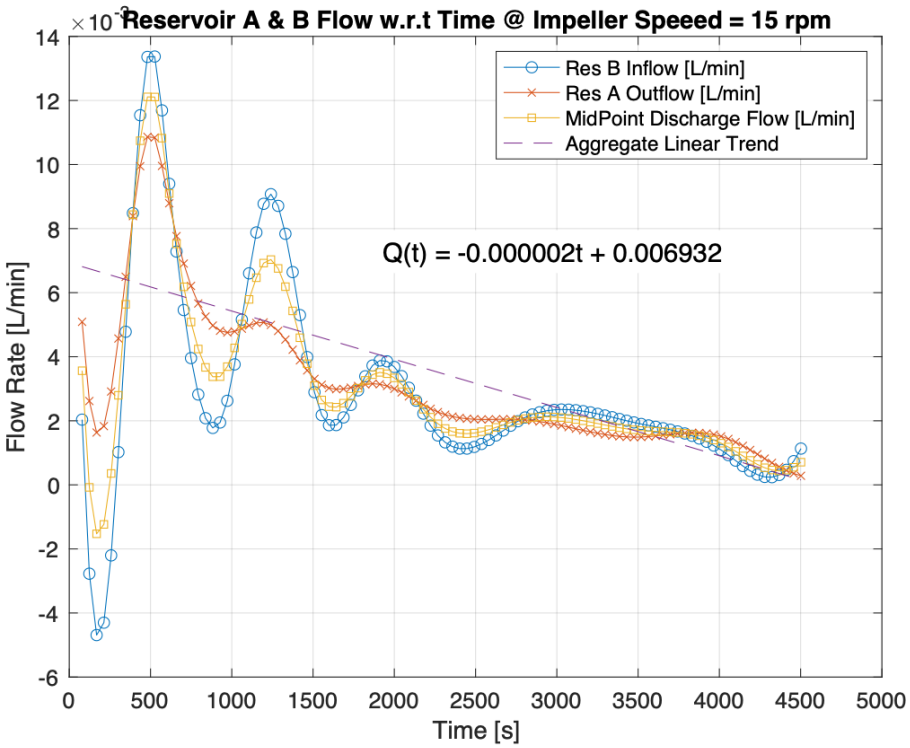

FIGURE 6.2: Steady-State Circuit Flow Variation

Due to the differing geometries of each reservoir, there is a non-proportional change of accumulated fluid level across reservoir respective volume. Therefore, for example a change of volume from **100mL** to **200mL** in **reservoir A** may yield a fluid level change of **2 cm**, while a change from **200mL** to **300mL** may yield a level change of **1.5 cm** in **reservoir B** all with respect to a common datum. In order to control the effect of varying reservoir geometry, the volume-height profile of each reservoir was normalised to produce a common scale of fluid volume measurement that yields a linearly proportionate change in associated fluid level. The normalised fluid level height above the datum at each time interval could then be determined by interpolating the recorded volume with respect to the normalised volume-height profile of each reservoir respectively. The

original and normalised tank profiles for each reservoir have been tabulated and illustrated in *Appendix C.7.2 & C.7.3* respectively.

By measuring time taken between set intervals of fluid volume reduction from the affinity reservoir A and measuring the associated fluid volume accumulation in the corresponding catchment reservoir B, the resultant circuit flow from A to B was calculated. By correlating respective volume values of each reservoir with the fluid level height above a set datum (in this case, Ground was used) the resulting flow changes can be analysed with respect to the changing degree of hydrostatic pressure present in the **Affinity Reservoir (Reservoir A)**. Due to fluid entering the **Coronary Catchment Reservoir (Reservoir B)** at the top, there is no net effect on pump head as the reservoir increases in volume. The drop in fluid level of Reservoir A solely contributes toward the changing value of required pump head. The rate of change of the normalised fluid level height corresponding to the instantaneous volume of fluid in Reservoir A is thus directly proportional to the changing required Pump Head. By extension so is the resulting flow output. This has been illustrated by the logarithmic fit to data in the **Head-Flow Characteristic Curve** shown in *Figure 6.3*.

Taking note of the resultant signal plotted in *Figure 6.2*, there is an evident periodic characteristic of the signal waveform. Each recurrent cycle shows an inequality in flow rate into and out of the respective reservoirs. Every other peak of each of the signals illustrated in orange and blue show a switch from a greater outflow than inflow to a greater inflow than outflow. Considering the measurement data is taken from a closed system where in fluid cannot escape between the time it leaves reservoir A until draining into reservoir B, there is thus a flow mismatch that contradicts *conservation of mass*. Each cyclical peak and trough alternates between the greatest or lowest value of the inflow/outflow at each respective time instance. The two signals shown appear to remain in phase however and proportionately diminish in amplitude with time. In this experiment, the only non-constant variable is the increasing degree of required pump head associated with a drop in reservoir A fluid level. The linear trend line shown in purple approximates the rate at which an aggregated flow signal would decrease in magnitude inversely proportional to an increase pump head. The oscillatory behaviour of the in/outflow signals in this trial are hypothesised to be an indicator of instantaneous changes in resulting flow at each of the reservoir inlet/outlet conditions as the system seeks to establish a net pressure equilibrium.

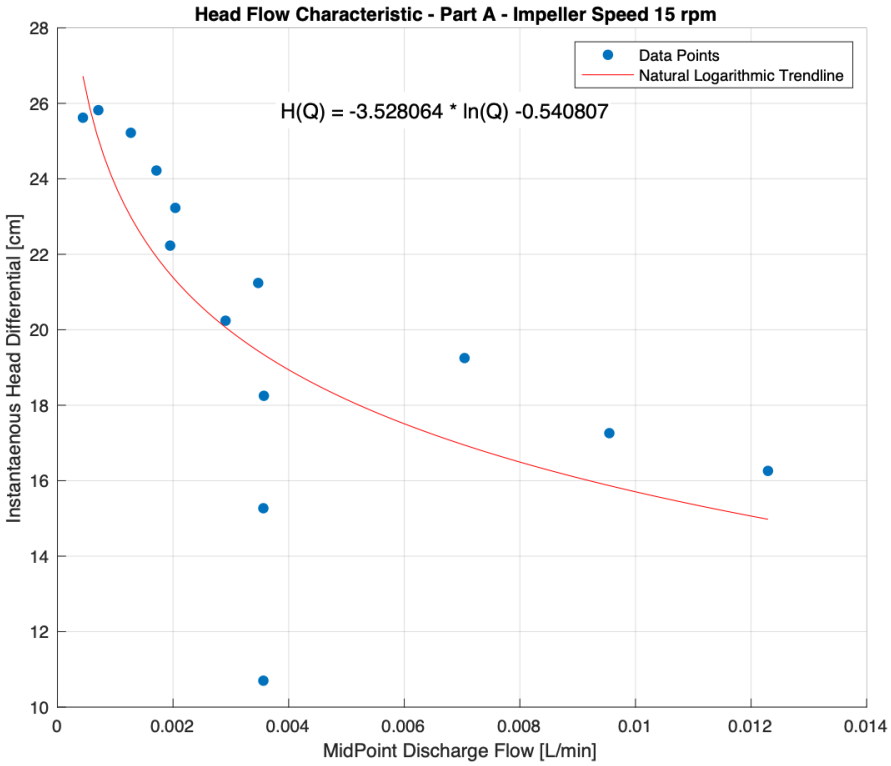

FIGURE 6.3: Head-Flow Characteristic Pump Operating Curve with Losses

Due to changing head as well as impedance of flow as well and pressure drop over circuit components, there is presumably some inherent delay in which the pressure at an in/outlet may change in relation to upstream/downstream flow variations. The delay in time taken for change in pressure gradients between in/outlet conditions explains the "overshoot" characterisation of the associated signal waveforms. The amplitude of overshoot decreases in relation to a net reduction in flow rate. Therefore, the increasing magnitude

of disturbance caused by pump head appears to dampen the system's affinity for overcompensation of localised pressure. This is akin to the concept of forward flow pushing fluid through the circuit along a pressure gradient towards the outlet, after which a theoretical vacuum is created in relation to an increase in positive upstream pressure resulting in a suction type effect at the downstream inlet. Furthermore, by taking note that the hydraulic model for simulation has been configured such that the same collecting reservoir used for de-oxygenated blood drainage is also used for oxygenated supply to the pump, there is consequently a diminished degree of fluid level height change during operation once flow has reached a steady-state. Therefore, to approximate the pump's discharge characteristic relative to an input motor speed, the pump flow value associated with a required pump head most similar to that of the smallest height difference from the estimated constant fluid volume of the affinity reservoir to the cannula level height must be chosen. These measurements are taken when the test rig is set up for dynamic input simulation. The impeller speed chosen thus allows for the pump flow relationship to be determined. This relationship is applied to the *Simscape* model as a correction factor to the **Impeller Flow Mapping** block. The block functions to approximate a required discharge flow from the pump based on an incoming impeller velocity signal. The resulting flow is the product of the impeller velocity and the velocity/flow ratio. This then allows the control system speed command to the motor to be calculated based on a better approximation of the rate of fluid discharge from the pump in this specific test rig configuration.

Assuming the dynamic single tank configuration is run with the intention of hypothetically maintaining a constant volume of **800 mL** in the Affinity Reservoir at a steady-state, the subsequent steady-state required pump head can be interpolated by using the volume/height profile of reservoir A in relation to the datum and subtracting it from the maximum height required to pump the fluid in the hypothetical setup. The head differential can then be mapped to the corresponding flow discharge rate in *Figure 6.3*. In this hypothetical scenario, the resulting correction factor applied for use in the **Impeller Flow Mapping** block for constant reservoir volume of **800 mL** is calculated as follows:

Required Head = Cannula Outlet Height - Reservoir Constant Fluid Level Height

$$118 - 102.85 = 15.15 \text{ cm} \tag{6.1}$$

Using the formula for the logarithmic relationship H(Q):

$$Q = 0.0117 \text{ L/min} \tag{6.2}$$

The resulting correction factor is:

$$m = \frac{\text{Pump Flow}}{\text{Impeller Speed}} = \frac{0.0117}{15} = 7.8058 \times 10^{-4} \tag{6.3}$$

6.2 Trial 2: Dynamic Response Flow Analysis

Applying the impeller speed to flow output ratio determined within the *trial 1 steady-state* analysis for the head height corresponding to a Reservoir A starting volume of **800 mL**, the simulation model was then appropriately corrected. The dynamic response of pump operation within the test rig circuit in relation to the initialised model control system can now be investigated. Using the same experimental apparatus and set up as in the steady-state experiment, the varying speed control signal generate from the *Simscape* simulation was then applied to the pump via the motor controller hardware.

The time taken for fluid to accumulate at set volume intervals within reservoir B was then measured as the primary dependant variable. Note, only the time-dependant volume accumulated within reservoir B was of interest in this trial because the head-flow relationship between the respective in/outlets of the reservoirs was already established and accounted for in trial 1. All height values of inlets and outlets with respect to the common datum remained consistent with the setup from the *steady-state trial*.

This trial was conducted with respect to three phases with the objective of measuring, analysing and determining the control parameters necessary for the characterisation of fluid flow through the testing rig.

6.2.1 Phase 1: Correction Factor Tuning

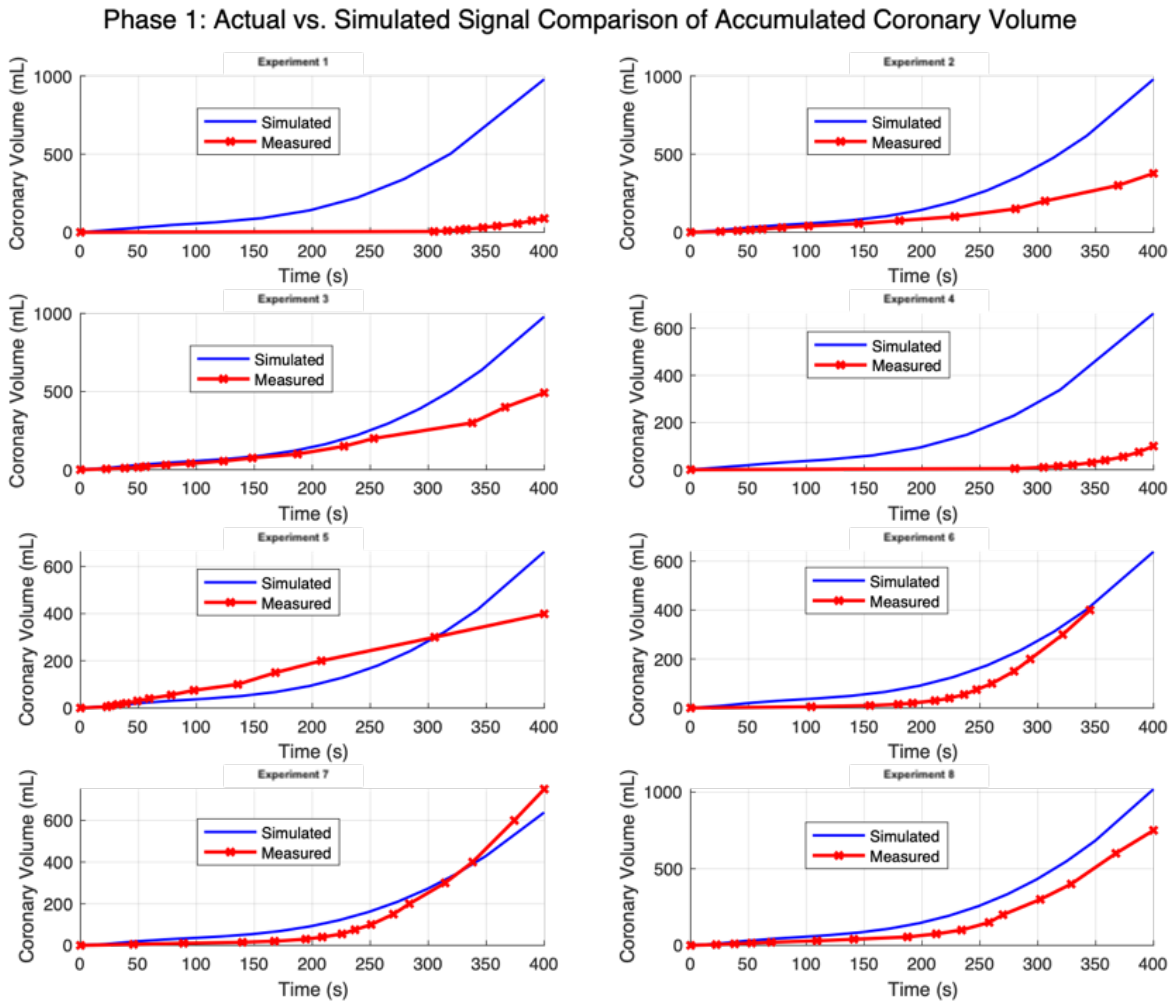

FIGURE 6.4: Comparative Coronary Volume Signal Outcomes

The objective of *phase 1* was to produce an initial set of data after the application of the impeller-flow ratio determined within the steady-state trial. The current system model initialisation serves as a "best guess" starting point to parameter initial values. Thereafter, the predominant focus was to adjust the flow-impeller correction factor from the initial best guess such that the physical data measurements fall within estimation range of the *grey-box model*. Adjustment of this correction factor was informed by two main criteria.

The first being the degree of deviation of the physical measurement from the corresponding simulated signal. This was quantified as the mean of residual values over the simulation period. This deviation is illustrated with respect to each experiment in *Figure 6.4*.

The second criteria used was the measure of deviation of slope/gradient between the physical signal measurement at each successive time interval in relation to the simulated signal measurement. This is illustrated in *Figure 6.5*. A slope that is approximately parallel to the corresponding simulation signal with the experiment provides a good starting point from which parameters with a lesser impact can be estimated for finer tuning. Taking both these criteria as measures of signal similarity allowed for both the shape and magnitude of resulting data waveforms to be quantified in relation to the impeller-flow factor used in each of the associated experiments.

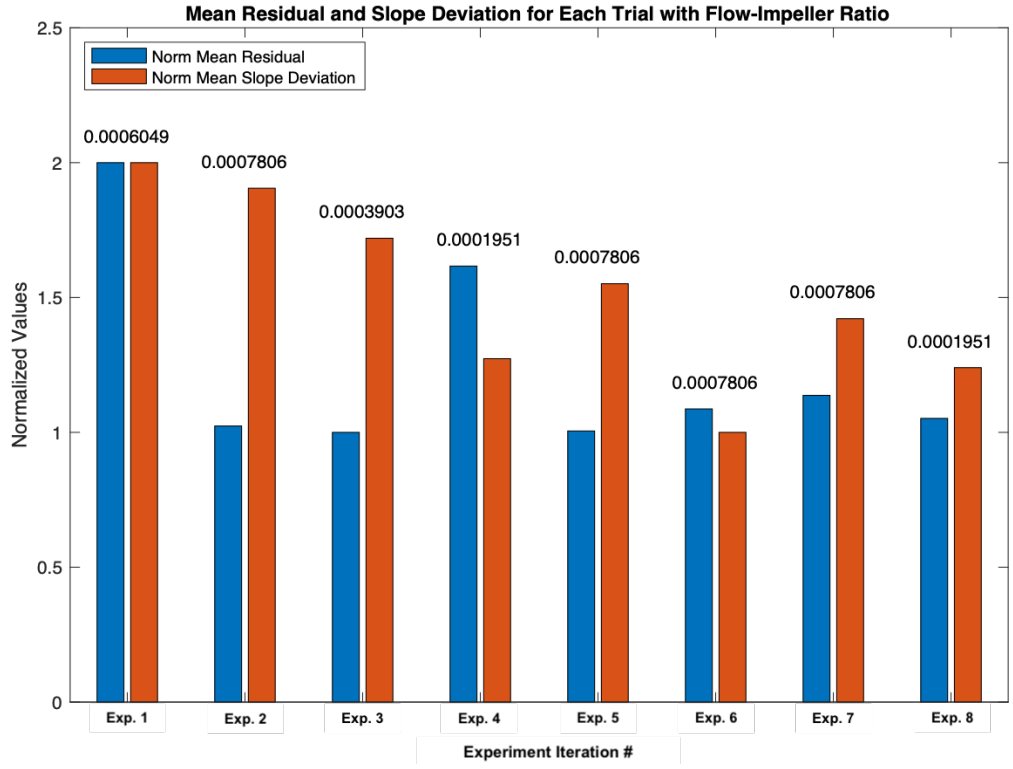

FIGURE 6.5: Experimental Comparison against Respective Simulation Outcome

The correction factor can be adjusted in such a way that the feasible signal range becomes evident. Once established, this feasible region becomes the solution space encompassing all future combinations and variations of parameter estimates. Using the original set of governing parameters from the steady-state trial - initial experiments produced noise and were of an expected lesser degree of accuracy in relation to the simulated signal result in each respective experimental case. This was attributed to mechanical and hydraulic elements of the test rig beginning dry and thus causing flow anomalies. One such example is the friction and stretch present within the connecting belt between the driving and driven gear heads. Starting "cold" with lower initial static friction, the belt undergoes a greater degree of slip over the rotating gear heads, resulting in a loss of mechanical energy that would otherwise translate toward hydraulic flow. Additionally, upon initiation of flow through the circuit even after care has been taken to purge the system of all air bubbles, there are still a number of micro air-embolisms present within tubing and adjacent to component connections. The presence of these air pockets are likely to cause anomalies in fluid flow behaviour particularly depending on where they are located at the onset of each experiment in addition to the their volume magnitude and whether they begin static or not. After the first four initial experiments, all if not majority of entrapped air within tubing and other components was considered to be expelled from the system.

The process of purging the circuit of this air in initial experiments presented an opportunity for leakages within the tubing connectors and other joints to be identified and resolved before further testing took place. This ultimately allowed the rig to be calibrated such that successive experiments from that point on would result in a greater degree of expected accuracy, especially considering the likelihood of entrapped air in the circuit to be reduced upon successive testing iterations. Additionally, the gear system is likely to result in greater mechanical efficiency upon successive experiments as the belt begins to heat up and expand becoming more malleable and less prone to slip.

Mean residual and slope deviation metrics calculated for each respective experimental iteration of phase 1 is shown in *Figure 6.4* illustrating the value for both mean residual metric's normalised between the value of **{1,2}** for ease of comparison. Varying of the correction factor was done by applying a factor of **0.5**. Observing the bar data associated with **Exp. 6** of *Figure 6.4*, the lowest combined residual effect was yielded at correction factor value of **0.0007806**. This experiment however, was not able to be completed over the full simulation time due to a leak that became present necessitating the termination and replication of this specific experiment iteration. The experiment was repeated and produced the results shown associated with **Exp. 7**.

Taking note of the effect of this correction factor on the resulting residual metric, it may be concluded that in comparison to the outcomes of **Exp. 8**, a correction factor of **0.0001951** can be considered favourable when observing the optimal fit for the measured coronary volume signal to the associated simulation result. The phase 1 raw experimental data and associated signal comparisons can be referenced in *Appendix C.9.1*.

6.2.2 Phase 2: Physical System Identification and Parameter Estimation

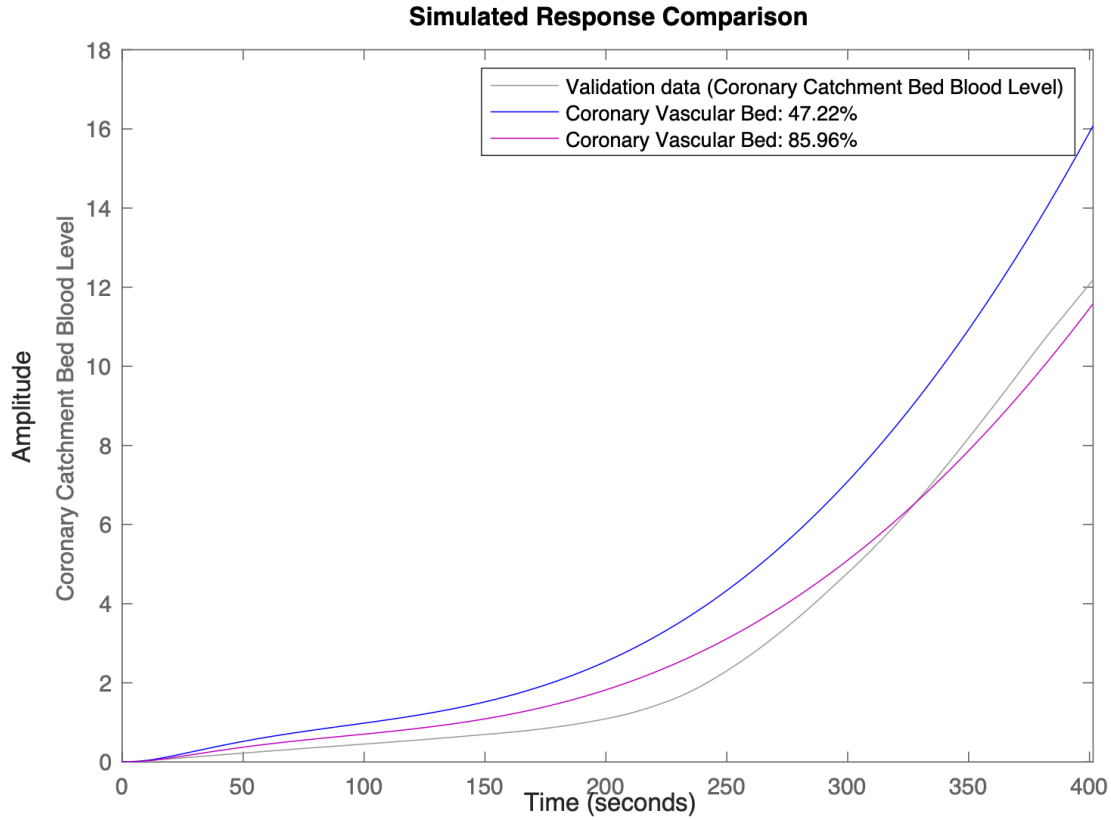

FIGURE 6.6: Parameter Estimation to Measured Data Comparison

The objective of *phase 2* was to apply the *non-linear grey box* presented in *Chapter 5*, by recalibrating the model to estimate coronary volume in reservoir B using the new adjusted value of the correction factor determined in *phase 1*.

Once the model initial estimate was able to produce an estimate within an **85%** degree of similarity, three successive experiments were run independently using identical setup and model parameter initialisations. The aggregate of these experiments was then taken as the validation set to the grey-box model and a set of parameter estimates were generated using using iterative application of the **Trust Region Reflective Newton** algorithm for comparison against a state-space representation of the signal output. This comparative estimation procedure remains consistent with the process followed in *Section 5.6.1*.

This parameter estimation as previously shown makes use of the measured **Coronary Vascular Bed** volume from reservoir B as the dependant variable against which comparison for parameter estimation takes place. Conversion of measured volume data to fluid level was achieved by applying a conversion factor corresponding to the normalised value of the constant cross-sectional area of reservoir B.

An additional experiment was carried out due to the first experimental outcome signal indicating a significant degree of pump cavitation which was visually noticeable during the experiment. The resulting signal indicated unexpected fluid behaviour and produced a sub-optimal first parameter estimate. This was done in an attempt to improve parameter estimation accuracy. The parameter estimation was carried out by using the aggregate of the latter three experiments as the validation set. New estimates were then applied to the simulation and state-space representation after which the estimation procedure was repeated.

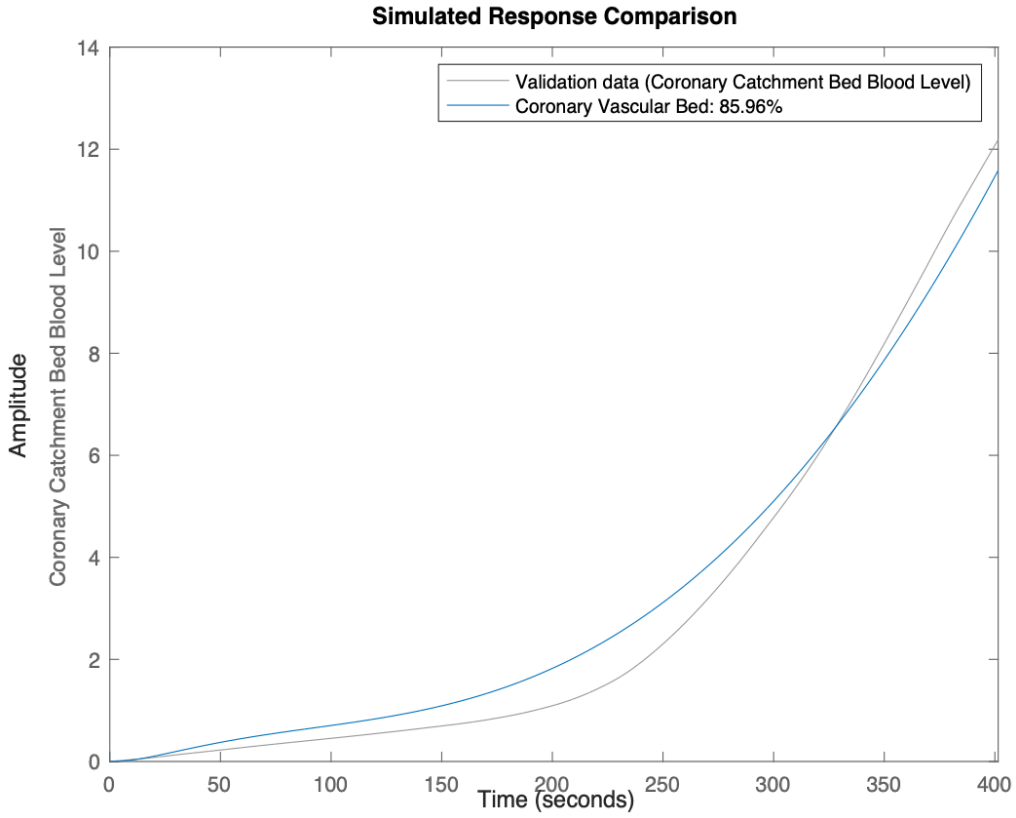

FIGURE 6.7: Estimation Response to Measured Data Comparison

Initial set of estimation parameters when applied to the grey-box model resulted in a signal similarity of **47.22%** illustrated in *Figure 6.6* in purple against the validation set. This signal using the original "best guess" for estimated parameters corresponds to the profile of the generated physical signal shown in **Exp. 8** of *phase 1*.

Successive replication of this estimation procedure resulted in a final parameter set corresponding to an **85.96%** signal similarity. Note, that as in the calibration process in *Chapter 5*, parameters corresponding to gravitational acceleration and fluid density remained fixed while all other parameters were initialised as free for estimation.

6.2.3 Phase 3: Validation

Validation of the estimated set of parameters was then achieved by repeating the experiment with an additional two iterations. Each iteration made use of a new set of *c-value* coefficient parameter estimates. The initial iteration of estimates were determined by fitting the line denoted by *Equation 5.2*, to the line governed by the approximating *theta* parameters produced by the *grey-box model* applied to the final estimated values in *phase 2*. The model simulation was then initialised and run concurrently with the physical flow experiment using the new derived *c-value* parameters for model pump configuration in conjunction with the determined *theta* parameter estimates of the *grey-box model*. Based on the resulting fit of the physical coronary volume signal once again determined via measurement of time-dependant fluid accumulation in reservoir B in relation to the simulated theoretical signal, *c-values* were intuitively tuned based on the magnitude of deviation from the corresponding experiment simulation signal.

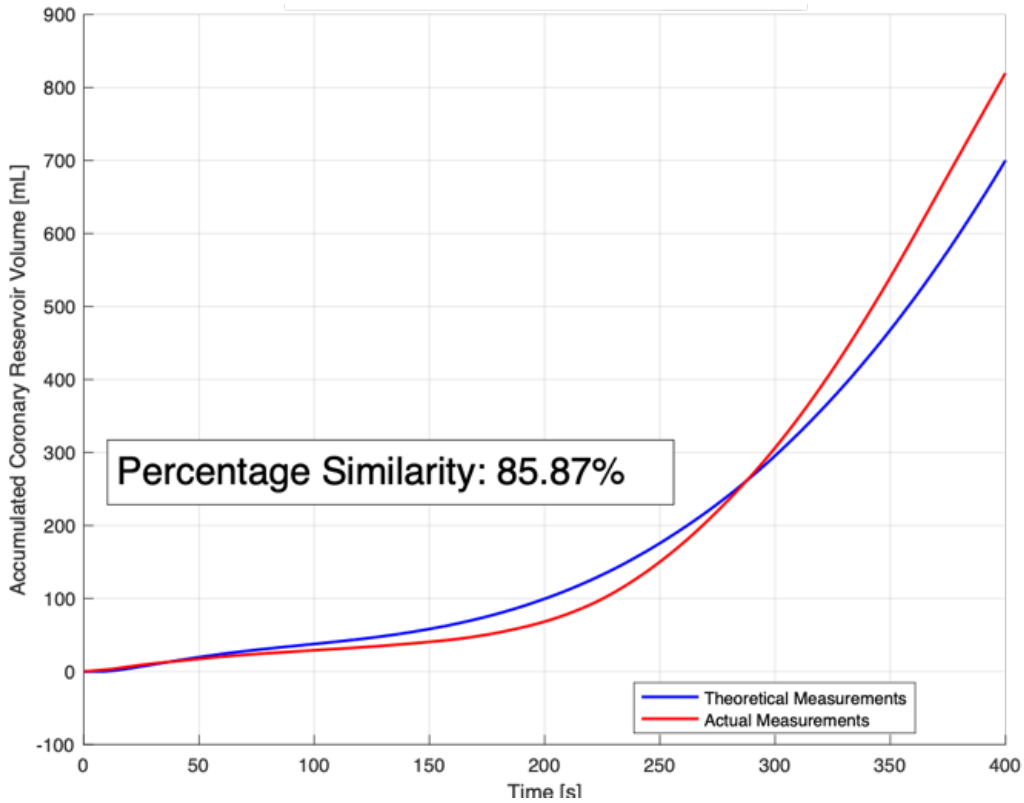

FIGURE 6.8: Validated Simulation Response of Estimated Pump Control Parameters

The second and resultantly final set of *c-values* corresponding to the highest degree of achievable accuracy was deemed to be the optimal solution due to minimal improvement of successive estimates without diverging into a non-feasible solution region *(i.e Solutions not physically possible or parameter values that over constrain the test rig motor-pump complex)*.

The resulting highest degree of achievable accuracy is illustrated alongside the signal comparison in *Figure 6.8* at **85.87%**. The initial and final *c-values* used are shown within *Table 6.1*. All raw data in addition to each set of measured physical and simulated signals can be found in *Appendix C.9.3*.

Model Parameters	Initial Value	Estimated Value #1	Estimated Value #2	Units
k	0.79	0.79	0.79	-
c_0	1.75E+05	1.75E+05	1.51E+05	$Pa{\cdot}m^3/kg$
c_1	-2.92E-07	-2.92E-07	-2.19E-03	$Pa{\cdot}s/kg$
c_2	3.91E+12	3.91E+12	6.91E+12	$Pa{\cdot}s^2/(kg{\cdot}m^3)$
c_3	2.16E+05	2.16E+05	2.16E+05	$Pa{\cdot}s^2/(kg{\cdot}m^3)$

TABLE 6.1: Comparison of Initial and Estimated Approximating Model Pump Coefficients

6.3 Trial 3: Artery Specific Phantom Flow Analysis

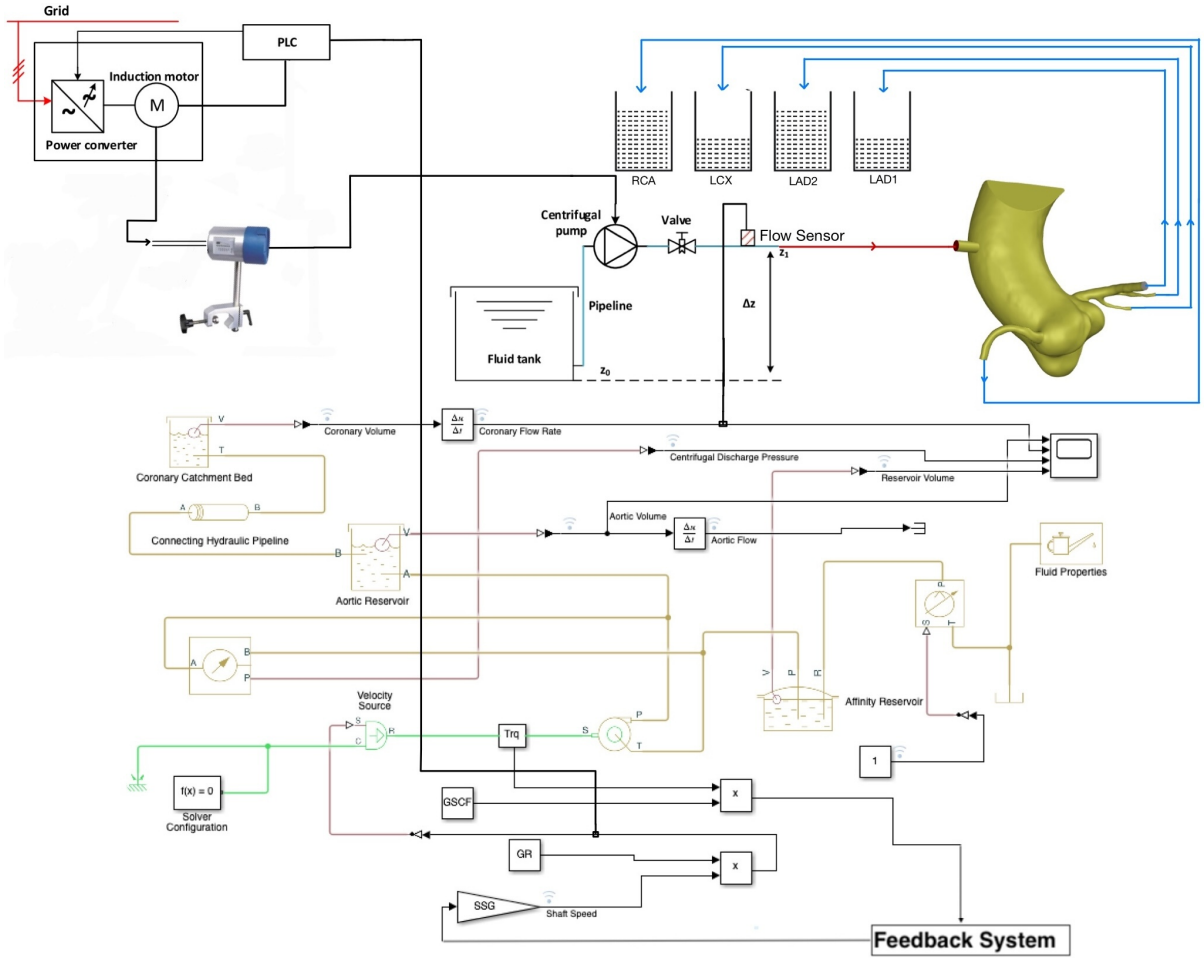

FIGURE 6.9: Trial 3 Simulation and Parallel Bench Testing Circuit Configuration

Dynamic flow testing was carried out in order to relate flow through each of the arteries represented in the physical phantom model, against the result of the computational fluid dynamic approach for flow calculations at the same boundary conditions. Using the simulation model incorporating the validated set of *c-values*, the same control system response simulation was used to produce flow through the each of arteries of the phantom. Flow through each artery was derived based on the time-dependant volume measurement of fluid drained into four separate respective beakers as shown in the diagram of *Figure 6.9*.

Careful consideration was taken to ensure that the height at which the respective tubing of each artery outlet entered each beaker were equal to each other as well as the height of tubing outlets used for connection with reservoir B within the experiments of *trial 2*. This consistency ensures that the correction factor and parameter estimates calculated with respect to the expected fluid level changes at the free surfaces during the simulation remain applicable and thus the model configuration retains its validity.

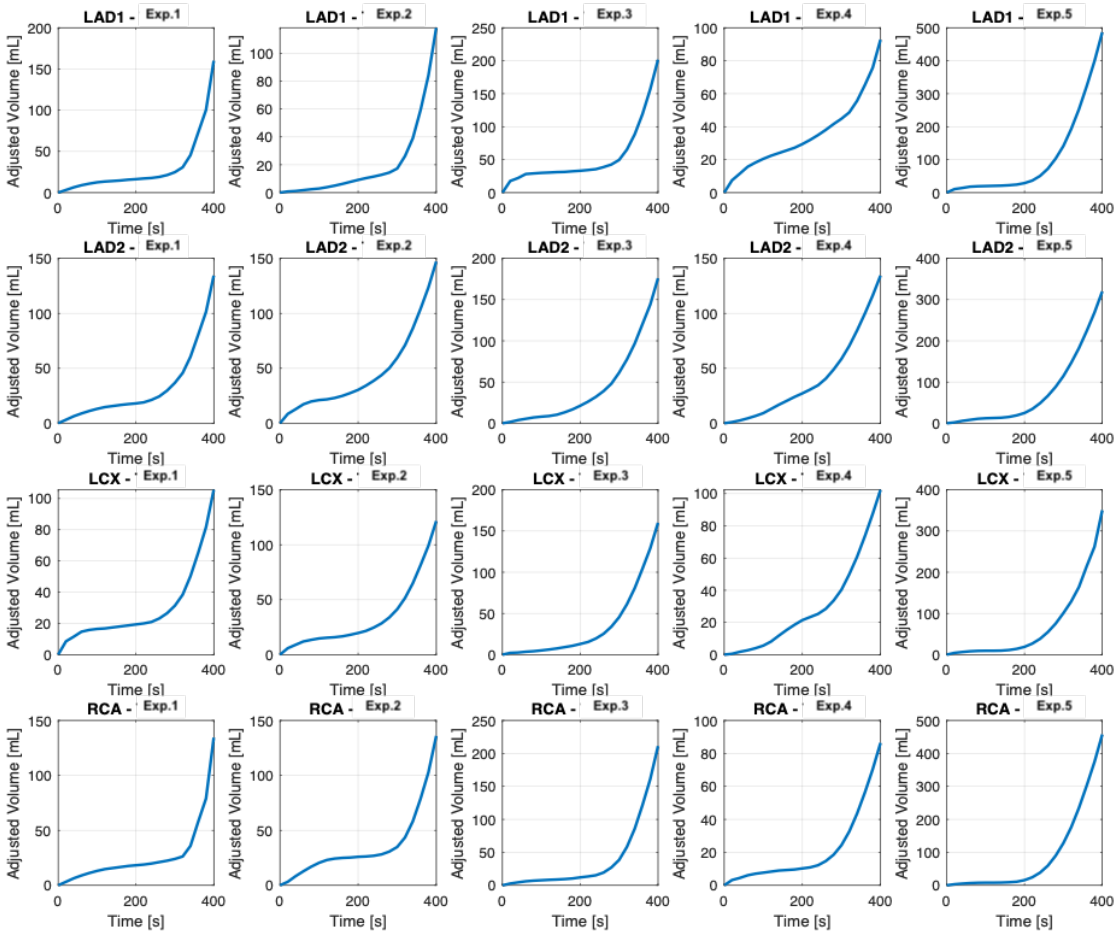

FIGURE 6.10: Accumulated Coronary Volume of each Artery in each Simulation Experiment

Five experimental iterations were completed that resulted in five sets of accumulated volume measurements through each of the phantom arteries. Each experiment was filmed using a camera specifically setup on a static tripod stand at a height chosen to minimise potential for error of parallax. Once each experiment was completed, footage was used to populate the dataset by manually capturing beaker volume measurements at successive **20 second** time-stamp intervals.

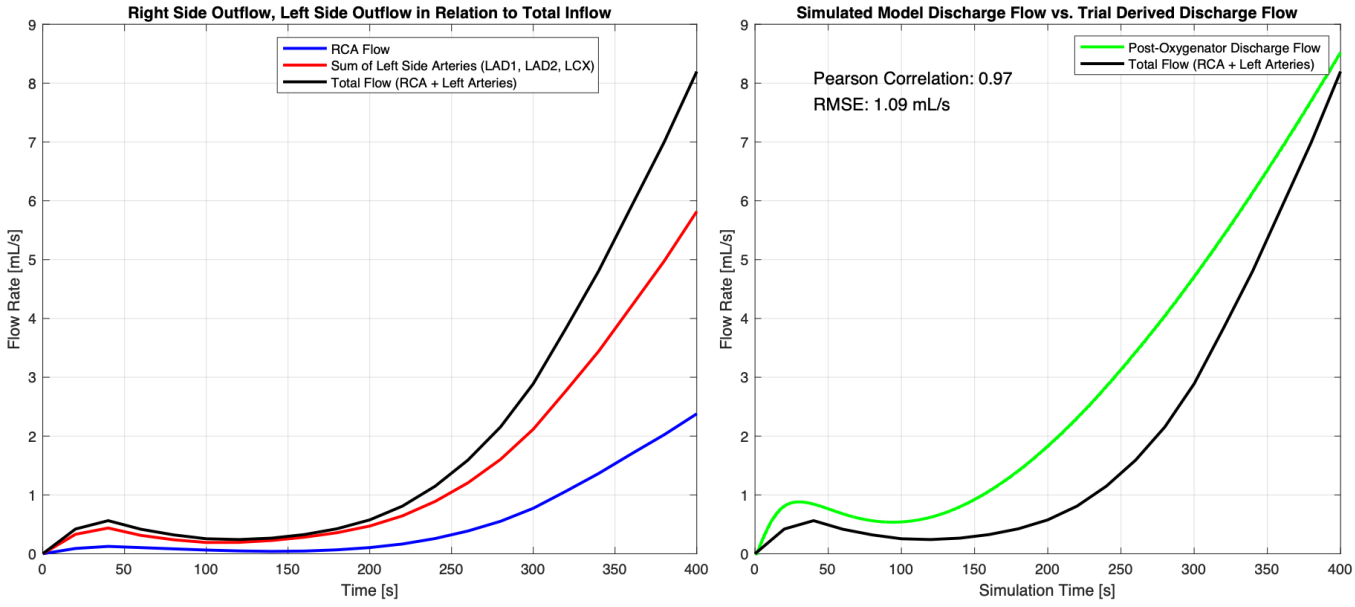

FIGURE 6.11: Right and Left Side Artery Flow Comparison in relation to Simulated Post Oxygenator Discharge Flow

The complete raw dataset can be referenced in *Appendix C.10.1*. Each artery volume signal was then aggregated across all experiments at each time interval. This aggregation process was done in order to reduce the effect of experiment specific flow anomalies and variation thus resulting in a distinct artery specific volume profile. The profile of each artery signal at each experiment iteration is shown in *Figure 6.10*. Taking into account each of the respective artery profiles, the resultant flow was then determined by calculating the associated time derivative. By extension, considering the principle for *Conservation of Mass* in a closed system, an approximated signal for the mean inflow through the cannula was derived according to *Equation 6.8*.

$$Q_{\text{Cannula}} = Q_{\text{LAD1}} + Q_{\text{LAD2}} + Q_{\text{LCX}} + Q_{\text{RCA}} \tag{6.4}$$

Drawing on each of the artery specific flow profiles, it is then of particular interest to observe the proportion of flow through each of the arteries and the subsequent changes in proportion of artery specific flow at each time point during simulation. This has been shown in *Figure 6.12* indicating each artery specific flow proportion in relation to the associated cannula inflow signal and control pressure target signal. It can be seen that at the onset of flow through the phantom, majority of outflow from through the root can predominantly be attributed to **LAD1**. At the onset of the experiment, inflow is relatively low and thus results in minimal accumulated pressure within the root. A larger proportion of flow exiting through the arteries of larger diameter would be expected. Taking note of the proportion signal changes as the simulation proceeds however, shows a change in relative flow proportion occurring at distinct points in time.

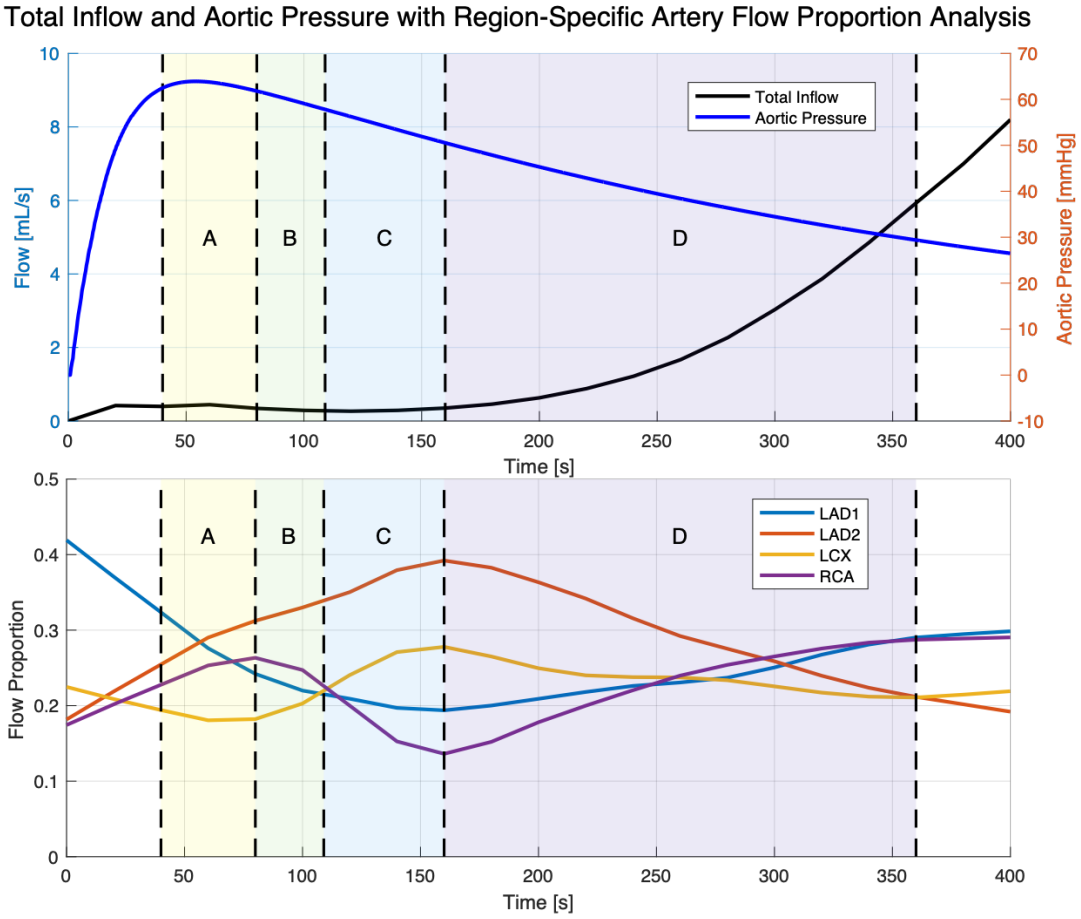

FIGURE 6.12: Phantom Artery Relative Flow Proportion Signals

The first change to discuss is the increase in flow proportion through **RCA**. Interestingly, **RCA** undergoes a linear increase until the point at which inflow magnitude causes a pressure overshoot in the simulation and is controlled back toward the target value of **60 mmHg**. This marks the start of the region marked **A**. We then notice a decline in the rate of flow proportion increase at **RCA** within this region until reaching a local maxima start of region characterised by **B**. The onset of this region can be seen to be in alignment with the change in concavity of the decreasing inflow signal. By extension, we notice that the points at which zero crossings of the first and second order time derivatives of the inflow signal occur, correlate with a sign or concavity change in each of the respective artery proportion signals.

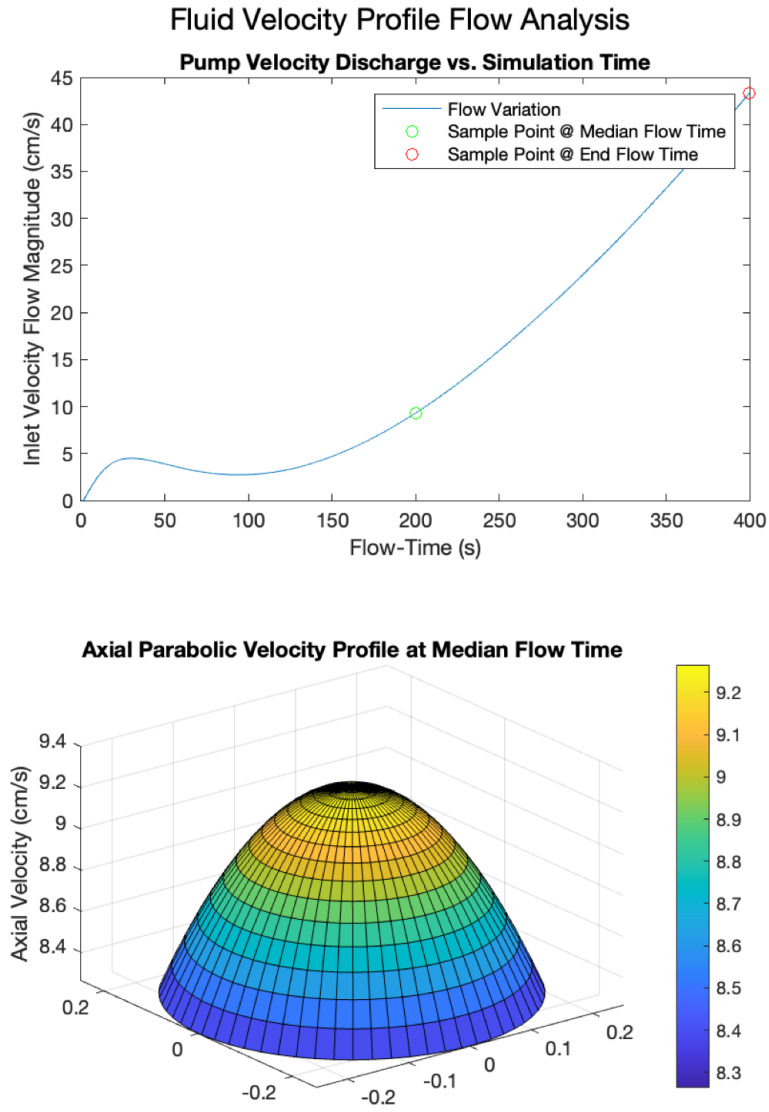

FIGURE 6.13: Developed Parabolic Flow Profile associated with Polynomial Determined to Sample Velocity

RCA and **LCX** resemble second order derivatives of the inflow signal, while **LAD1** and **LAD2** resemble first order derivatives. **RCA** and **LCX** appear to compete for flow and appear inversely proportional to one another. The same principle appears to apply between **LAD1** and **LAD2**. This is evident based on the way in which these signals appear to inversely reflect one another as though mirrored across a hypothetical horizontal axis positioned at the midpoint between the signal pairs. Time points at which each of the region limits have been defined are

t = [40; 80; 109; 160; 360]

for reference. These time points were determined by approximating the zero crossings of the first and second order time derivatives of the inflow signal.

After the first pressure peak, an increase of inflow results in a decrease in relative flow proportion through the largest and smallest arteries respectively **(LAD2, LCX)**, while the inverse occurs through the remaining intermediately sized arteries **(LAD1, RCA)**. At the end of simulation after prolonged inflow, the two larger arteries predominate total outflow. The associated cross-sectional areas of each of the boundary conditions can be found in *Table 6.2*. Furthermore, taking note of the simulated **aortic pressure** signal we notice the changing flow magnitude in relation to simulated rising and falling aortic root pressure within the upper half of *Figure 6.12*.

Observing the changing inflow in response to the simulated pressure changes within the phantom, it remains to be determined, to what extent the observed artery specific flow proportion changes are governed by pressure changes within the phantom root and/or the subsequently developed inflow pattern as function of these pressure changes. As discussed in *Chapter 3*, the decline in aortic root pressure during diastolic relaxation is expected to result in increase coronary blood flow. This is the case however, when ejection from the left ventricle

Table 6.2 Surface Area Measurements of the Inlet and Outlets

Rank	Region	Area (cm^2)
1	Inlet	$1.961E-01$
2	LAD2	$8.420E-02$
3	RCA	$1.551E-02$
4	LAD1	$1.373E-02$
5	LCX	$1.249E-02$

occurs independently of root pressure changes and any positive antegrade flow directly resulting in an in increased root pressure. Assuming in a hypothetical instance that the simulated aortic pressure signal describing the associated root pressure has been simulated and quantified accurately - we take note drawing once again on the signals shown in *Figure 6.12*, flow through all arteries does appear to be directly correlated with an increasing inflow. We may then assume that the predominant factor affecting artery specific flow proportion is the net effect of instantaneous root pressure change in relation to varying cannula inflow.

The orientation and dimensions of each of the arteries in relation to the root and the points at which bifurcation occur has be shown to be one of the main determining factors in flow behaviour according to **Murray's Law** (*See Chapter 2.2.6*). Further analysis of the resultant artery flow behaviour is required to better understand the relationship between the geometric properties of the phantom arteries and the resulting flow patterns observed during the experiments within this trial.

Should there be a potential relationship between the characteristics of the inflow signal during cardiac perfusion and the resultant oxygen delivery to the myocardium through each of the coronary arteries, this would have extensive design implications on the nature of flow delivered from a supporting circulatory apparatus. Considering the inverse relationship between the right major coronary artery and the left circumflex artery, appearing to supposedly compete for flow, there are additional considerations to be made when considering the differing rate of myocardial oxygen consumption delivered to either side of the heart during perfusion. This as discussed previously in *Chapter 2.2.2*, is based on the differing degrees of cellular metabolism dependant on the degree of stroke work achieved through ventricular contraction against differing left and right after-load pressures within the ventricles of a heart in a perfused mid-transplant condition.

6.3.1 CFD Mesh Flow Cross-Comparison

In the case of aortic perfusion where the AV remains shut throughout each successive cardiac cycle due to *Aortic Pressure » Left Ventricular Pressure*, perfusion can thus be considered purely diastolic. This presents the pressure drop and subsequent velocity at the coronary ostia to be a valuable metric for analysis of perfusion related haemodynamics. The flow velocity is thus computed at the plane normal to the mesh boundary condition of each of the arteries.

The optimised polyhedric model presented in *Chapter 4.2.2*, was used to simulate flow with respect to the mean time taken for the control system response presented in *Chapter 3* to reach it's respective **0.2-settling time** in relation to the chosen target value. The cross-comparison of the CFD model simulation data was achieved by contrasting the distribution of flow ranges at the boundary conditions of the mesh with the experimental data measured through the flow phantom using the same input signal.

User-Defined Inlet Profile

The inflow velocity to the cannula region of the flow phantom was determined by calculating the total outflow inferred from the aggregation of artery flow profiles measured during *trial 3* testing. The flow was then used to calculate an approximate signal measurement for discharge velocity applied to the cannula inlet of the phantom. The calculation for the expected discharge velocity was achieved using *Poiseiulle's Law* as follows:

The axial fluid velocity $v(r)$ in a tube as a function of radial distance r can be derived from the volumetric flow rate Q and the radius R of the tube. We assume steady, incompressible, laminar flow (Poiseuille flow), where the velocity profile is parabolic.

Given:

- Q: Volumetric flow rate (cm^3/s)
- R: Radius of the tube (cm)

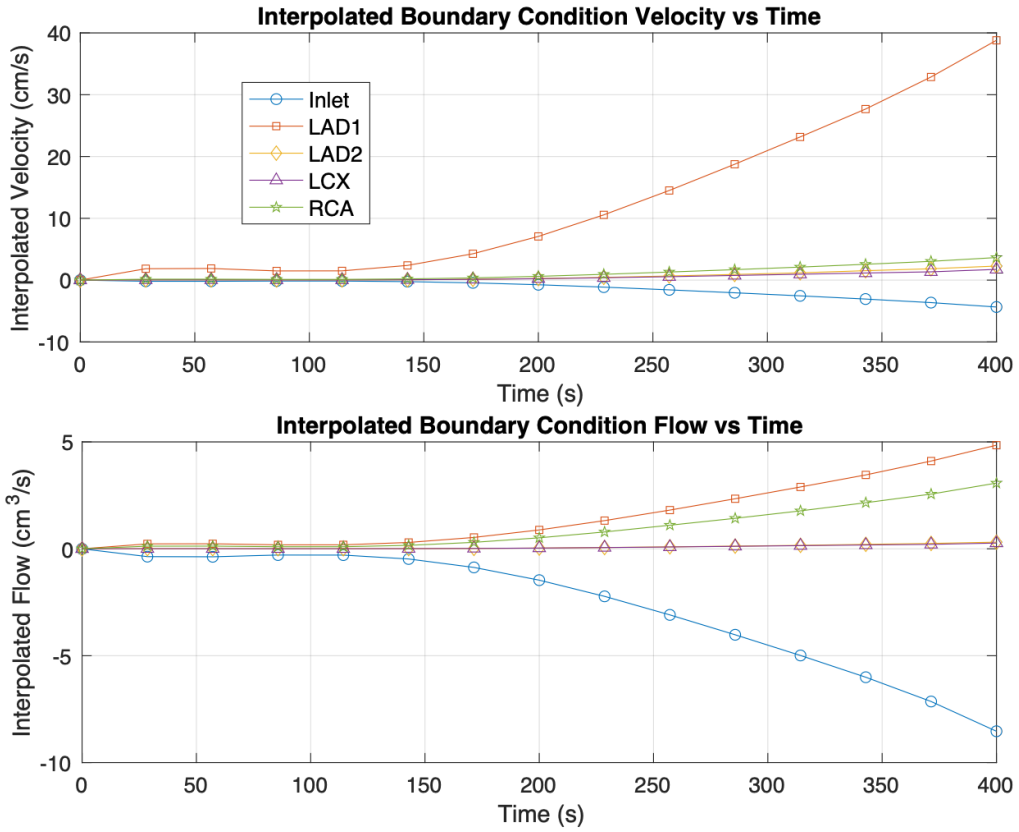

FIGURE 6.14: CFD Simulated Artery Specific Flow Outcome

- r: Radial distance from the center of the tube (m), where $0 \leq r \leq R$
- $v(r)$: Axial velocity at radial position r

The total volumetric flow rate Q through the tube is related to the velocity profile $v(r)$ and the cross-sectional area:

$$Q = \int_0^R v(r)\, 2\pi r\, dr \tag{6.5}$$

This integral sums up the contributions to flow from all infinitesimal annular rings at radius r.

For laminar flow, the velocity profile follows a parabolic distribution. The maximum velocity $v_{\max}$ occurs at the center of the tube $r = 0$, and the velocity at any radial distance r is given by:

$$v(r) = v_{\max}\left(1 - \frac{r^2}{R^2}\right) \tag{6.6}$$

Substituting the velocity profile into the equation for flow rate:

$$Q = \int_0^R v_{\max}\left(1 - \frac{r^2}{R^2}\right) 2\pi r\, dr \tag{6.7}$$

The inlet velocity signal was determined by interpolation of the derived **Discharge Velocity** signal over the simulated time of **400 s** from the corrected model experiment. A function to recreate the flow was determined by fitting coefficients of an *nth* order polynomial through a set of samples points interpolated from the signal measurement. The general form of the equation is as below:

$$f(x) = a_n x^n + a_{n-1} x^{n-1} + a_{n-2} x^{n-2} + \cdots + a_1 x + a_0 \tag{6.8}$$

where:
The coefficients of the polynomial are $a_n, a_{n-1}, a_{n-2}, \ldots, a_1, a_0$, where a_n is the coefficient of x^n and a_0 is the constant term. The degree of the polynomial is n.

Polynomial regression methods for higher order curve fitting were then applied to determine a time-dependent function to characterise the inlet velocity within a finite computational reference frame. The accuracy of the resultant data determined using the polynomial obviously hinges upon the 'goodness of fit' and as such, a polynomial of higher order was prioritised, but also chosen such that the nature of noise and oscillation between data points was minimised.

The function was thus determined to be a 5th order polynomial having the following coefficients:

Degree n	**Coefficient** a_n
5	3.75E-11
4	-4.13E-08
3	1.625E-05
2	-0.002295
1	0.1192
0	0

Applying the inlet velocity function was then achieved by specifying simulated velocity as an axial velocity function normal to the inlet boundary condition of the mesh. In order to simulate a fully developed flow profile as is the case with blood (saline) travelling through a tube at the point at which it enters the root geometry, the fluid at the inlet surface will be of a parabolic shape. The creation of a parabolic flow profile was done in consistency with the work presented in *Chapter 2.3.5*. Residual calculations indicating regions of best polynomial fit are shown in *Appendix C.10.2*.

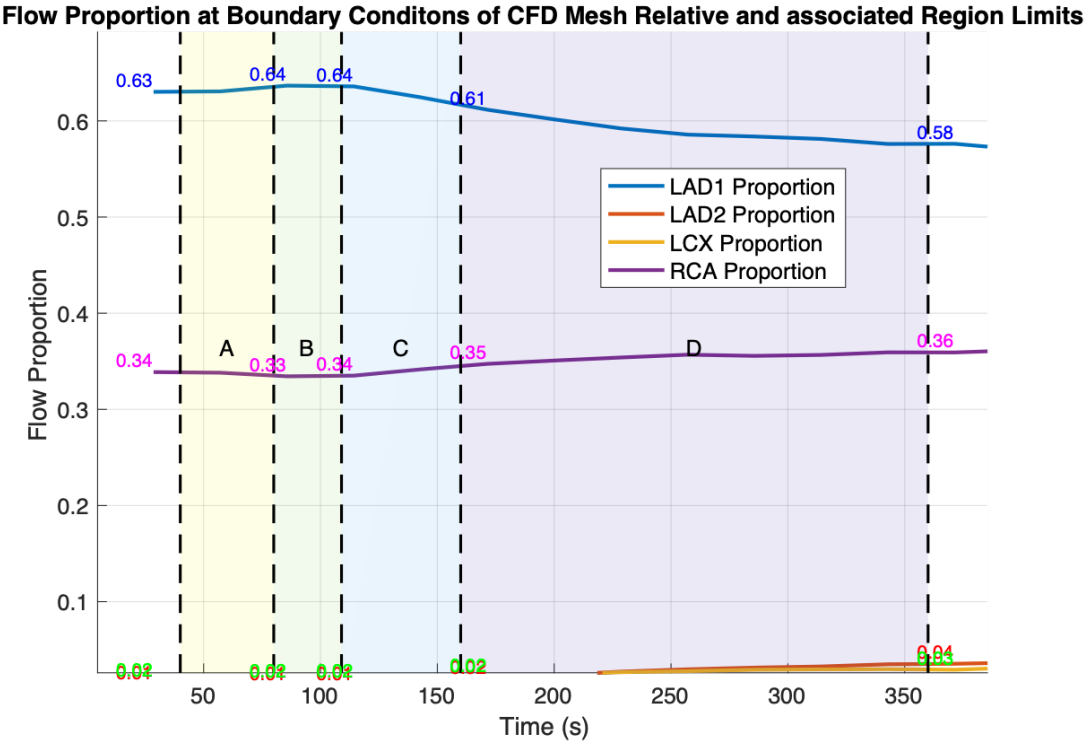

FIGURE 6.15: CFD Artery Relative Flow Proportion Signals

The velocity profile for fluid in a pipe where velocity $v(t, r)$ is a parabolic function of the radial position r and varies with time t and can be denoted by $v_{\max}(t)$ such that:

- $v_{\max}(t)$: The maximum fluid velocity at the center of the pipe as a function of time t.
- R: The radius of the pipe.
- r: The radial distance from the center of the pipe, where $0 \leq r \leq R$.

In this case, the time-dependence of the maximum velocity occurring at the centre of the tube where $r = 0$, is specified as a magnitude characterised by the determined polynomial function.

Then, the velocity profile at a given time t defined at the inlet boundary condition was thus defined using the following form:

$$v(t,r) = v_{\max}(t)\left(1 - \frac{r^2}{R^2}\right)$$

This equation describes parabolically diminishing magnitude of fluid velocity outward from the centre of the tube ($r = 0$) to the walls of the pipe ($r = R$). The remainder of the UDF Function derivation can be found in *Appendix C.10.3*.

The resultant expression was applied through the use of a compiled **C++** script. An example of the application of this function to specify the parabolic fluid surface at a point in time in relation to the discharge velocity signal is illustrated in *Figure 6.13*, where the magnitude of axial velocity at the median simulation time can be seen to be the value of velocity at the centre of the parabolic surface corresponding to the maximum fluid velocity at that time instance. The CFD calculation was formulated by specifying the aforementioned time-dependent parabolic inlet profile in an axial direction positioned as a magnitude normal to the inlet boundary of the mesh model. The simulation was then initialised over the same **400 second** experiment time domain and calculated using **8000** time steps of **0.05** step size and a maximum number of **200** iterations per time step.

6.3.2 Discussion

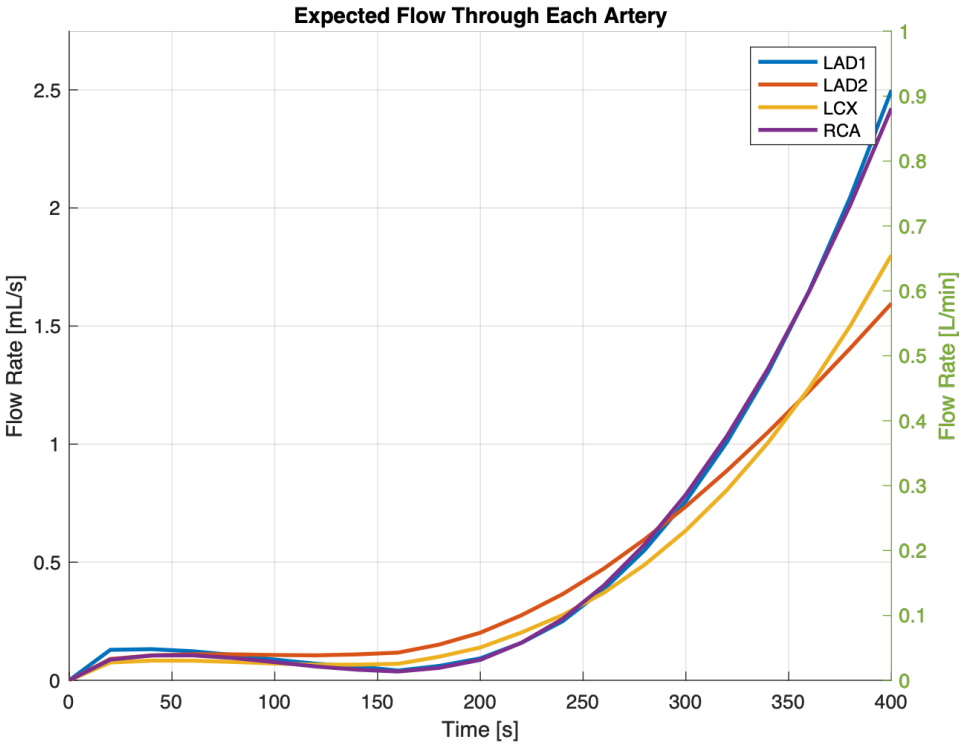

FIGURE 6.16: Aggregated Artery Specific Flow Profile

Drawing on the results of the simulation applied to the computational mesh problem setup, the velocity and flow results measured during the *in-vitro* bench testing experiment in *trial 3* may be compared and used for validation. Firstly, taking note of the signals illustrated in *Figure 6.14*, it can be seen that flow represented by the signal marked blue is in agreement with the flow signal derived from the experimental results using the *Conservation of Mass* principle. This serves to verify the correct application of the inlet polynomial as it relates to the model specific dimensions at the cannula inlet. The representation of the inlet flow signal being negative as determined using the mesh model simply serves to specify the direction of flow as inward to the model in contrast to the flow signals of the outlet boundary conditions shown positive.

Comparing the flow result in *Figure 6.16* showing the outcome of the physical measurements against the mesh flow results shown *Figure 6.14*, there exists a significant deviation in magnitude of flow. It can be see that **LAD1** and **RCA** as calculated by the mesh model indicate approximately twice the value of final flow magnitude at $t = 400s$. Additionally, the final value of flow calculated through **LAD2** and **LCX** at the same time point diverges from the values determined in the experiment by approximately a whole order of magnitude. There are two main theories behind the deviation of the flow magnitudes mentioned.

The first is the effect of tubing outlets connected to each of the phantom arteries entering the respective volume beakers at the same height above the datum. While this was a necessary control variable, it does result in changes of upstream pressure at the phantom coronary ostia. This would be as a result of the hydrostatic pressure at the free surface of the tube outlet and its vertical displacement from the respective artery outlets. While, theoretically using a constant pressure condition uniformly across the outlet boundaries of the mesh problem can be considered analogous to the uniform atmospheric pressure present at the tubing outlets, the impact of effectively normalising the inherent anatomical outlet geometries of the phantom and equalising the resulting pressure head would not surprisingly yield significant flow deviation from what would otherwise be expected.

The second consideration is that of the computational accuracy of the mesh simulation. Due to limitations on the maximum computational complexity of the problem setup, larger time steps were required in order to complete a full simulation across the complete experimental time domain. Using the maximum *cell-convective Courant number* as a metric for simulation accuracy, the final solution presented in this chapter was associated with a maximum value of approximately $4.5E+07$. This is a significantly large result and would be associated with a solution very unlikely to reach convergence upon successive time-step calculations. Therefore, the resulting solution flow magnitude deviation would also be attributed deviation of resulting flow proportion.

Taking note of the flow proportions of the mesh solution shown in *Figure 6.15*, in contrast to the proportions of physical flow through the phantom arteries previously discussed in *Figure 6.12*, it is evident that the deviations observed in flow magnitude throughout the simulation time have a significant impact on the relationship between relative flow proportions of vessels within the mesh solution. However, a vital similarity between the resulting proportions of the two experiments can be identified when noting the seemingly paired flow behaviour of the same vessels shown in *Figure 6.12* as in *Figure 6.15*. It can be seen that the hierarchy of relative flow magnitudes between the two datasets are in agreement. The final settling proportion of **RCA** for instance, results in an absolute deviation of approximately **10 %** from that of the mesh calculated result.

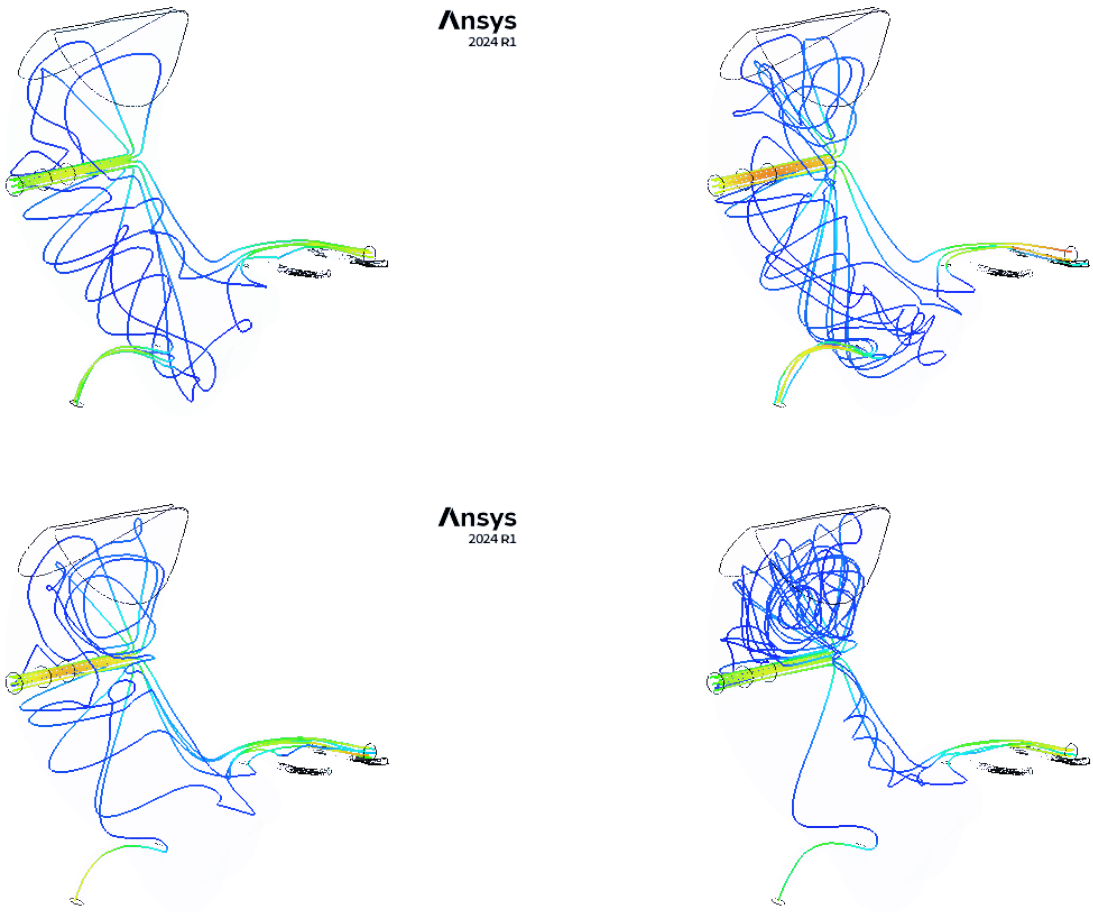

FIGURE 6.17: Particles Streamline Render of CFD Calculated Velocity Vectors at **t(s) = [20, 40, 60, 80]** in chronological order from top left to bottom right

The resultant fluid pathlines within the mesh model at the respective time intervals has been illustrated in *Figure 6.17*. The proportion of red coloured pathlines indicative of higher velocity with regards to flow developed through the inlet can be observed as inlet velocity reaches the first peak in the top right hand image denoted by **t = 40 seconds**. It should be noted that the relative proportion of pathlines through respective vessels changes at each time point.

The change of inlet velocity from **t = 20 seconds** to **t = 80 seconds** results in an expected net reduction of density of pathlines illustrated through **RCA** for example. This is consistent with the reduction of flow proportion through **RCA** seen in *Figure 6.15* where relative proportion drops from **0.34** to **0.33** over the same time interval.

6.4 Summary of Investigation and Key Findings

(a) The effect of a hollow fibre membrane oxygenator used within steady-state circuit testing was shown to induce a complex impedance exhibiting what can be considered an inductive effect on resulting fluid flow with the test rig circuit.

(b) By confirming flow behaviour through the root geometry by validating the mesh model, applications of the mesh simulation allow for the observation of inlet profile dependent affect on the TPG_{ACo} (*See Chapter 3.2.4*). Based on the available data, the effect of inlet flow variation on the degree of myocardial oxygen delivery with respect to perfusion time during transplant may potentially be investigated drawing on the methodology for testing presented in *trial 3* of this chapter.

(c) There exists a marginal deviation of the coronary volume signal from the validated simulation model in comparison to the measured result. The factors believed to have the largest degree of impact on the solution are those modelled and thus estimated by the grey box model. Should additional parameters and factors governing the physics of flow through the test rig circuit be implemented into the parameter estimation procedure, a larger degree of dynamic accuracy may be achieved. This is an important consideration if the simulation model were to be used in a software device capacity and/or cases where large degrees of accuracy are of distinct priority. In the case of simulation model development and by extension the confirmation of parameter dependent signal relationships by way of test rig validation, the observed margin of error serves to adequately characterise the fluid flow behaviour in the circuit and show that the simulation model is able to accurately quantify the relationship between coronary blood flow delivery in relation to control system dynamic pressure response targeting. This was the main objective of the simulation model development and subsequent parameter estimation, because building on this validated platform for simulation, informed future design considerations may be made by expanding on the development of the developed testing rig. This development process is made robust by the ability to simulate different perfusion scenarios using a parameterised simulation model e.x *Cases of Hyperemia (Elevated Heart Rate), Hypertension (Elevated Blood Pressures)*. In this way the simulation landscape developed lends itself to a more versatile and robust process of future solution system development.

(d) By aggregating the profiles of volume accumulation through each of the phantom model arteries during testing, the expected flow profile was determined for each artery and used to derive an expected aggregate inflow signal to the phantom. This signal allowed for a comparative assessment against the post-oxygenator discharge flow signal produced by the simulation model.

(e) The proportion of flow exiting through **LCX** and **RCA** was shown to behave as a second order time derivative with respect to the inflow signal during simulation. Similarly, the proportion of flow exiting through **LAD1** and **LAD2** exhibited first order time derivative behaviour in relation to the inflow signal.

(f) Each pair of arteries exhibiting the same type of differential flow behaviour were identified to be inversely proportional and appear to be *horizontal axis* reflections of one another.

(g) The expected discharge velocity signal was derived by applying *Poiseuille's Law* to the inflow signal based on the dimensions of the phantom cannula inlet. A higher order polynomial characterisation was used to formulate a user-defined function for the parallel CFD application of flow at the inlet boundary condition.

Chapter 7

Conclusions and Future Work

7.1 Future Design Considerations

Based on observations made specifically during the design, development and verification of the *in-vitro* testing rig, it became evident that high system sensitivity is a vital consideration to be made at every level of the design process. This became evident when observing large differences present in the hydraulic fluid behaviour of individual trials in relation micro-air embolisms or very fine leakages. Small differences had resounding subsequent impact particularly noticeable in initial trials discussed within *phase 1* of the dynamic flow testing. The ability to effectively and efficiently purge the circuit of all air would be a vital design consideration for the solution system particularly when considering the impact that these embolisms can have. Furthermore, maintenance of a constant beating heart requires the timely initiation and cessation of perfusion meaning that connection/disconnection of elements within the circuit create potential for instantaneous pressure losses in addition to air infiltration.

Another very necessary consideration made relevant by the high-risk nature of transplant procedure and the inherent need for precise highly accurate flow control is the implementation of correct sensors. Due to the system relying on sensor feedback, the accuracy and efficacy of flow control is completely dependent on the preservation of sensor signal quality. The use of ultrasonic piezoelectric based flow sensors has shown high levels of flow accuracy, however an essential consideration is the requirements that these sensors have for adequate calibration. Choosing and incorporating the correct sensors within the solution system is largely dependent on the resolution of measured signals particularly at very low magnitudes of flow or pressure.

Effective pump control is heavily influenced by the instantaneous calculation of feedback error. Signal latency determines the frequency of feedback response and ultimately determines the effective mechanical and electrical time constants yield the plant transfer function. Minimising latency and prioritising components both electrical and mechanical that are highly responsive to changing input inherently reduce the overarching dampening factor of the plant transfer function. This reinforces the ability of designing and developing a system that can achieve left half plane stability.

7.1.1 PID Control Optimisation

Parameter configurations of the continuous time PID based pressure control of the test rig have large implications on both the efficacy of time-dependent pressure control response as well as efficiency when applied to pump control of the test rig in a trial setting. However, due to the emphasis of the trial procedure being on the verification and validation of flow characteristics and model parameter dependent flow profiles, a slower rate of control response allowed for longer simulation time which was advantageous from the perspective of creating a larger dataset. Additionally, the slower rate of inflow change allowed for more accurate measurements to be achieved and also lead to a greater degree of flow stability in during trials. This flow stability allowed for better control over factors such as pump cavitation and spontaneous appearances of leak and micro-air embolisms which would have otherwise resulted in less accurate flow behaviour and resulting data. From this perspective, relaxation of PID control response was a necessary consideration when considering the aim of the trial procedure to be on the analysis of circuit and simulation dependent flow and not the efficacy of time response which was already investigated in relation to varying flow modalities and applied disturbances in *Chapter 3.4*.

The main purpose of PID control implementation into the model design was however to increase time-dependent pressure control response with a focus on eliminating the need for manual intervention. However, after applying the correcting factors and validation procedure detailed in the preceding chapter there are new and very necessary implications on control configuration that must be considered when designing model control for it's main and originally ideated purpose. Having the *in-silico* simulation now accurately representing the flow dynamics of a real world fluid flow case, the parameters governing control efficacy can be tuned and optimised so as to improve control efficacy without violating the maximum operating point of flow within an actual circuit. In this way the true feasible

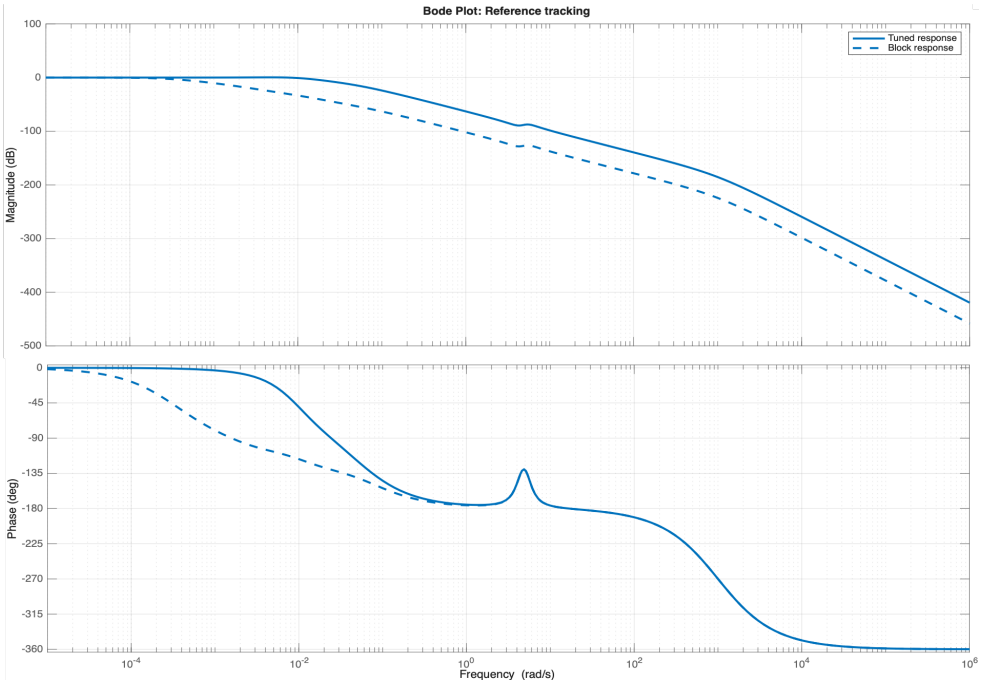

FIGURE 7.1: Phase and Magnitude Bode Plot of Tuned vs Untuned Pressure Control Response

region for a control solution can be explored from the perspective of real world flow delivery based on the materials and equipment standardised for cardiac perfusion.

Compensator Formula for PID Control

The compensator formula for a PID controller in Simulink can be written as:

$$C(s) = K_p \left(1 + \frac{1}{T_i s} + T_d s\right)$$

where:

- K_p is the proportional gain,
- K_i is the integral gain,
- K_d is the derivative gain,
- s is the Laplace variable,
- $T_i = \frac{K_p}{K_i}$ is the integral time constant,
- $T_d = \frac{K_d}{K_p}$ is the derivative time constant.

7.1.2 Response Tuning

The parameters used for control configuration during trialling were determined experimentally based on the maximum permissible load placed on the test rig and the duration with which this load could be maintained without become unstable. Through further experimental variation of control parameters through simulation, tuned control parameters were established which can be found alongside the original relaxed control parameter in *Table 7.1*.

Table 7.1 PID Controller Gain Comparison

Gain	Tuned	Untuned
K_p	147.7356	2.9076
K_i	2.5709	0.045906
K_d	-4974.9562	-255.6249
N	0.029696	0.011375

The improved dynamic system response performance from the perspective of Gain and Phase margin changes in relation to the un-tuned system has been illustrated by a bode plot *Figure 9.1*.

Table 7.2 System Performance Comparison

Response KPI	**Tuned**	**Untuned**
Rise time	132 seconds	6.75E+03 seconds
Settling time	591 seconds	1.21E+04 seconds
Overshoot	6.98 %	0 %
Peak	1.07	0.999
Gain margin	108 dB @ 16.7 rad/s	147 dB @ 16.6 rad/s
Phase margin	70.5 deg @ 0.011 rad/s	87.6 deg @ 0.000312 rad/s
Closed-loop stability	Stable	Stable

The functional result on perfusion performance is illustrated in *Figure 7.2* showing a normalised comparison between the resultant Aortic Pressure signal in relation to the variable control of the tuned and un-tuned motor signals used to vary pump discharge pressure. The associated key performance indicators of the two contrasted control configurations have been compared in *Table 7.2*.

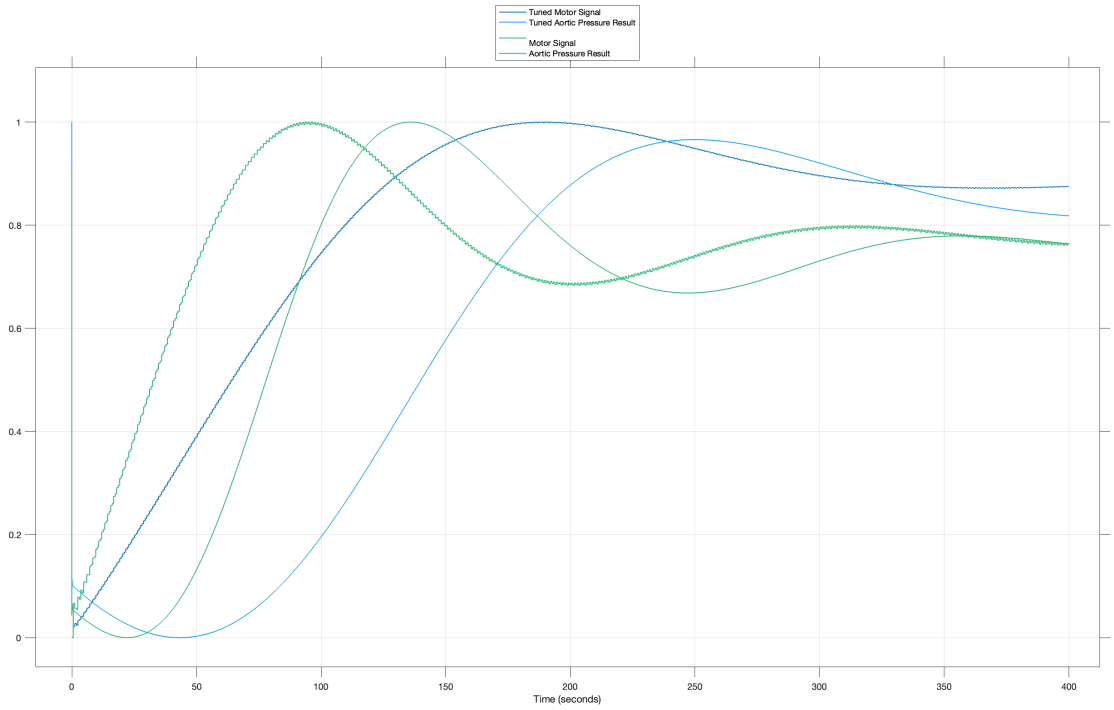

FIGURE 7.2: Tuned versus Non-Tuned Continuous Motor Signal and Subsequent Aortic Output Pressure Result

It can be seen that the result of optimal control parameter tuning can yield a significantly different degree of response efficiency. This is well justified when considering the difference between a **591 second** settling time in relation to **1.21E+04 seconds** of the tune and non-tuned systems respectively. The potential impact this may have on optimal perfusion function it becomes clear when considering the efficacy of organ preservation in relation to reaching a steady target pressure **3.2 hrs** sooner. This is obviously a performance improvement skewed by the inherently slow intended response of the un-tuned original system. However, the improvement in efficacy does establish a good precedent for improved future optimisation with a focus on optimal perfusion delivery and response. By using more robust methods for system transfer function derivation, further large response improvements are very achievable. By running perfusion trial testing as in *Chapter 6*, in parallel with control optimisation iterations, there can be a significantly higher degree of functionality achieved in future design iterations.

7.1.3 Resistance and Pressure Drop Correction for Coronary Vasculature

By applying the principle of flow division proportional to the area at the boundary surface normal to each of the respective coronary ostia according to **Murray's Law**, applying weighting factors to each of the coronary outlet sub-blocks within resistance block **R3** there may also be a significantly improved degree of simulation accuracy.

This approach lends itself well toward a more immediate effort to achieve improved simulation accuracy. These weighting factors can be derived by calculating the cross-sectional area-ratio of the surface planes normal to each of the respective coronary ostia within the CHD model.

7.1.4 Transient Transfer Function Derivation

By conducting **Pulse Image Velocimetry** testing to further validate and increase accuracy of CFD calculations using the root mesh model, the coefficient of loss and the inherent velocity transfer function for each of the outlet boundary conditions may be determined as a function of the delivered cannula inflow. This allows for better approximation of the complex impedance exhibited by the root such that it may be incorporated into the simulation model as its own block as illustrated in *Figure 7.3*. By applying this transfer function as a control block in the Laplace domain, we may preliminarily assess coupled model simulation and make necessary scaling corrections before coupling operation of both models for parallel real time simulation.

Additionally, by better understanding the haemodynamics of blood in the root subject to cannula inflow in relation to cannula placement, there exists the potential to optimise cannula placement such that the delivered flow through the cannula in a specific location and orientation may serve to better perfuse the coronary vascular beds by working in conjunction with system control logic that leverages the expected flow behaviour associated with a specific type of cannulation. This may serve to be a particularly effective solution when considering the efficacy of antegrade vs retrograde cannulation used in a host of varying surgical procedures over and above just bypass.

7.1.5 Innovation of Physical Feedback Flow Coupling

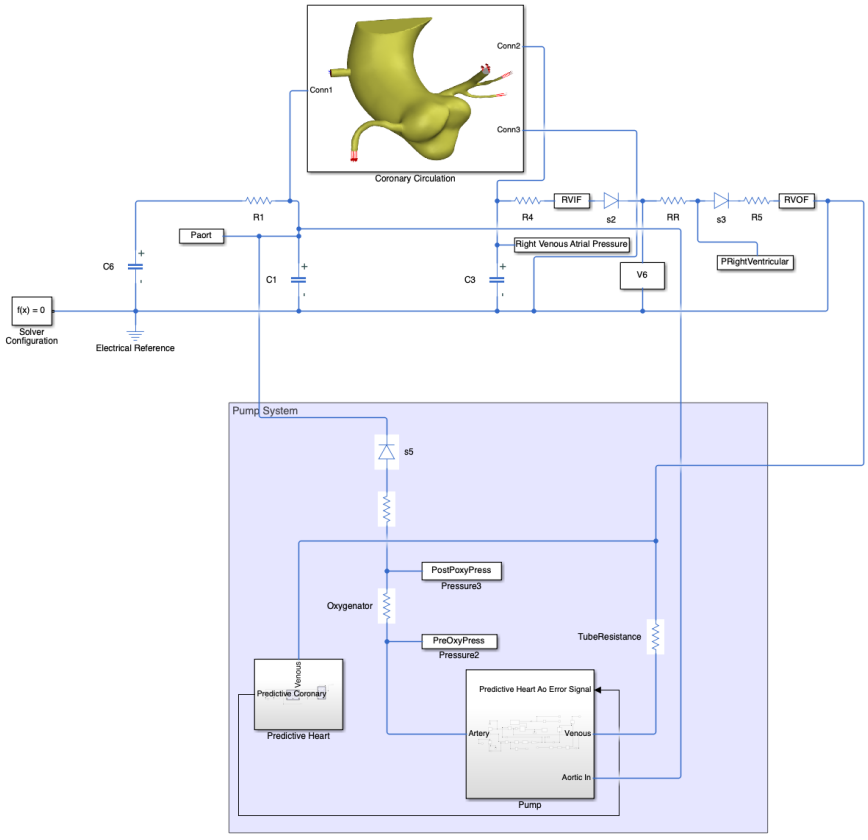

FIGURE 7.3: CHD and LPM Model Subsystem Coupling

By compiling and deploying the optimised simulation model incorporating improved control response and digital CFD feedback calculations, the implementation of this new control logic in a system developed to provide live physical feedback, there exists the potential to incorporate a large degree of added functionality to a potential perfusion device. One challenge faced by surgeons during the transplantation procedure is the vertical displacement of the heart during ongoing perfusion and the altered pressure and flow as a result of hydrostatic fluid pressure changes at free surfaces of the perfusate. Improved efficacy and rate of response in varying discharge as well as higher rates of

control side signal calculation serve to potentially provide an effective solution to this as well as many of the other similar challenges posed during transplantation of a continuously beating heart.

7.1.6 Pressure Gradient Feedback Targeting

By reconfiguring control logic based on the feedback of live sensor data, instead of absolute root pressure being used as a manual user input fixed target, the measure for endocardial viability and the associated algorithm for its calculation presented in *Chapter 3*, may allow for system control to be determined based on the dynamically varying requirement for a pressure gradient developed across the aortic root such that coronary flow is optimised. This relies on constant tracking of cardiac action potential using hardware such as a pacemaker and other specialised sensor components. The integration of these signals toward this feedback logic is detailed as a UML diagram illustrated in *Figure 7.4*.

Coupled Feedback Control Logic

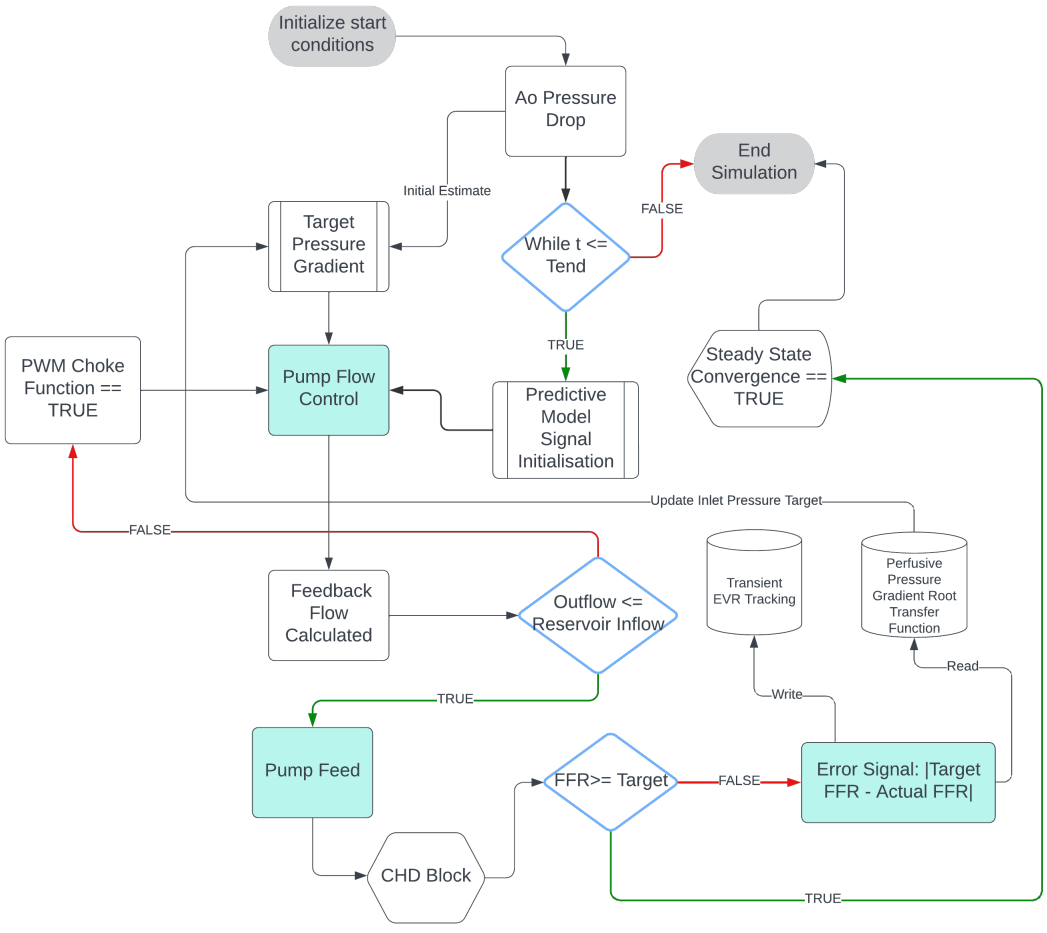

FIGURE 7.4: UML Global System Control Process Algorithm

Throughout the process undertaken during design and development, numerous obstacles and challenges were encountered. The observation of these obstacles does however serve to better inform the design process of the posited solution system. The realisation of the factors potentially impeding the innovation of this solution system was however one of the intended outcomes of this study.

Based on observations made during specifically the design, development and verification of the *in-vitro* testing rig, it became evident that high system sensitivity is a vital consideration to be made at every level of the design process. This was noted when observing the large differences present in the hydraulic fluid behaviour of individual trials in relation micro-air embolisms or very fine leakages. Small differences had a resounding impact, particularly noticeable in initial trials discussed within *phase 1* of the dynamic flow testing. The ability to effectively and efficiently purge the circuit of all air would be a vital design consideration for the solution system particularly when considering the impact that these embolisms can have. Furthermore, maintenance of a constantly beating heart requires the

timely initiating and cessation of perfusion, meaning that at some stage elements connection/disconnection of the hydraulic circuit exposes it to the risk of instantaneous pressure losses and air infiltration.

Another very necessary consideration made relevant by the high-risk nature of transplant procedure and the inherent need for precise highly accurate flow control is the implementation of correct sensors. Due to the system relying on sensor feedback, the accuracy and efficacy of flow control is completely dependent on the preservation of sensor signal quality. The use of ultrasonic piezoelectric based flow sensors has shown high levels of flow accuracy, however an essential consideration is the requirements that these sensors have for adequate calibration. Choosing and incorporating the correct sensors within the solution system is largely dependent on the resolution of measured signals particularly at very low magnitudes of flow or pressure.

Effective pump control is heavily influenced by the instantaneous calculation of feedback error. Signal latency determines the frequency of feedback response and ultimately determines the effective mechanical and electrical time constants yielding the transfer function of the *"plant"*. Minimising latency and prioritising components both electrical and mechanical that are highly responsive to changing input inherently reduce the overarching dampening factor of the plant transfer function. This creates a greater margin under which the designed system may tuned to exhibit left half plane dynamic stability.

7.1.7 Motor-Pump Complex

Technical design considerations as related to the testing rig included the design and implementation of a step-down gearing system and belt tensioner used to ensure that the motor could achieve desired torque of the driven shaft while also operating within the optimal speed range of the controller without overloading the current draw. The belt and gearing system allowed for the inclusion of the hand crank in the event of motor fault/failure. The redesign and use of a non-direct method for shaft coupling would allow for the utility of an emergency hand crank to be quickly introduced in order to restore/maintain flow if needed in the case of high-risk trial testing which may be a necessary future consideration.

Digital to analog conversion allowed for the use of high-resolution signal transmission from simulation to controller with minimal data loss. As opposed to being limited to only eight speed settings as specified by the digital input specifications to the controller the use of a digital signal for control side calculation vastly improved the total control resolution of the system while the real time execution of analog control commands lends itself better to the operation of a motor in parallel with simulation as was the case of the test rig. Current DAC speed of bit conversion output however may have potential limitations when higher degrees of responsiveness may be required. The total analog command resolution was still limited between **0-5V** which may introduce future limitations when considering design for the use of a single power source.

7.2 Future Market Application and Commercialisation

7.2.1 Economic Impact of Heart Failure

The economic impact of cardiovascular disease is associated with the costs of hospitalisation, intervention and treatment. The impact and societal burden of a population hindered by the impact of cardiovascular diseases are thus considered quite significant and a primary concern of the WHO (Mathers, Lopez, and Murray, 2006).

Cardiovascular disease has been identified as the number one cause of death globally. In **2010** costs associated with *CVD's* cost the **US $ 108 Billion** per annum (Cook et al., 2014). This contributes to an overall productivity loss and must be accounted for when considering the economic impact of such illnesses. Ongoing treatment and rehabilitation remains the reality for most patients having suffered from some or other cardiovascular related pathology at both an acute and chronic level. This results in longer term financial commitment to healthcare costs.

TABLE 7.3: Transplant Specific Market Overview (Market Research Future, 2018)

Parameter	Value
Market Size 2022	USD 10.2 Billion
Market Size 2023	USD 11.2 Billion
Market Size 2032	USD 24.3 Billion
Compound Annual Growth Rate (CAGR) (2023-2032)	10.10%
Base Year	2022
Market Forecast Period	2023-2032
Historical Data	2018-2022

Table 7.3 (continued)

Parameter	Value
Market Forecast Units	Value (USD Billion)
Report Coverage	Revenue Forecast, Market Competitive Landscape, Growth Factors, and Trends
Segments Covered	Type, End User, and Region
Geographies Covered	North America, Europe, Asia Pacific, and the Rest of the World
Countries Covered	The U.S., Canada, Germany, France, U.K, Italy, Spain, China, Japan, India, Australia, South Korea, and Brazil
Key Companies Profiled	Apaxis Medical, Inc., CardiacAssist Inc., SynCardia Systems, LLC, Optum Inc., CARMAT, HeartWare International Inc., Thoratec Corporation, and Calon Cardio
Key Market Opportunities	Increasing demand for quality devices in healthcare
Key Market Dynamics	Increasing number of patients suffering from cardiovascular diseases and rise in the geriatric population

A study in **2012** including **197** countries that span **98.7%** of the world's population - the direct, indirect and total costs of heart failure were calculated to be **$ 65 Million**, **$ 43 Billion** and **$ 108 Million** respectively (Cook et al., 2014).

7.2.2 Regulatory Consideration

Taking into account the FDA classification for a medical device, and observing the classifications of existing solutions in the field of myocardial preservation and organ perfusion, it can be determined that the potential solution device/system would be classified as a high-risk device because of the potential for outcomes associated with insufficient organ preservation and corresponding tissue death. By extension this would have strong detrimental effects on the outcome of transplant procedures and may likely result in patient death. This system thus falls within the category of cardiovascular devices and can be subcategorised as a "Circulatory Support Device/Peripheral Interventional Device".

7.2.3 Utility of Developed Simulation Landscape

The multi-faceted approach to transplant specific perfusion modelling and simulation achieved by the outcomes of this study open up several avenues for its utility. The *in-silico* model creates an environment in which various physiological conditions and of the transplanted organ and resulting scenario can be investigated. By analysing the different modalities of pump flow and different control tuning configurations, the software logic aspect of the solution system can be iteratively tested and optimised for function.

The combination of both a computational fluid dynamic approach as well as a lumped-parameter approach to the modelling of perfusion through aortic root cannulation in a cross-clamped aortic root geometry to the best knowledge of the author at the time does not exist in publicly available literature. As discussed in *Section 7.1.5*, the combination of both simulation modalities would allow for the robust modelling of macro circuit blood flow while also allowing for a high level of simulation precision at a more micro coronary specific level. An advantage of the use of a lumped parameter approach especially when applied to global system circuit dynamics is the scalable and ubiquitous nature of its variables and the configurations in which they are used. The potential for investigation of a solution system on both this macro and micro level would comprehensively inform the design process by allowing for the qualification of functional and design variations based on their downstream impact on theoretical coronary blood flow and thus theoretical myocardial oxygen delivery.

In addition, the presence of an *in-vitro* testing model able to facilitate and execute validated hydraulic signals in parallel with the simulation environment allow for the investigation and analysis of solution system function as it relates to real world materials and components. Furthermore, the use of standardised perfusion tubing, reservoirs, luer-locking and magnetically levitated impeller based pumping consistent with materials and products found in a clinical perfusion setting fortify the the test rig's utility for the investigation of a solution device specific to the transplant use-case.

7.2.4 Implications for Development in Context of the South African Healthcare Industry

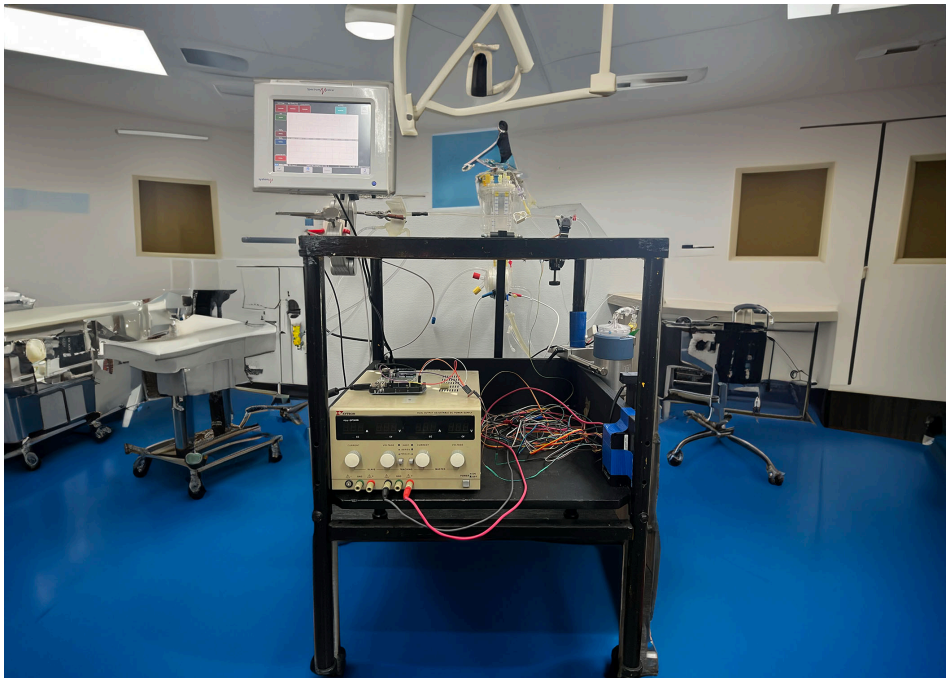

FIGURE 7.5: Developed *In-Vitro* Testing Rig - Solution System *Prototype 0*

The aforementioned utility of the developed foundation for future device innovation creates a starting point for a potential future solution system. Such a system would have far reaching benefits if successfully produced, developed and launched within the South African healthcare space. However, many of the barriers that may potentially prevent the successful adoption of such a device in South Africa would likely originate from the need to produce a solution that accounts for the nation's specific infrastructures (specifically as related to travel and transportation). The economic viability of such a venture necessitates the scale on which it would be manufactured and sold. Innovating a solution that is then effective in facing the challenges of national heart transplantation therefore depends on the ability to produce a solution system aimed at serving the South African population as needed and within the limitations of national healthcare policy, while being able to withstand the constraints of local economy.

7.3 Closing Remarks

Considering the documented development of the perfusion device design and associated simulation landscape, it can be concluded that the inflow waveform into the aortic root as developed by the device control feedback directly effects the flow developed through the connecting coronary arteries. The present limitation of testing under the constraints of rigid-wall haemodynamics limits the accuracy of measured flows through the phantom arteries however. This limitation applies both to the CFD resultant data as well as the physical flow measurements. In reality, the presence of geometrical changes of the root and surrounding vessels deform as a function of the degree of structural compliance encountered by the anatomy under developing pressures. A rigid-walled structure will rapidly increase in pressure, whereas a compliant structure will naturally deform subject to increasing stresses and strains causing an extended period of time in which the target root pressure may be achieved.

A future recommendation of this work is to re-create the experimental setup using a non-rigid body phantom in conjunction with non-rigid body CFD assumptions in order better approximate the inherent time-delay encountered when simulating the achievement of a chosen target pressure. This time-delay may then be used in accordance with the process followed for control tuning and performance optimisation of the embedded control function. By following this process, future design iterations may include a dynamic system-state response better suited toward achieving and maintaining the required flow parameters to an *in-transit* heart.

Bibliography

Alomari, Mohammad et al. (2022). "Is the Organ Care System (OCS) Still the First Choice With Emerging New Strategies for Donation After Circulatory Death (DCD) in Heart Transplant?" In: *Cureus* 14.6.

Appelt, Hannah et al. (2020). "Factors associated with hemolysis during extracorporeal membrane oxygenation (ECMO)—Comparison of VA-versus VV ECMO". In: *PLoS One* 15.1, e0227793.

Ardehali, Abbas et al. (2015). "Ex-vivo perfusion of donor hearts for human heart transplantation (PROCEED II): a prospective, open-label, multicentre, randomised non-inferiority trial". In: *The Lancet* 385.9987, pp. 2577–2584.

Avanzolini, Guido et al. (1988). "CADCS simulation of the closed-loop cardiovascular system". In: *International journal of bio-medical computing* 22.1, pp. 39–49.

Barnard, Christiaan N (1969). "Human heart transplantation." In: *Canadian Medical Association Journal* 100.3, p. 91.

Bell, Robert M, Mihaela M Mocanu, and Derek M Yellon (2011). "Retrograde heart perfusion: the Langendorff technique of isolated heart perfusion". In: *Journal of molecular and cellular cardiology* 50.6, pp. 940–950.

Bellhouse, Brian J and L Talbot (1969). "The fluid mechanics of the aortic valve". In: *Journal of fluid mechanics* 35.4, pp. 721–735.

Brink, Johan G and David KC Cooper (2005). "Heart transplantation: the contributions of Christiaan Barnard and the University of Cape Town/Groote Schuur Hospital". In: *World journal of surgery* 29, pp. 953–961.

Cobert, Michael L, LaShondra M West, and Michael E Jessen (2008). "Machine perfusion for cardiac allograft preservation". In: *Current opinion in organ transplantation* 13.5, pp. 526–530.

Cobert, ML et al. (2010). "Importance of organ preservation solution composition in reducing myocardial edema during machine perfusion for heart transplantation". In: *Transplantation proceedings*. Vol. 42. 5. Elsevier, pp. 1591–1594.

Cook, Christopher et al. (2014). "The annual global economic burden of heart failure". In: *International journal of cardiology* 171.3, pp. 368–376.

De Canete, J Fernandez et al. (2013). "Object-oriented modeling and simulation of the closed loop cardiovascular system by using SIMSCAPE". In: *Computers in biology and medicine* 43.4, pp. 323–333.

Evans, RW (2013). "Aggregate Annual Health Care Expenditures Associated with Heart Transplantation in the United States: 1980-2011". In: *The Journal of Heart and Lung Transplantation* 32.4, S159.

Firestone, Leonard (1991). "Heart transplantation". In: *International Anesthesiology Clinics* 29.3, pp. 41–58.

Garcia, Damien et al. (2006). "Analytical modeling of the instantaneous maximal transvalvular pressure gradient in aortic stenosis". In: *Journal of biomechanics* 39.16, pp. 3036–3044.

Goodwill, Adam G et al. (2017). "Regulation of coronary blood flow". In: *Comprehensive Physiology* 7.2, p. 321.

Hess, Nicholas R, Luke A Ziegler, and David J Kaczorowski (2022). "Heart Donation and Preservation: Historical Perspectives, Current Technologies, and Future Directions". In: *Journal of Clinical Medicine* 11.19, p. 5762.

Hirshfeld Jr, John W and Ashwin S Nathan (2020). *Deriving function from structure: applying Hagen-Poiseuille to coronary arteries*.

Ji, Bingyang and Akif Ündar (2006). "An evaluation of the benefits of pulsatile versus nonpulsatile perfusion during cardiopulmonary bypass procedures in pediatric and adult cardiac patients". In: *Asaio Journal* 52.4, pp. 357–361.

Kapur, Navin K et al. (2015). "Hemodynamic effects of left atrial or left ventricular cannulation for acute circulatory support in a bovine model of left heart injury". In: *ASAIO Journal* 61.3, pp. 301–306.

Kim, Hyun Jin et al. (2010). "Patient-specific modeling of blood flow and pressure in human coronary arteries". In: *Annals of biomedical engineering* 38, pp. 3195–3209.

Kim, Subin, Bibin Prasad, and Jung Kyung Kim (2016). "Alignment of microbeads using spinning helical minichannel cartridge". In: *Journal of the Korean Society of Visualization* 14.3, pp. 38–45.

Kothari, Perin (2023). "Ex-Vivo Preservation of Heart Allografts—An Overview of the Current State". In: *Journal of Cardiovascular Development and Disease* 10.3, p. 105.

Mansouri, Mahdi (2016). *Physiological control of an implantable rotary blood pump*. University of Malaya (Malaysia).

Market Research Future, https://www.marketresearchfuture.com/ and (2018). *Global Transplant Diagnostics Market Overview Source: https://www.marketresearchfuture.com/reports/transplant-diagnostics-market-1324*.

Mathers, Colin D, Alan D Lopez, and Christopher JL Murray (2006). "The burden of disease and mortality by condition: data, methods, and results for 2001". In: *Global burden of disease and risk factors*.

Michael Rochette, Martijn Hoeijmakers (2024). "Get to the Heart of the Matter". In.
Painter, Page R, Patrik Edén, and Hans-Uno Bengtsson (2006). "Pulsatile blood flow, shear force, energy dissipation and Murray's Law". In: *Theoretical Biology and Medical Modelling* 3, pp. 1–10.
Pollock, Joshua D and Amgad N Makaryus (2017). "Physiology, cardiac cycle". In.
Porat, Eyal et al. (2000). "Hemodynamic changes and right heart support during vertical displacement of the beating heart". In: *The Annals of thoracic surgery* 69.4, pp. 1188–1191.
Pries, AR, Timothy W Secomb, and P Gaehtgens (1996). "Biophysical aspects of blood flow in the microvasculature". In: *Cardiovascular research* 32.4, pp. 654–667.
Querzoli, Giorgio et al. (2016). "A laboratory model of the aortic root flow including the coronary arteries". In: *Experiments in Fluids* 57, pp. 1–9.
Ramanathan, Tamilselvi and Henry Skinner (2005). "Coronary blood flow". In: *Continuing Education in Anaesthesia, Critical Care & Pain* 5.2, pp. 61–64.
Rebeyka, Ivan M et al. (1990). "Rapid cooling contracture of the myocardium: the adverse effect of prearrest cardiac hypothermia". In: *The Journal of thoracic and cardiovascular surgery* 100.2, pp. 240–249.
Rega, Filip et al. (2024). "Hypothermic oxygenated perfusion of the donor heart in heart transplantation: the short-term outcome from a randomised, controlled, open-label, multicentre clinical trial". In: *The Lancet* 404.10453, pp. 670–682.
Ruiz-Meana, Marisol et al. (2009). "Role of sarcoplasmic reticulum in mitochondrial permeability transition and cardiomyocyte death during reperfusion". In: *American Journal of Physiology-Heart and Circulatory Physiology* 297.4, H1281–H1289.
Sáez, Diana García et al. (2014). "Evaluation of the organ care system in heart transplantation with an adverse donor/recipient profile". In: *The Annals of thoracic surgery* 98.6, pp. 2099–2106.
Sáez, Diana García et al. (2015). "Ex vivo heart perfusion after cardiocirculatory death; a porcine model". In: *journal of surgical research* 195.1, pp. 311–314.
Salisbury, Peter F, Cecil E Cross, and P Andre Rieben (1962). "Intramyocardial pressure and strength of left ventricular contraction". In: *Circulation research* 10.4, pp. 608–623.
Schelbert, Heinrich R (2010). "Anatomy and physiology of coronary blood flow". In: *Journal of nuclear cardiology* 17.4, pp. 545–554.
Schichl, K and K Affeld (1993). "A computer controlled versatile pulse duplicator for precision testing of artificial heart valves". In: *The International journal of artificial organs* 16.10, pp. 722–728.
Schmid-Schönbein, GW et al. (1981). "Passive mechanical properties of human leukocytes". In: *Biophysical Journal* 36.1, pp. 243–256.
Sevre, Knut (2006). "Handbook of cardiac anatomy, physiology, and devices". eng. In: *Blood Pressure* 14.1, pp. 59–59. ISSN: 0803-7051.
SkyQuest (2024). *Heart Transplant Market Size, Share, Growth Analysis, By Type of Transplant(Orthotopic Heart Transplant, Heterotopic Heart Transplant, and Pediatric Heart Transplant), By Donor Type (Deceased Donor Heart Transplant, and Living Donor Heart Transplant), By Indication(Ischemic Cardiomyopathy, Dilated Cardiomyopathy, Congenital Heart Disease, Valvular Heart Disease), By Region - Industry Forecast 2025-2032*. URL: https://www.skyquestt.com/report/heart-transplant-market.
Smith, Deane E et al. (2022). "Early experience with donation after circulatory death heart transplantation using normothermic regional perfusion in the United States". In: *The Journal of Thoracic and Cardiovascular Surgery* 164.2, pp. 557–568.
Sorin Group Italia, S.r.l (2020). *S5® Cardiac surgery solutions S5 - The world-leading perfusion system*. Catalogue.
Strüber, Martin et al. (2009). "The current status of heart transplantation and the development of" artificial heart systems"". In: *Deutsches Ärzteblatt International* 106.28-29, p. 471.
Suleiman, M-S, AP Halestrap, and EJ Griffiths (2001). "Mitochondria: a target for myocardial protection". In: *Pharmacology & therapeutics* 89.1, pp. 29–46.
Taylor, Charles A et al. (2023). "Patient-specific modeling of blood flow in the coronary arteries". In: *Computer Methods in Applied Mechanics and Engineering* 417, p. 116414.
Urban, Marian et al. (2024). "Financial impact of donation after circulatory death heart transplantation: A single-center analysis". In: *Clinical Transplantation* 38.4, e15296.
Wald, Shaily, Alex Liberzon, and Idit Avrahami (2018). "A numerical study of the hemodynamic effect of the aortic valve on coronary flow". In: *Biomechanics and modeling in mechanobiology* 17, pp. 319–338.
White, Christopher W et al. (2013). "A cardioprotective preservation strategy employing ex vivo heart perfusion facilitates successful transplant of donor hearts after cardiocirculatory death". In: *The Journal of Heart and Lung Transplantation* 32.7, pp. 734–743.
White, Christopher W et al. (2015). "A whole blood–based perfusate provides superior preservation of myocardial function during ex vivo heart perfusion". In: *The Journal of Heart and Lung Transplantation* 34.1, pp. 113–121.
Wicomb, Winston Neville (1983). "The development of a system of 24 hours preservation of the heart for transplantation". In.

Zamir, Mair (2006). *The physics of coronary blood flow*. Springer Science & Business Media.

Zeng, An et al. (2023). "ImageCAS: A large-scale dataset and benchmark for coronary artery segmentation based on computed tomography angiography images". In: *Computerized Medical Imaging and Graphics*, p. 102287.

Zhang, John X.J. and Kazunori Hoshino (2014). "Chapter 3 - Microfluidics and Micro Total Analytical Systems". In: *Molecular Sensors and Nanodevices*. Ed. by John X.J. Zhang and Kazunori Hoshino. Oxford: William Andrew Publishing, pp. 103–168. ISBN: 978-1-4557-7631-3. DOI: https://doi.org/10.1016/B978-1-4557-7631-3.00003-X. URL: https://www.sciencedirect.com/science/article/pii/B978145577631300003X.

Zhou, Yifang, Ghassan S Kassab, and Sabee Molloi (1999). "On the design of the coronary arterial tree: a generalization of Murray's law". In: *Physics in Medicine & Biology* 44.12, p. 2929.

Appendix A

Global Lumped Parameter Model

A.1 System State Initialisation

Parameter	Description	Unit	Value
x10	Initial aortic pressure	(mmHg)	71.112
x20	Initial blood flow in arterial systemic circulation	($cm^3\ s^{-1}$)	8.880
x30	Initial systemic pressure	(mmHg)	70.516
x40	Initial blood flow in venous systemic circulation	($cm^3\ s^{-1}$)	67.337
x50	Initial right venous–atrial pressure	(mmHg)	3.328
x60	Initial right ventricle volume	(cm^3)	105.520
x70	Initial pulmonary venous pressure	(mmHg)	13.417
x80	Initial blood flow in arterial pulmonary circulation	($cm^3\ s^{-1}$)	0.786
x90	Initial pulmonary pressure	(mmHg)	13.393
x100	Initial blood flow in venous pulmonary circulation	($cm^3\ s^{-1}$)	23.836
x110	Initial left venous–atrial pressure	(mmHg)	11.294
x120	Initial left ventricle volume	(cm^3)	112.760
PipL	Left peak isovolumic pressure	(mmHg)	50.000
PipR	Right peak isovolumetric pressure	(mmHg)	24.000
EdL	Left elastance while diastole	($mmHg\ cm^{-3}$)	0.100
EsL	Left elastance while systole	($mmHg\ cm^{-3}$)	1.375
EdR	Right elastance while diastole	($mmHg\ cm^{-3}$)	0.030
EsR	Right elastance while systole	($mmHg\ cm^{-3}$)	0.328
RmL	Left myo. viscosity resistance	($mmHg\ s\ cm^{-3}$)	0.080
RmR	Right myo. viscosity resistance	($mmHg\ s\ cm^{-3}$)	0.0175
R1	Aortic valve resistance	($mmHg\ s\ cm^{-3}$)	3.7511E-03
R2	Aortic-systemic resistance	($mmHg\ s\ cm^{-3}$)	6.7501E-02
R3	Systemic resistance	($mmHg\ s\ cm^{-3}$)	1.000
R4	Tricuspid valve resistance	($mmHg\ s\ cm^{-3}$)	3.751E-03
R5	Pulmonary valve resistance	($mmHg\ s\ cm^{-3}$)	3.751E-03
R6	Pulmonary artery resistance	($mmHg\ s\ cm^{-3}$)	3.3761E-02
R7	Pulmonary resistance	($mmHg\ s\ cm^{-3}$)	0.101
R8	Mitral valve resistance	($mmHg\ s\ cm^{-3}$)	3.751E-03
L1	Aortic-systemic inertance	($mmHg\ s^{-2}\ cm^{-3}$)	8.250E-04
L2	Systemic inertance	($mmHg\ s^{-2}\ cm^{-3}$)	3.600E-03
L3	Pulmonary artery inertance	($mmHg\ s^{-2}\ cm^{-3}$)	7.500E-04
L4	Pulmonary inertance	($mmHg\ s^{-2}\ cm^{-3}$)	3.080E-03
C1	Aortic compliance	($mmHg^{-1}\ cm^3$)	0.220
C2	Arterial systemic compliance	($mmHg^{-1}\ cm^3$)	1.460
C3	Venous systemic compliance	($mmHg^{-1}\ cm^3$)	20.000
C4	Pulmonary artery compliance	($mmHg^{-1}\ cm^3$)	9.000E-02
C5	Arterial pulmonary compliance	($mmHg^{-1}\ cm^3$)	2.670
C6	Venous pulmonary compliance	($mmHg^{-1}\ cm^3$)	46.700
tc	Cardiac period	(s)	0.800

A.2 Declarations

State: Xl X2 X3 X4 X5 X6 X7 X8 X9 X10 X11 X12
Der: DXl DX2 DX3 DX4 DX5 DX6 DX7 DX8 DX9 DX10 DX11 DX12 Time T
Ts = 0.16 + 0.3*Tc
Tm = mod(T, Tc)
A = if Tm < Ts then (1 - cos(2Tm/Ts))/Z
UL = ULO*A
UR = URO*A
EL = ELD + ELS*A
ER = ERD + ERS*A
Zl = UL + XlZ'EL - Xl
22 = X5 - UR - X6*ER
23 = UR + X6*ER - X7
24 = XII - UL - X12*EL
Sl = if Zl > 0 then 1 else 0

A.3 Auxiliary variables

S2 = if Z2 > 0 then 1 else 0
S3 = if Z3 > 0 then 1 else 0
S4 = if Z4 > 0 then 1 else 0
LVOF = Zl*Sl/(RL
RVIF = Z2*S2/R4
RVOF = Z3*S3/(RR + RS)
LVIF = Z4*S4/R8
LVP = UL + EL*X12 - RL*LVOF
RVP = UR + ER*X6 - RR*RVOF
DXl = (Sl*Zl/(RL + RI) - X2)/Cl
DX2 = (Xl - R2*X2 - X3)/L
DX3 = (X2 - X4)/C2
DX4 = (X3 - R3*X4 - X5)/L2
DX5 = (X4 - S2*Z2/R4)/C3
DX6 = S2*Z2/R4 - S3*Z3/(RR + R5)
DX7 = (S3*Z3/(RR + R5) - X8)/C4
DX8 = (X7 - R6*X8 - X9)/L3
DX9 = (X8 - X10)/C5
DX10 = (X9 - R7*X10 - X11)/L4
DX11 = (X10 - S4*Z4/R8)/C6
DX12 = (S4*Z4/R8 - Sl*Zl/Rl

A.4 Display of Current Values of States, Derivatives, Auxiliary Variables and Parameters

TIME: T, STATE: Xl, x4, x7, x10, INIT: Xl, x4, x7, x10
DER: DXl, DX4, DX7, DX10, PAR: Tc, URO, ERD, R1, R2, R3, c4, CS, C6, VAR: TS, UL, ER
23, s2, LVOF, LVIF, CONTINUOUS SYSTEM CIRC
1.6000, 71.112, x2, 8.8880, 67.337, x5, 3.3285
x3, 70.516, X6, 105.52, x9, 13.393, x12, 112.76 x3, 70.537, X6, 105.46, x9, 13.392, x12, 112.76 DX3, -40.033, DX6, 43.433
13.417, 23.836, 71.132, 67.359 13.416, 23.830 -40.400, -41.318

-8.7373, -102.67 0.80000, 24.000 3.0000E-02, 3.7510E-03, 3.7510E-03, 6.7500E-02, 1.0000, 9.0000E-02, 2.6700
46.700 0.40000, 0.0000E+00, 3.0000E-02 -10.251, 1.0000
0.0000E+00, 4.8520 X8, 0.78636, 11.295, -5.4654, 1.1952, 3.4281 0.40652, 3.1416, 0.10000, 0.32880, 3.7510E-03, 3.7510E-03, 8.2500E-04, 3.6000E-03, 3.3760E-02, 0.10130
0.0000E+00, 0.0000E+00, -59.836 1.81999E-02, 0.0000E+00
43.433, 11.276 x11, x2, x5 X8, 0.78612, 11.294, 8.8900, 3.3268
DER: DX2, DX5, DX8, DX11, PI, ELD, ERS, PAR: R4, R8, L1, L2, R6, R7, VAR: Tm, UR, Z1
24, s3, RVIF, PLV, DX9, DX12, ULO, ELS, RL, RR, C1
c2, c3, L3, L4, A, EL, 22, S1, s4, RVOF, PRV
-8.6330, 4.8520 50.000, 1.3750, 8.0000E-02, 1.7500E-02, 0.22000 1.4600
20.000, 7.5000E-04, 3.0500E-03 0.0000E+00, 0.10000 0.16292, 0.0000E+00, 1.0000, 0.0000E+00
3.1655

A.5 EVR Calculation Algorithm

Algorithm 1 EVR Determination

Input: ap, peakp, rvap, R3, tc, ts
Output: cpp, cbf, EVR, SNR, meanEVR, meancpp
$tse \leftarrow (ts \times 0.5)/tc$
$diffonset \leftarrow \text{floor}(\text{diff}(peakp) \times tse)$
$padded\_diff \leftarrow [diffonset, \text{zeros}(1, \text{length}(peakp) - \text{length}(diffonset))]$
$sysend \leftarrow peakp + padded\_diff$
$adp \leftarrow ap(sysend)$
$asp \leftarrow ap(peakp)$
$rvapd \leftarrow rvap(sysend)$
$cpp \leftarrow \text{abs}(adp - rvapd)$
$cbf \leftarrow cpp/R3$
$len1 \leftarrow \text{length}(asp)$
$len2 \leftarrow \text{length}(cpp)$
$max\_length \leftarrow \max(len1, len2)$
if len1 < len2 **then**
    $last\_value \leftarrow asp[\text{end}]$
    $asp \leftarrow \text{append}(asp, \text{repmat}(last\_value, \text{max\_length} - len1, 1))$
end if
if len2 < len1 **then**
    $last\_value \leftarrow cpp[\text{end}]$
    $cpp \leftarrow \text{append}(cpp, \text{repmat}(last\_value, \text{max\_length} - len2, 1))$
end if
Design a 3rd order Bessel low-pass filter
Apply the filter to ap to obtain $rmsap$
$noise \leftarrow ap - rmsap$
$noise\_power \leftarrow \text{mean}(noise^2)$
$signal\_power \leftarrow \text{mean}(rmsap^2)$
$SNR \leftarrow signal\_power/noise\_power$
$DPTI \leftarrow cpp \times (tc - ts)$
$TTI \leftarrow asp \times ts$
$EVR \leftarrow DPTI/TTI$
if SNR > 500 **then**
    Compute $stepinfo$ for ap
else
    Compute $stepinfo$ for $rmsap$
end if
$meanEVR \leftarrow \text{mean}(EVR)$
$meancpp \leftarrow \text{rms}(cpp)$

Appendix B

Coronary Vascular Bed Model

B.1 Parameter Values of the Closed-Loop System

Table B.1 Parameters of Closed Loop Coronary Vascular Bed System at Rest, Light and Moderate Exercise.

	R_{a}			$R_{\mathrm{a\text{-}micro}}$			$R_{\mathrm{v}} + R_{\mathrm{v\text{-}micro}}$			C_{a}			c_{im}		
	R	E1	E2	R	E1	E2	R	E1	E2	R	E1	E2	R	E1	E2
a: LAD1	183	177	76	299	56	24	94	44	18	0.34	0.75	0.75	2.89	6.88	6.88
b: LAD2	131	126	52	214	40	16	67	32	13	0.48	1.02	1.02	4.04	9.34	9.34
c: LAD3	123	91	51	148	39	16	65	31	12	0.49	1.07	1.07	4.16	9.74	9.74
d: LAD4	75	55	31	90	24	10	40	19	7	0.80	1.74	1.74	6.82	15.9	15.9
e: LCX1	49	47	20	80	15	6.2	25	12	5	1.28	2.79	2.79	10.8	25.4	25.4
f: LCX2	160	154	65	261	49	20	82	39	15	0.39	0.85	0.85	3.31	7.78	7.78
g: LCX3	216	208	87	353	66	27	111	53	21	0.29	0.63	0.63	2.45	5.74	5.74
h: LCX4	170	164	68	277	52	21	87	41	16	0.37	0.80	0.80	3.12	7.29	7.29
i: RCA1	168	163	71	274	51	22	86	40	16	0.37	0.83	0.83	3.15	7.60	7.60
j: RCA2	236	229	98	385	72	31	121	56	23	0.26	0.59	0.59	2.24	5.38	5.38
k: RCA3	266	257	110	435	81	35	136	64	25	0.23	0.52	0.52	1.99	4.72	4.72
$c^{\star}$: LAD3	100		51	146		16	65		12	0.49		1.07	4.16		9.74
$c^{\star\star}$: LAD3	89		51	146		16	65		12	0.49		1.07	4.16		9.74
$c^{\star\star\star}$: LAD3	80		51	98		16	65		12	0.49		1.07	4.16		9.74
$c^{\star\star\star\star}$: LAD3	57		51	93		16	65		12	0.49		1.07	4.16		9.74
d: LAD4	65		31	89		10	40		7	0.80		1.74	6.82		15.9
d** : LAD4	54		31	89		10	40		7	0.80		1.74	6.82		15.9
d*** : LAD4	48		31	58		10	40		7	0.80		1.74	6.82		15.9
d**** : LAD4	35		31	57		10	40		7	0.80		1.74	6.82		15.9

B.2 Approximating Coefficient of Theoretical Pump Initialisation

Control Parameter	**Variable**	**Current Value**	**Unit**
First Approximating Coefficient	c_0	4.524143312	Pa·m^3/kg
Second Approximating Coefficient	c_1	-2.69E+00	Pa·s/kg
Third Approximating Coefficient	c_2	1.30E-08	Pa·s^2/(kg·m^3)
Fourth Approximating Coefficient	c_3	1.54E-01	Pa·s^2/(kg·m^3)
Pump Correction Factor	k	0,768701594	-
Pump Design Delivery	q_{D}	5	lpm
Reference Angular Velocity	ω_{ref}	3000	rpm
Reference Density	ρ_{ref}	1069.68	kg/m^3
Leak Resistance	k_{leak}	1.00E+08	Pa·s/m^3
Reference Drive Shaft Torque	T_0	0.2	N·m
Torque-Pressure Coefficient	k_p	0.1585E-04	N·m/Pa
Backflow Angular Speed Threshold	ω_{min}	1.00E-09	rad/s

B.3 System Pump Specification Sheet Profile

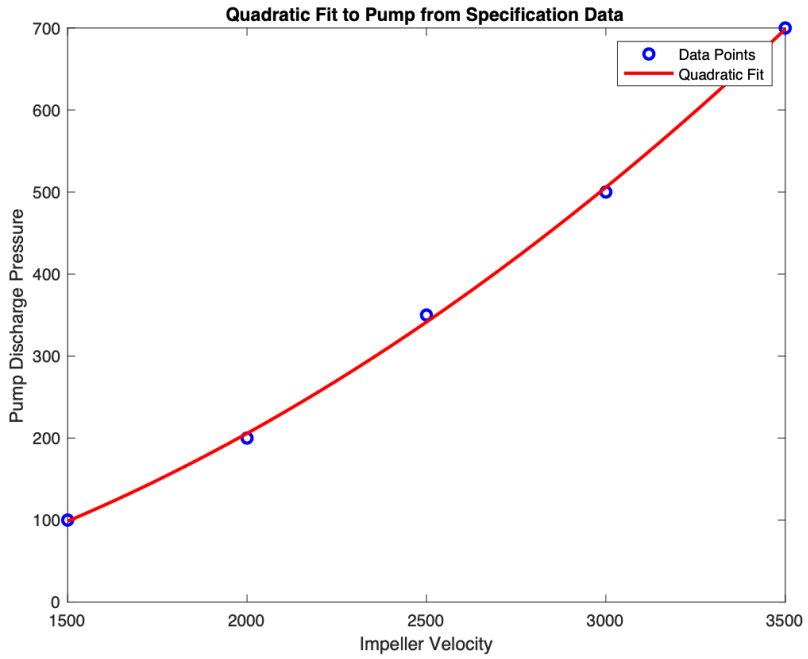

FIGURE B.1: Pump Spec. Sheet P-v Characteristic Curve

B.4 Mesh Model Center Line Lengths

Table B.3 Centreline Statistics

Boundary Condition	Segment length (mm)
Ao	64.18
RCA	174.32
Ao -> LCX	28.75
LCX	20.53
LCX -> LAD1	7.58
LAD1	25.71
LAD2	46.03
Total	367.11
Mean	52.44

Appendix C

Bench Test Rig

C.1 Motor Design Specifications (BLE17E40-02-RO)

Motor Specification	**Value**
Phase	3
Frame Size	42 mm
NEMA Size	NEMA 17
Body Length (Dimension A)	101 mm
Rated Voltage	48 VDC
Rated Output Power	90 W
Rated Speed	4000 RPM
Max Speed	5000 RPM
Rated Torque	0.215 Nm
Rated Current	2.4 A
Max Torque	0.43 Nm
Resistance	1.47 ohm
Terminal Inductance	1.57 mH
Torque Constant	0.089 Nm/A
Rotor Inertia	144 g-cm²
Weight	0.83 kg
Electrical Time Constant	1.1 ms
Mechanical Time Constant	2.9 ms
Hall Effect Angle	120° electrical Angle
Radial Play	0.05 mm @ 0.45 kg
End Play	0.08 mm @ 45 kg
Max, Radial Force	10 mm @ 1.53 kg
Max, Axial Force	1.02 kg
Insulation Class	Class B
Dielectric Strength	500 VDC for 1 minute
Insulation Resistance	100 Min, 500 VDC
Ambient Operating Temperature	-20.00 °C to 50.00 °C
Storage Temperature	-20.00 °C to 100.00 °C
Humidity Range (%)	85% (RH) non-condensing
Direction Of Rotation	CCW

DIMENSIONS	
Model	BL17E40-02
DIM, A (length) mm	101 mm

C.2 Speed Controller Specifications (BLDC-50)

Drive Type	3-phase MOSFET bridge. D/Q sine current control
Supply Voltage	12-48VDC

Supply Voltage Type	DC
Max Power Input	10-70VDC
Control Modes	Velocity Control
Feedback	Halls
Setup Method	Switch / potentiometer
Digital Inputs	8
Digital Outputs	2
Analog Inputs	1 (0 to 5 Vdc, 12 bit)
Status LEDs	1 red, 1 green
Dimensions	3.9 x 2.6 x 1.2 inches
Weight	6.0 oz
Velocity Ripple	+/-0.5% Rated Velocity Error
Under Voltage Protection	10V
Over Voltage Protection	70V
Input Signal Voltage (IO)	5-24V
OUT Maximum Voltage	30V
Ambient Temperature	0 to 40°C
Storage Temperature	-10 to 70°C
Humidity	90% non-condensing
Output Current	BLDC50: 0.1 — 5.0A/phase precision to 0.1A BLDC100: 0.1 — 10.0A/phase precision to 0.1A
Protection Function	Over voltage, under voltage, over temperature, short circuit (phase to phase, phase to ground), bad Hall signal.
OUT Maximum Output Current	100mA

C.3 Pump Cone Design Specification

Pump Specification	**Value**
Priming Volume	57 ml
Maximum Flow Rate	8 lpm
Maximum Outlet Pressure	800 mmHg
Inlet/Outlet Port	3/8 in, (9.5 mm)
Pump Casing	Polycarbonate
Shaft	Stainless Steel
Impeller & Magnet Housing	ABS
Bearings	HDPE
Magnet	Nylon NdFeB Blend

C.4 Driving Unit Specification

Drive Unit Specification	**Value**
Speed display	7 LEDs
Resolution	500 RPM per LED (starting at 1000 RPM)
Displayed range of speed	1000 to 4000 RPM
Accuracy	±250 RPM
Diameter	100 mm (3.9 in) (without mast holder)
Height	250 mm (9.8 in)
Weight	4.5 kg (9.9 lbs)
Height hand crank	115 mm (4.5 in)

Diameter hand crank	26 mm (1 in)
Gear Ratio	Approximately 1:35

C.5 Hydraulic Model Initialisation

C.5.1 Model Constants

Initial Conditions and Set Constants	**Value**	**Unit**
Fluid Properties		
Hydraulic Fluid Index	Water-Glycol 60/40	-
System Temperature	37	°C
Relative Amount of Trapped Air	0,005	-
Viscosity Derating Factor	1	
Density	1069,68	kg/m^3
Viscosity	2,84423	cSt
Bulk Modulus	2,29E+09	-
Affinity Reservoir		
Presurization	0,101325	MPa
Initial Fluid Volume	1	m^3
Return Line Diameter	1	m
Return Line Pressure Loss Coefficient	1	
Aortic Reservoir		
Pressurization 1 atm		
Tank Cross-Sectional Area	13,5	cm^2
Port A Pipeline (Inlet) Diameter	5	mm
Port A Pressure Loss Coefficient	1,2	-
Port B Height above Port A	3	cm
Port B Pipeline (Outlet) Diameter	3	mm
Port B Pressure Loss Coefficient	1,2	-
Acceleration due to Gravity	9,80665	m/s^2
Initial Fluid Volume	0	cm^3
Coronary Catchment Bed		
Pressurization 1 atm		
Tank Cross Sectional Area	1	cm^2
Inlet Pipeline Diameter	3	mm
Pipeline Pressure Loss Coefficient	1,2	-
Acceleration due to Gravity	9,80665	m/s^2
Minimum Level of Fluid	1,00E-03	mm
Nominal Fluid Volume	1	cm^3
Connecting Hydraulic Pipeline		
Internal Diameter	2E+00	cm
Laminar Friction Constant for Darcy Friction Factor	64	-
Pipe Length	50	cm
Aggregate Equivalent Length of Local Resistances	1	cm
Internal Surface Roughness Height	1,50E-05	cm
Laminar Flow Upper Reynolds Number Limit	2000	-
Turbulent Flow Lower Reynolds Number Limit	4000	-
Initial Pressure	1	atm
Pipe Wall Type	Rigid	-
Specific Heat Ratio	1,4	-
Port A Elevation from Reference Plane	0	cm
Port B Elevation from Reference Plane	0	cm
Gravitational Acceleration	9,80665	m/s^2
Heart Model		
Initial Aortic Pressure	0	mmHg
Initial Aortic Fluid Volume	0	cm^3

C.5.2 Hydraulic System State Parameters

System State Parameter	Variable	Unit
Input		
Motor Signal	Φ_{motor}	rpm
Output		
Motor Torque	T_{DS}	N·m
Impeller Velocity	ω_{impeller}	rpm
Aortic Volume	V_{Ao}	cm^3
Aortic Flow Rate	q_{Ao}	cm^3/s
Coronary Volume	V_{bed}	cm^3
Coronary Flow Rate	q_{bed}	cm^3/s
Centrifugal Discharge Pressure	P_{pump}	Pa

C.5.3 Parameter Configurations

System State Declaration	Variable	Expression	Unit
Heart Model			
Instantaneous Aortic Pressure	DX10	*See Appendix A.3	mmHg
Hydraulic			
Aortic Reservoir Pressurization	Paor	DX10·0.000133322	MPa
Connecting Hydraulic Pipeline Pressurization	Pcon	DX10·0.000133322·M1	MPa
Coronary Catchment Bed Pressurization	Pbed	DX10·0.000133322·M2	MPa
Motor			
Shaft Speed	ω_{shaft}	SSG·Φ_{motor}·GR	rad/s
Pump Flow	q_{pump}	T_{DS}·PCF	cm^3/s

C.6 Parameter Estimation Solver Calibration Data

Table C.9 Trust-Region Reflective Newton Algorithm

Iteration	Cost	Norm of Step	First-order Optimality
0	423.923	-	-
1	91.7485	10	6.39e+07
2	9.61073	20	2.62e+07
3	0.527239	40	4.2e+06
4	0.317593	80	1.77e+05
5	0.317593	0.552	1.77e+05
6	0.288207	0.0276	1.47e+05
7	0.288207	0.0552	1.47e+05
8	0.285427	0.00276	1.48e+05
9	0.280069	0.00552	1.37e+05
10	0.272101	0.011	2.64e+05
11	0.269676	0.0221	2.4e+05
12	0.269676	0.0441	2.4e+05
13	0.267592	0.00221	1.31e+05
14	0.263658	0.00441	3.99e+04
15	0.262942	0.00883	1.28e+05
16	0.262942	0.0177	1.28e+05
17	0.262942	0.000883	1.28e+05
18	0.262905	4.41e-05	1.28e+05
19	0.26283	8.83e-05	1.27e+05
20	0.26283	0.000177	1.27e+05

C.6.1 Estimated Parameter Values

Table C.10 Initial and Estimated Values of System Parameters

Parameter	Initial Value	Estimated Value
Upper Tank Cross-Sectional Area [cm^2]	35.911	35.98
Pump Constant	0.42433	0.32208
Upper Tank Area of Inlet Port [mm^2]	1.008	1.3106
Upper Tank Area of Outlet Port [mm^2]	0.40199	0.35874
Gravity Constant	9.81	9.81
Lower Tank Cross-Sectional Area [cm^2]	9.9686	14.634
First Approximating Coefficient	1.7101e+05	1.7101e+05
Second Approximating Coefficient	-1.722	-1.7226
Third Approximating Coefficient	3898.9	3898.9
Fourth Approximating Coefficient	2.1589e+05	2.1589e+05
Fluid Density [kg/m^3]	1069.7	1069.7

C.7 Reservoir Tank Profiles

C.7.1 Original

Res A Volume Heights above Datum		Res B Volume Heights above Datum	
Volume [ml]	**Height [cm]**	**Volume [ml]**	**Height [cm]**
1100	105,50	0,00	91,00
1050	105,10	5,00	91,60
1000	104,70	10,00	92,25
950	104,20	15,00	92,80
900	103,70	20,00	93,90
850	103,20	30,00	94,00
800	102,85	40,00	94,65
750	102,30	55,00	95,50
700	101,80	75,00	96,20
650	100,60	100,00	97,00
600	100,10	150,00	97,90
550	99,70	200,00	98,50
500	99,00	300,00	99,40
450	99,20	400,00	100,20
400	98,70	600,00	101,75
350	98,10	800,00	103,30
300	97,60	1000,00	104,70
250	97,10	1200,00	106,10
200	96,60		
150	95,80	**Pump Inlet/Outlet**	
100	94,20	70,00	
50	90,85	**Cannula Outlet**	
0,00	83,50	118,00	
		Res B Inlet	
		112,70	

C.7.2 Normalised Reservoir Data

Res A Volume [ml]	Res A Height above Datum [cm]	Res B Volume [ml]	Res B Height above Datum [cm]	Normalized Res. A Height	Normalized Res. B Height
720	102.00	0	91.00	102.00	91.00
700	101.80	8	91.99	97.43	91.10

Res A Volume [ml]	Res A Height above Datum [cm]	Res B Volume [ml]	Res B Height above Datum [cm]	Normalized Res. A Height	Normalized Res. B Height
650	100.60	70	96.03	96.44	91.86
600	100.10	125	97.45	95.44	92.54
550	99.70	150	97.90	94.45	92.84
500	99.00	240	98.86	93.45	93.95
450	99.20	280	99.22	92.46	94.44
400	98.70	340	99.72	91.46	95.18
350	98.10	375	100.00	90.47	95.61
300	97.60	425	100.39	89.47	96.22
250	97.10	490	100.90	88.48	97.02
200	96.60	525	101.17	87.48	97.45
180	96.12	540	101.29	87.08	97.63
170	96.12	580	101.60	86.88	98.12

C.7.3 Normalised Reservoir Volume-Level Profiles

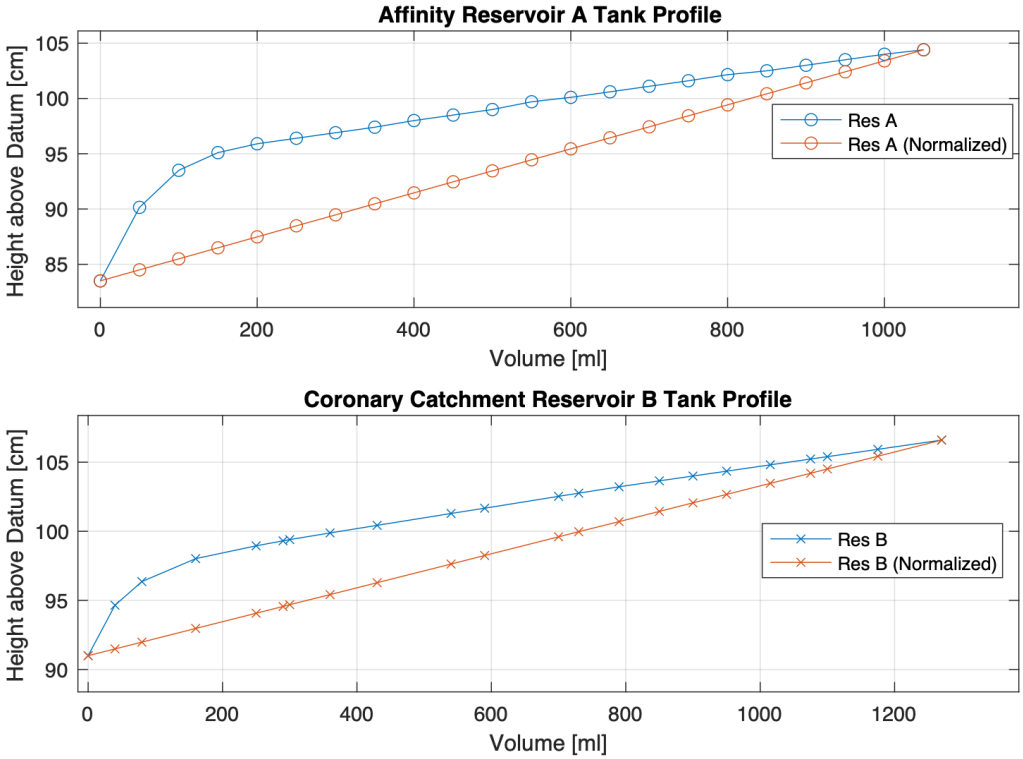

FIGURE C.1: Original and Normalised Tank Profiles

C.8 Trial 1: Steady-State Experimental Data

Table C.13 Time, Res A, Res B Data

Time [s]	Lap [s]	Res A Vol [ml]	Res A H [cm]	Res B Vol [ml]	Res B H [cm]	Res B Inflow [L/min]
0.00	0.00	1050	104.4	0	91.00	0.048
50.43	50.43	1000	104.0	40	94.65	0.048
92.97	42.54	950	103.5	80	96.36	0.056
156.34	63.36	900	103.0	160	98.02	0.076
212.35	56.01	850	102.5	250	98.95	0.096
282.81	70.46	800	102.2	290	99.31	0.034
365.31	82.49	750	101.6	300	99.40	0.007
413.45	48.14	700	101.1	360	99.88	0.075
477.91	64.46	650	100.6	430	100.4	0.065
538.71	60.79	600	100.1	540	101.3	0.109
...	...	...	...	...	...	...
4042.62	2362.41	0	83.5	1270	106.6	0.002

Table C.14 Outcomes and Head Flow Data

Time [s]	Res A Out [L/min]	Norm. A H	Norm. B H	MidPt Flow [L/min]	Δ Head [cm]	Disch. Flow [L/min]
0.00	0.0595	104.4	91.00	0.0535	8.30	-0.012
50.43	0.0595	103.4	91.49	0.0535	9.30	-0.012
92.97	0.0705	102.4	91.98	0.0635	10.29	-0.014
156.34	0.0473	101.4	92.97	0.0616	11.29	0.028
212.35	0.0536	100.4	94.07	0.0750	12.28	0.043
282.81	0.0426	99.42	94.56	0.0383	13.28	-0.009
365.31	0.0364	98.43	94.68	0.0218	14.27	-0.029
413.45	0.0623	97.43	95.42	0.0686	15.27	0.012
477.91	0.0465	96.44	96.28	0.0558	16.26	0.019
538.71	0.0494	95.44	97.63	0.0790	17.26	0.059
...	...	...	...	...	...	...
4042.62	0.0013	83.50	106.6	0.0018	29.20	0.001

C.8.1 Captured Raw Flow Data

Table C.15 Motor Speed = 50 rpm, Impeller Speed = 15 (Part 1)

Time [s]	Lap Int [s]	Res A Vol [ml]	Res A H [cm]	Res B Vol [ml]	Res B H [cm]	Res B Inflow [L/min]
78.94	78.94	720	102.00	0	91.00	0.00204
314.73	235.79	700	101.80	8	91.99	0.00204
509.13	273.34	650	100.60	70	96.03	0.01361
603.25	329.91	600	100.10	125	97.45	0.01000
959.97	630.06	550	99.70	150	97.90	0.00238
1226.41	596.35	500	99.00	240	98.86	0.00906
1524.71	928.36	450	99.20	280	99.22	0.00259
1878.52	950.16	400	98.70	340	99.72	0.00379

Table C.16 Motor Speed = 50 rpm, Impeller Speed = 15 (Part 2)

Time [s]	**Res A Outflow [L/min]**	**Norm Res. A H**	**Norm Res. B H**	**MidPoint Flow [L/min]**	**Δ Head [cm]**	**Disc Flow [L/min]**
78.94	0.00509	102.00	91.00	0.00356	10.70	-0.003
314.73	0.00509	97.43	91.10	0.00356	15.27	-0.003
509.13	0.01098	96.44	91.86	0.01229	16.26	0.003
603.25	0.00909	95.44	92.54	0.00955	17.26	0.001
959.97	0.00476	94.45	92.84	0.00357	18.25	-0.002
1226.41	0.00503	93.45	93.95	0.00704	19.25	0.004
1524.71	0.00323	92.46	94.44	0.00291	20.24	-0.001
1878.52	0.00316	91.46	95.18	0.00347	21.24	0.001

C.9 Trial 2: Dynamic Response Experimental Data

C.9.1 Phase 1:

TABLE C.17: Simulation and Measured Population Sizes for Experiment 1 and 2

Experiment	Initial Simulation Experiment #1		Initial Simulation Experiment #2	
	Population Size (N)	Sample Size (n)	Population Size (N)	Sample Size (n)
Sim	301218	30122	301218	21516
Measured	10	-	14	-

TABLE C.18: Simulation and Measured Population Sizes for Experiments 3 and 4

Experiment	Initial Simulation Experiment #3		Initial Simulation Experiment #4	
	Population Size (N)	Sample Size (n)	Population Size (N)	Sample Size (n)
Sim	301218	20082	301335	30134
Measured	15	-	10	-

TABLE C.19: Simulation and Measured Population Sizes for Experiments 5 and 6

Experiment	Initial Simulation Experiment #5		Initial Simulation Experiment #6	
	Population Size (N)	Sample Size (n)	Population Size (N)	Sample Size (n)
Sim	301335	21524	300856	21490
Measured	14	-	14	-

TABLE C.20: Simulation and Measured Population Sizes for Experiments 7 and 8

Experiment	Initial Simulation Experiment #7		Initial Simulation Experiment #8	
	Population Size (N)	Sample Size (n)	Population Size (N)	Sample Size (n)
Sim	300856	18804	301867	18867
Measured	16	-	16	-

Experiment 1

Table C.21 Initial Simulation Experiment #1

Sampled Time	**Measured Time s**	Coronary Volume (Sim/Measured)
0	0	0/0
37.05	5.00	21.78/5.00
77.04	10.00	45.60/10.00
116.30	15.00	63.58/15.00
157.12	20.00	91.16/20.00
197.90	30.00	140.51/30.00
238.69	40.00	221.52/40.00
279.12	55.00	340.64/55.00
319.28	75.00	503.05/75.00
400	100.00	979.20/100.00

Experiment 2

Table C.22 Initial Simulation Experiment #2

Sampled Time	Measured Time	Coronary Volume (Sim/Measured)
0	0	0/0
25.85	5.00	13.15/5.00
54.19	10.00	33.43/10.00
82.63	15.00	48.18/15.00
110.69	20.00	60.81/20.00
139.53	30.00	77.28/30.00
168.86	40.00	102.65/40.00
197.90	55.00	140.51/55.00
227.18	75.00	194.96/75.00
256.24	100.00	268.09/100.00

Experiment 3

Table C.23 Initial Simulation Experiment #3

Sampled Time	Measured Time	Coronary Volume (Sim/Measured)
0	0	0/0
24.01	5.00	11.71/5.00
50.41	10.00	31.07/10.00
77.04	15.00	45.60/15.00
103.25	20.00	57.35/20.00
129.83	30.00	71.03/30.00
157.13	40.00	91.17/40.00
184.30	55.00	120.96/55.00
211.50	75.00	163.58/75.00
238.69	100.00	221.53/100.00

Experiment 4

Table C.24 Initial Simulation Experiment #4

Sampled Time	Measured Time	Coronary Volume (Sim/Measured)
0	0	0/0
37.07	5.00	14.18/5.00
77.04	10.00	29.99/10.00
116.33	15.00	41.92/15.00
157.10	20.00	60.37/20.00
197.90	30.00	93.57/30.00
238.64	40.00	148.10/40.00
279.13	55.00	228.64/55.00
319.31	75.00	338.62/75.00
400	100.00	662.40/100.00

Experiment 5

Table C.25 Initial Simulation Experiment #5

Sampled Time	Measured Time	Coronary Volume (Sim/Measured)
0	0	0/0
25.84	5.00	8.43/5.00
54.26	10.00	21.95/10.00
82.64	15.00	31.70/15.00
110.70	20.00	40.08/20.00
139.55	30.00	51.07/30.00
168.85	40.00	68.10/40.00
197.90	55.00	93.57/55.00
226.91	75.00	129.87/75.00
256.16	100.00	179.45/100.00

Experiment 6

Table C.26 Initial Simulation Experiment #6

Sampled Time	Measured Time	Coronary Volume (Sim/Measured)
0	0	0/0
24.10	5.00	12.15/5.00
50.32	10.00	30.48/10.00
76.80	15.00	44.05/15.00
102.97	20.00	55.45/20.00
129.66	30.00	69.81/30.00
157.13	40.00	89.35/40.00
184.32	55.00	118.13/55.00
211.50	75.00	158.60/75.00
238.69	100.00	214.54/100.00

Experiment 7

Table C.27 Initial Simulation Experiment #7

Sampled Time	Measured Time	Coronary Volume (Sim/Measured)
0	0	0/0
37.04	5.00	13.47/5.00
77.06	10.00	27.89/10.00
116.30	15.00	38.77/15.00
157.10	20.00	56.02/20.00
197.92	30.00	87.54/30.00
238.70	40.00	138.12/40.00
279.10	55.00	213.55/55.00
319.28	75.00	316.56/75.00
400	100.00	630.45/100.00

Experiment 8

Table C.28 Initial Simulation Experiment #8

Sampled Time	Measured Time	Coronary Volume (Sim/Measured)
0	0	0/0
24.03	5.00	11.42/5.00
50.40	10.00	29.91/10.00
77.08	15.00	43.72/15.00
103.28	20.00	54.64/20.00
129.87	30.00	69.02/30.00
157.14	40.00	88.46/40.00
184.30	55.00	117.38/55.00
211.50	75.00	157.30/75.00
238.69	100.00	214.21/100.00

C.9.2 Phase 2

Table C.29 Experiment 1 and Experiment 2 Data

Time 1 [s]	**Volume 1 [mL]**	**Time 2 [s]**	**Volume 2 [mL]**
0.00	0.00	0.00	0.00
77.61	5.00	22.98	5.00
101.51	10.00	33.53	10.00
126.48	15.00	44.53	15.00
148.76	20.00	55.59	20.00
182.06	30.00	85.64	30.00
202.12	40.00	119.20	40.00
220.78	55.00	162.83	55.00
233.74	75.00	185.59	75.00
248.38	100.00	206.45	100.00
267.38	150.00	230.26	150.00
282.83	200.00	248.11	200.00
311.94	300.00	279.03	300.00
335.13	600.00	302.98	400.00
368.40	800.00	341.26	600.00
400.00	900.00	378.48	800.00

Table C.30 Experiment 3 and Experiment 4 Data

Time 3 [s]	Volume 3 [mL]	Time 4 [s]	Volume 4 [mL]
0.00	0.00	0.00	0.00
150.04	5.00	21.58	5.00
175.84	10.00	30.25	10.00
189.00	15.00	55.71	15.00
198.74	20.00	181.39	20.00
211.16	30.00	211.89	30.00
219.17	40.00	221.65	40.00
231.30	55.00	239.62	55.00
240.46	75.00	252.18	75.00
251.40	100.00	265.69	100.00
266.87	150.00	284.11	150.00
278.25	200.00	297.64	200.00
301.74	300.00	320.69	300.00
323.08	400.00	343.93	400.00
361.41	600.00	380.24	600.00
400.00	780.00	400.00	700.00

Aggregated Profile

Table C.31 Aggregate Time and Volume Data

Aggregate Time [s]	Aggregate Volume [mL]
0.00	0.00
64.87	5.00
79.87	10.00
96.41	15.00
145.24	20.00
169.56	30.00
186.67	40.00
211.25	55.00
226.08	75.00
241.18	100.00
260.41	150.00
274.67	200.00
300.49	300.00
323.33	400.00
360.97	600.00
392.83	760.00
400.00	793.33

C.9.3 Phase 3

Time 1 [s]	Volume 1 [mL]	Time 2 [s]	Volume 2 [mL]
0	0.00	0	0.00
12.84	5.00	19.18	5.00
24.08	10.00	27.07	10.00
38.60	15.00	38.02	15.00
82.55	20.00	53.10	20.00
184.04	30.00	105.50	30.00
209.90	40.00	153.84	40.00
229.80	55.00	191.63	55.00

Time 1 [s]	Volume 1 [mL]	Time 2 [s]	Volume 2 [mL]
242.47	75.00	210.29	75.00
257.49	100.00	231.16	100.00
275.67	150.00	254.29	150.00
289.48	200.00	270.09	200.00
316.38	300.00	300.05	300.00
338.91	400.00	325.68	400.00
374.30	600.00	360.79	600.00
400.00	725.00	400.00	820.00

TABLE C.32: Validation Experiment Volume Data

C.10 Trial 3: Artery Specific Analysis

C.10.1 Artery Specific Raw Data Capture

Table C.33 Experimental Data

Time	Experiment 1				Experiment 2				Experiment 3				Experiment 4				Experiment 5			
(s)	LAD1	LAD2	LCX	RCA	LAD1	LAD2	LCX	RCA	LAD1	LAD2	LCX	RCA	LAD1	LAD2	LCX	RCA	LAD1	LAD2	LCX	RCA
0	0	0	0	0	0	0	0	0	0	0	0	0	0	0	0	0	0	0	0	0
20	3.2	3.2	11.2	3.2	0.8	9.6	8	3.2	25.6	0	3.2	3.2	9.6	0	0	3.2	12.8	0	4.8	3.2
40	6.4	6.4	14.4	6.4	1.6	16	9.6	6.4	27.2	4.8	3.2	4.8	12.8	3.2	1.6	6.4	19.2	6.4	8	6.4
60	9.6	9.6	16	9.6	1.6	19.2	12.8	12.8	28.8	6.4	3.2	6.4	16	3.2	3.2	6.4	19.2	9.6	9.6	8
80	12.8	12.8	16	12.8	1.6	19.2	14.4	19.2	28.8	8	3.2	8	19.2	6.4	4	6.4	19.2	12.8	9.6	8
100	12.8	12.8	16	12.8	3.2	22.4	15.2	22.4	30.4	8	4.8	8	20.8	9.6	4.8	8	19.2	12.8	8.8	8
120	12.8	14.4	16.8	14.4	4	22.4	15.36	24	30.4	8	6.4	8	22.4	10.88	6.4	8	19.2	12.8	9.6	8
140	14.4	16	17.6	16	4.16	22.4	16	24	31.2	9.6	8	8	24	16	9.6	9.6	22.4	12.8	9.6	8
160	14.4	17.6	17.6	17.6	6.4	22.4	16	25.6	31.36	10.4	8.8	9.6	25.6	22.4	16	9.6	22.4	12.8	9.6	8
...																				
380	92.8	102.4	83.2	70.4	76.8	124.8	99.2	102.4	153.6	140.8	128	156.8	76.8	115.2	86.4	70.4	393.6	265.6	244.8	374.4
400	160	134.4	105.6	134.4	118.4	147.2	121.6	136	201.6	176	160	211.2	92.8	134.4	102.4	86.4	486.4	320	350.4	457.6

C.10.2 Polynomial Residual Analysis

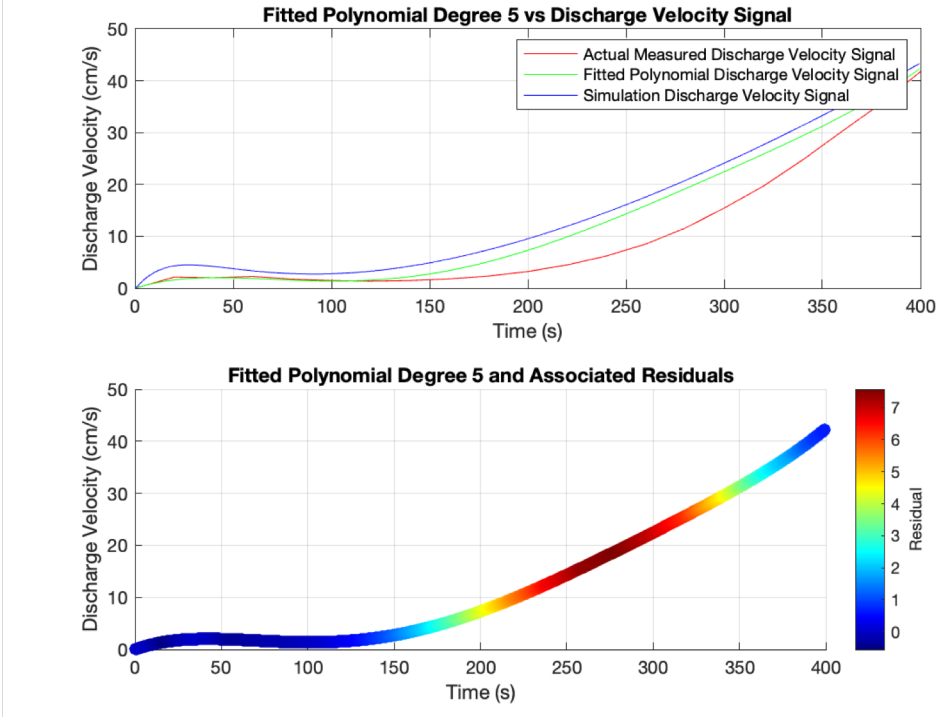

FIGURE C.2: Residual Characteristic of Polynomial Interpolated Discharge Velocity Signal

C.10.3 UDF Derivation

$$v_{\max}(t) = 3.75 \times 10^{-11}t^4 - 4.13 \times 10^{-8}t^3 + 1.625 \times 10^{-5}t^2 - 0.002295t + 0.1192$$

where the coefficients are in decreasing order of the powers of t.

Substituting $v_{\max}(t)$ into the velocity profile equation:

$$v(t,r) = \left(3.75 \times 10^{-11}t^4 - 4.13 \times 10^{-8}t^3 + 1.625 \times 10^{-5}t^2 - 0.002295t + 0.1192\right)\left(1 - \frac{r^2}{R^2}\right)$$

Thus, the fluid velocity depends on both time t and the radial position r. This equation shows that the velocity at each point in the pipe follows a fourth-degree polynomial in time, while retaining a parabolic shape in the radial direction.

At specific times, such as $t = 0$ and $t = 100$, we can observe the behavior of the velocity:

At $t = 0$, we have:

$$v(0,r) = \left(3.75 \times 10^{-11} \cdot 0^4 - 4.13 \times 10^{-8} \cdot 0^3 + 1.625 \times 10^{-5} \cdot 0^2 - 0.002295 \cdot 0 + 0.1192\right)\left(1 - \frac{r^2}{R^2}\right)$$

$$v(0,r) = 0.1192\left(1 - \frac{r^2}{R^2}\right)$$

Thus, the velocity profile is parabolic with a maximum value of 0.1192 at the center when $t = 0$.

At $t = 100$, we have:

$$v(100,r) = \left(3.75 \times 10^{-11} \cdot 100^4 - 4.13 \times 10^{-8} \cdot 100^3 + 1.625 \times 10^{-5} \cdot 100^2 - 0.002295 \cdot 100 + 0.1192\right)\left(1 - \frac{r^2}{R^2}\right)$$

Simplifying the polynomial for $t = 100$:

$$v(100,r) = \left(3.75 \times 10^{-11} \cdot 10^8 - 4.13 \times 10^{-8} \cdot 10^6 + 1.625 \times 10^{-5} \cdot 10^4 - 0.002295 \cdot 100 + 0.1192\right)\left(1 - \frac{r^2}{R^2}\right)$$

$$v(100,r) = (3.75 - 4.13 + 1.625 - 0.2295 + 0.1192)\left(1 - \frac{r^2}{R^2}\right)$$

$$v(100,r) = 1.1347\left(1 - \frac{r^2}{R^2}\right)$$

At $t = 100$, the maximum velocity at the center is 1.1347.

The final time-dependent velocity profile, incorporating the polynomial for the maximum velocity, is given by:

$$v(t,r) = \left(3.75 \times 10^{-11}t^4 - 4.13 \times 10^{-8}t^3 + 1.625 \times 10^{-5}t^2 - 0.002295t + 0.1192\right)\left(1 - \frac{r^2}{R^2}\right)$$

This equation models fluid velocity as a parabolic function of the radial position r and a polynomial function of time t.